Power Electronics- based Photovoltaics Panel Fault Detection using Online Impedance Measurement Technique

Jeet Bhavick Panchal

Thesis submitted to the faculty of the

Virginia Polytechnic Institute and State University

in partial fulfillment of the requirements for the degree of

Master of Science

In

Electrical Engineering

Rolando Burgos, Chair

Bo Wen

Dong Dong

December 8, 2022

Blacksburg, Virginia

Keywords: Photovoltaics panel, fault, small signal, AC impedance

Power Electronics- based Photovoltaics Panel Fault Detection using Online Impedance Measurement Technique

Jeet Bhavick Panchal

ABSTRACT

Photovoltaics panel (PV) integration with the utility grid has been installed throughout the globe. The fault-monitoring technology for photovoltaics (PV) panels is a method to save energy production losses and become a key contributor to overall cost reduction in variable operating costs for photovoltaics systems. PV researchers today explore factors such as reducing utility energy bills and CO_2 emissions, grid voltage stability, peak demand shaving, supply of electric power off-grid areas, and many more.

The technology discussed is easy to incorporate, requires no additional hardware, doesn't alter the system's stability, is implemented at a steady state point, and is helpful to record changes in PV cell operation from forward bias to reverse bias state. PV panel AC impedance can be used as an early-stage fault indicator. Also, comparing AC impedance magnitude and phase at maximum power point (MPP) or near MPP can help identify the nature of the fault in a PV system.

The focus of the thesis is proposing the fault detection of 300 W PV panels using online AC impedance measurement, utilizing existing panel-level power optimizers and microinverters in a PV system to actively perturb small signals into the PV panel and compute its small signal impedance. The technology is incorporated in a power optimizer

with C2000 MCU and helps identify hot spot faults and short circuit faults in a 300 W rooftop PV panel.

Multiple PV panel faults scenarios such as hot spot faults, short circuit faults, junction box faults, and capacitor faults are investigated to deduct further the effectiveness of the online impedance measurement using a small signal. This thesis's focus areas are, first, modeling the PV panel and power converter and incorporating fault scenarios to identify the fault indicators. Secondly, measuring PV panel impedance under normal and faulty conditions using an equipment-based offline technique. Lastly, measuring PV panel impedance under normal and faulty conditions using a power optimizer.

Power Electronics- based Photovoltaics Panel Fault Detection using Online Impedance Measurement Technique

Jeet Bhavick Panchal

GENERAL AUDIENCE ABSTRACT

A Photovoltaics panel is a series and parallel combination of many photovoltaics cells to generate electricity from sunlight via a photoelectric process. The fault-monitoring technology for photovoltaics (PV) panels is a method to save energy production losses and become a key contributor to overall cost reduction in variable operating costs for photovoltaics systems. The PV panel, over a period of time, can degrade with fluctuations in temperature and weather. Photovoltaics panel (PV) integration with the utility grid has been installed throughout the globe. PV researchers today explore factors such as reducing utility energy bills and CO2 emissions, grid voltage stability, peak demand shaving, supply of electric power off-grid areas, and many more.

The technology discussed is easy to incorporate, requires no additional hardware, doesn't alter the system’s stability, is implemented at a steady state point, and is helpful to record changes in PV cell operation from forward bias to reverse bias state. A PV panel operating at maximum power point (MPP) generates direct current (DC) and maintains a stable voltage across the PV panel load. A small signal injection in PV panel current or voltage is an addition of a sinusoidal signal with an amplitude of 10 % to the operating point of PV panel voltage or current and frequency sweep between 10 Hz to 200 kHz. The

PV panel's AC impedance is measured under small signal injection and can be used as an early-stage fault indicator. Also, comparing AC impedance magnitude and phase at maximum power point (MPP) or near MPP can help identify the nature of the fault in a PV system.

The focus of the thesis is proposing the fault detection of PV panels using online AC impedance measurement and utilizing existing panel-level power optimizers and microinverters in a PV system to actively perturb small signals into the PV panel and compute its small signal impedance. The technology is incorporated in a power optimizer with C2000 MCU and helps identify hot spot faults and short circuit faults in a 300 W rooftop PV panel.

This thesis's focus areas are, modeling the PV panel and power converter and incorporating fault scenarios to identify the fault indicators. Multiple PV panel faults scenarios such as hot spot fault, short circuit fault, junction box fault, and capacitor fault are investigated to further deduct the effectiveness of the online impedance measurement using a small signal. Secondly, measuring PV panel impedance under normal and faulty conditions using an equipment-based offline technique. Lastly, measuring PV panel impedance under normal and faulty conditions using a power optimizer.

ACKNOWLEDGMENT

Firstly, I would like to thank my advisor, Dr. Rolando Burgos, for allowing me the opportunity to pursue my master's degree with the Center for Power Electronics Systems (CPES) at Virginia Tech. His guidance and feedback throughout my degree helped me grow as an engineering and researcher. His profound experience and knowledge of power electronics systems motivated me to continue this path.

I would also like to sincerely thank and express my heartfelt appreciation to my co-advisor and mentor, Dr. Bo Wen. During our weekly meetings, Dr. Wen guided me from presentations, rational thinking, and hardware testing to questioning myself with the results produced. He helped me add more skill sets to my bag throughout this journey. He proves the quote, "A mentor is someone who sees more talent and ability within you, than you see in yourself, and helps bring it out of you."

I thank my committee member, Dr. Dong Dong, for agreeing to join my master's committee and devoting his time to our discussion and valuable suggestions during the master's defense.

Thank you to the Department of Energy for sponsoring this research project which led to the accomplishment of this thesis. I thank Tobias Ahlgrim, Mike Little, and Nareshkumar Nandola from the Siemens team for your time and discussion during our weekly meetings.

Thank you to all the professors in CPES for your helpful guidance in courses. Thank you to all the CPES staff, Ms. Audri Cunningham, Ms.Ling Li, Mr. Matthew Scanland,

Ms. Brandy Grim, Ms. Teresa Shaw, Mr. Dennis Grove, Ms. Yan Sun, lab director Mr. David Gilham and lab assistant Neil Croy for your help and support. Thank you to my program advisors for providing detailed information on completing this degree and helping me during difficulties.

Thank you to my many friends and peers in CPES; although I haven't had a chance to work together, you have never hesitated to share your wisdom. These people are Mr. Jayesh Motwani, Mr. Pranav Raj Prakash, Mr. Yugal Gupta, Ms. Qing Lin, Ms. Biqi Wang, Ms. Lakshmi Ravi, Mr. Ripun Phukan, Mr. Matthias Spieler, Mr. Che-Wei Chang, Ms. Aishworya Roy, Mr. Mark Cairnie, Mr. Yuliang Cao, Mr. Gibong Son, Mr. Sridhar Sundaramoorthy, Mr. Bhavin Jain, Mr. Joshua Stewart, Mr. Jian Liu, Mr. Arthur Mendes, Mr. Jesi Miranda-Santos, Mr. Vladimir Mitrovic, Mr. Paul Mourges, Mr. David Nam, Mr. Adhistira Naradhipa, Mr. Xingchen Zhao, Mr. Minh Ngo, Dr. Boran Fan, Dr. Slavko Mocevic, Ms. Ning Yan. Many other people helped me but are not listed here. I want to thank them also. My friends, thank you for listening, offering advice, and supporting me. Special thanks to Vihang Vasa, Abhinav Soni, Prakhar Sah, Dishant Shah, Kiran Kumar, Vivek Goyal, Aparajita Sengupta.

I want to express my profound gratitude to my parents, Anita and Bhavick Panchal, for providing me with unfailing support and continuous encouragement throughout my years of study and through the process of researching and writing this thesis. Also, thanks to my sisters Nidhi, Nicky, and brother Mitul, the accomplishment wouldn't have been possible without you. Finally, I offer my most profound appreciation to my love Vaibhavi Pandit, who stood by me through all my travails, absences, and impatience.

Table of Contents

List of Figure

List of Table

Chapter 1 Introduction

1.1 Photovoltaics Panel under Faults

Solar photovoltaics (PV) has seen rapid growth for many years and is expected to grow further with a continuous decrease in the cost of technologies [1]. Photovoltaic energy is noise-less, pollution-free, and easy to install system [8]. The United States alone has reached a total solar PV capacity of 95 GW_{dc} at the end of 2020 and is expected to reach 202 GW_{dc} by 2025 [3]. Rapid growth in the improvement of PV technologies has also helped provide cost-effective solutions for the decarbonizing electric grid. Since 2016, the United States has shifted from a multicrystalline PV modules system (6.3 kW) to a monocrystalline PV modules system (7 kW) for residential rooftops owing to better efficiency. From 2010 to 2022, a cost reduction benchmark of 64% in the residential rooftop to $2.71 per watt DC is attributed to hardware cost [3]

PV systems are susceptible to various faults, such as modules, cabling, protection, converters, and inverters. PV system reliability, monitoring, and fault diagnosis is crucial in timely detecting and solving faults [7]. Under extreme environmental conditions such as dust, snow, high temperature, cloudy weather, and many more, panels may undergo defects. Faults in any component of Photovoltaics systems can affect the efficiency and yield of energy as well as the security and reliability of PV systems

1.2 Literature Review

A mathematical PV model can provide a detailed electrical characteristic under varying environmental conditions. A Simulink-based PV model is introduced in [1]-[5] where the model involves forward bias, reverse bias, and nonlinear dynamics of PV cell and compares I-V and the

P-V characteristics from simulation and experimental results, which helps emulate a string mismatch or partial shading conditions under PV cell reverse biased. Component-level faults generally cause photovoltaic systems' faults in modules, connection lines, converters, inverters, etc. Fault detection and diagnosis methods are necessary to obtain the PV system's high efficiency, energy yield, security, and reliability. Timely fault monitoring, analysis, detection, and diagnosis can help increase the life of PV systems. The survey paper discusses various visual and thermal methods to detect discoloration, browning, surface soiling, hot spot, breaking, and delamination of PV panels.[6]-[10] Under harsh environmental conditions, PV modules may encounter browning or delamination of EVA on the solar cells, which can lead to a decrease in current production, cumulatively decreasing the adequate power of the PV panel. Faults such as junction box faults are related to soldering points where the cable connects to the bypass diodes in the PV modules. Due to improper soldering, fretting corrosion can occur in aged PV modules. Fretting corrosion can lead to an increase in contact resistance of the solder point in a junction box; the rise in resistance tends to DC arching and can lead to a fire in a junction box. Energy from the PV module is extracted using power optimizers or microinverter to transfer it efficiently to the grid. DC link capacitor in switching power converter is used to provide switching current, helping suppress dc link voltage ripple and maintain energy balance in the system during transients and abnormal operations. Thermal and electrical stress can be a reason for the degradation fault in a capacitor. The paper discusses multiple methods of conditional monitoring for dc-link capacitors to enhance the reliability of the power converter. Fault detection can be an effective way to diagnose and extend the life of a PV system.

[11], [12] The DC model of the PV cell is not able to characterize the internal process of the PV cell. Thus, electrochemical impedance spectroscopy (EIS) is utilized in some literature to measure impedance fluctuation. A significant advantage of EIS over other modeling techniques is that the extracted parameters can be used to quantitatively observe the changes in the internal dynamic processes under various operational conditions. Thus, EIS has been beneficial for device characterization and fault condition monitoring. The impedance spectroscopy is also helpful in detecting cracks and interconnection ribbons disconnection in PV panels by observing the decrease in parallel resistance and increase in parallel capacitance due to cracks in PV modules. AC parameter characterization can help to detect faults such as partial shading or hot spot within a series of PV cells. A PV comprises series, parallel resistances, and parallel capacitance, which are affected by voltage bias, illumination, and temperature. Under maximum power point tracking control, with the presence of a hot spot in a single cell of a series of PV cells, utilizing AC small signal injection, the capacitance and dc impedance increase can be a fault indicator for hot spot fault.

[13]-[17],[19] The AC impedance method is utilized in research to evaluate electrochemical device characteristics. An online impedance measurement is a helpful tool in the control system; the power converter can measure the input or output impedance in real time to monitor the stability and take corrective action if needed. A real-time power converter estimates the increase in output capacitance under fault conditions using an online impedance-based technique. Digital control with a modified correlation method can be a helpful tool for power converter system identification to determine control-to-output response by cross-correlation of an input signal and sensed output signal. Using multi-period pseudo-random binary signal injection to the control input, input and

output impedance can be measured. The online AC impedance technique is utilized in the power converter to measure PV panel ac impedance using a Pseudo random binary signal (PRBS). Fault monitoring and detection can eventually decrease the operational and maintenance cost of a PV system. [18] The report mentioned the mathematical derivation and the software-based model to estimate the operational and maintenance cost related to photovoltaic systems. The cost model takes a few assumptions on system size, type, environmental conditions, and age to provide a detailed cost change over a very long performance period.

1.3 Motivation and Outline

1.3.1 Cost Reduction and Evaluation

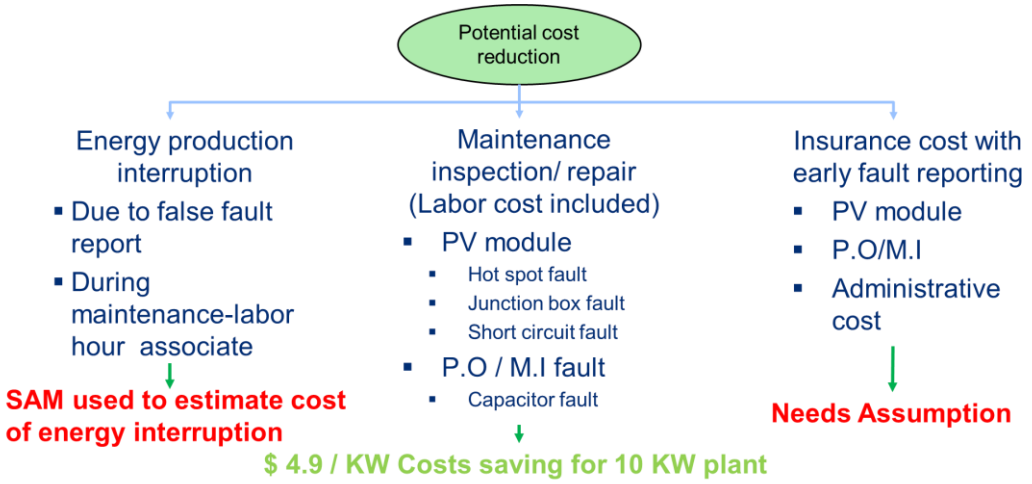

Figure 1-1 Potential cost reduction details using online impedance algorithm technique

The online impedance measurement technique for PV panel fault detection and identification is valuable to alert the operational and maintenance (O&M) personnel for corrective action, thereby reducing energy production losses. The technique helps reduce potential costs such as energy production interruption, maintenance inspection and repair, insurance costs with early

fault reporting, and many more. The Figure 1-1 shows the method to deduce the potential cost reduction of the Levelized cost of energy (LCOE) for residential PV rooftop systems. The total decrease in LCOE adds up to $6.3 / kW for a 10 kW residential PV rooftop system. Energy production interruption, maintenance inspection, and repair reduction cost estimation are shown below. Insurance cost with early fault reporting needs several assumptions regarding administrative fees. The quotation from insurance companies varies under several scenarios and thus is not covered in this project.

1.3.1.1 Energy Production Interruption:

Parameter	Value	Units
Total Capacity	9.98	DC kW
Module power	300	W
Module quantity	34	
Project life	25	years
DC loss	3	%

Figure 1-2 Photovoltaics System electrical parameter for determining the cost of energy production interruption

Metric	Value
Annual AC energy in Year 1	18,601 kWh
DC capacity factor in Year 1	21.3%
Energy yield in Year 1	1,864 kWh/kW
Performance ratio in Year 1	0.78
LCOE Levelized cost of energy nominal	7.08 ¢/kWh
LCOE Levelized cost of energy real	5.66 ¢/kWh
Electricity bill without system (year 1)	$1,514
Electricity bill with system (year 1)	$144
Net savings with system (year 1)	$1,370
Net present value	$3,800
Simple payback period	15.8 years
Discounted payback period	Inf
Net capital cost	$27,156
Equity	$0
Debt	$27,156

Figure 1-3 SAM report result for the system specified

Energy interruption during hot spot faults, short circuit faults, and junction box faults is calculated using the System advisor model (SAM). SAM is a techno-economic model designed to facilitate decision-making for people involved in the renewable energy industry. SAM's user

interface organizes and displays the performance, and financial model inputs help display tables and graphs of the results. The model utilizes irradiance and weather data, sun position, and surface angle based on the latitude and longitudes of the PV system location. The effective plane of array irradiance is calculated with the system's self-shading, external shading, and soiling losses input. The PV farm specifications are mentioned in Figure 1-2. The SAM model generates an extensive report based on the location of the PV farm, the number of PV modules, the orientation of PV panels, shading and soiling losses, and many more, and computes effective annual AC energy generation. The energy yield is further utilized for calculating the Levelized cost of energy and the net present value of the PV system. The SAM-based report for the PV system mentioned in the above-mentioned figure is shown in Figure 1-3.

Table 1-1 Energy interruption cost saving for 10 KW PV farm with downtime

PV Fault	Identification time (days)	Delivery time (days)	Service time (hours)	Total downtime (day)
Junction Box	1	1	3	2.125
Short circuit	1	2	5	3.208
Hot Spot	2	2	5	4.208

Table 1-2 Energy interruption cost saving for 10 KW PV farm with downtime

No. of times fault (per year)	Nominal LCOE (₵/kWh)	Net preesent value ($)	Energy yield (kWh/kW)	No. of times fault thorughout project life	Decrease in energy yield (kWh/kW)	Cost Saving ($/kW)
0	7.08	3800	1864	-	-	-
1	7.09	3794	1863	20	1	1.416
2	7.1	3787	1861	20	3	4.248
5	7.12	3767	1857	20	7	9.912
10	7.15	3734	1850	20	14	19.824

To incorporate energy production interruption in SAM, DC losses are considered, and with a time stamp, the PV panel under fault will be turned off. As the PV panel is turned off, the difference in the energy yield will correspond to the cost due to energy production interruption. Table 1-2 is an assumption for PV panel downtime per fault. For a PV panel under fault, out of 34 PV panels, the effective DC loss is 3% from the equation, as shown below.

$$DC\ loss\ (\%) = \frac{PV\ panel\ under\ fault}{Total\ PV\ panel\ modules} * 100$$

Considering the DC loss for the PV system as discussed above for the PV panel fault and corresponding time stamp, the SAM generates the report with a decrease in energy yield and an increase in the Levelized cost of energy (LCOE). Table 1-2 shows the number of times fault can

appear per year with nominal LCOE, net present value, and energy yield as given by SAM. Considering each year, once a junction box fault, hot spot fault, and short circuit fault appears in the PV system, the energy yield decreases by 1 kWh/ kW. As shown in the equation below, the cost savings due to energy production interruption if the fault doesn't arise is $ 1.416 per kW.

$$Cost\ saving = \Delta Energy\ yield * Nominal\ LCOE(no\ fault) * fault\ throught\ life \quad (1\text{-}1)$$

1.3.1.2 Operational & Maintenance Cost:

Maintenance and repair cost saving was calculated using Sunspec Alliance's operational and maintenance spreadsheet tool. The spreadsheet is a proforma cost modeling tool for PV industry operation and finance practitioners designing and budgeting PV O&M plans.

Table 1-3 lists adequate cost savings for maintenance and repair. The list provides a cost for detecting and identifying hot spot faults, short circuit faults, and junction box faults, as given by the spreadsheet tool. Utilizing the table above for effective cost saving under maintenance and repair, the O&M spreadsheet was used to compare the annualized O&M cost for a 10 KW PV farm, as shown in the table above. Table 1-4 shows the comparison of O&M costs before the implementation of the online algorithm and after the implementation of the online algorithm. As shown in the figure mentioned above, the online algorithm is effective in reducing $ 4.8 from the total annualized O&M cost per KW per year.

Table 1-3 Net present value cost saving in operation and maintenance per fault

Sr. No.	Details	NPV Cost saving – total
1.	Use infrared camera to inspect for hot spots; bypass diode failure	$ 30
2.	Test modules showing corrosion of ribbons to junction box	$ 53
3.	Test output of modules that exhibit cracked glass, bubble formation oxidation of busbars, discoloration of busbars, or PV module hot spots (bypass diode failure)	$ 15
4.	Replace modules failing performance test or IR scan	$ 455
5.	Monitoring annual service package	$ 122

Table 1-4 Operational and maintenance cost-saving comparison using an online impedance measurement technique

Online Impedance Algorithm	Before implementation	After implementation
Plant Size (kWp DC)	10.0	10.0
Energy Yield Year 1 (kWh/kWp/year)	1,400.0	1,400.0
Module Power (W STC)	305	305
Annualized O&M Costs ($/year)	**$350**	**$301**
Annualized Unit O&M Costs ($/kW/year)	$34.95	$30.14
NPV Annual O&M Cost per kWh	**$0.032**	**$0.027**

1.3.2 Thesis Outline

In Chapter 1, the PV panel faults are introduced with the current trends in PV panel fault identification are discussed. The literature review discusses a costly and complex algorithm for identifying PV panel faults. The motivation for online AC impedance measurement is also concerned with cost reduction evaluated using the SAM tool and operational and maintenance spreadsheet tool, totaling $ 6.3 per KW cost reduction in operating and maintenance cost and energy production interruption cost.

In Chapter 2, the PV cell was modeled using an analytical equation in Simulink. The non–linear Simulink-based PV cell model AC impedance was measured using a small signal injection in PV panel current. The PV cell impedance was compared between the Simulink-based model and traditional analytical equation, obtaining a less than 5% error between both. The PV cell Simulink model AC impedance was measured and compared under temperature and illumination fluctuations. A PV string with 18 PV cells in series was modeled, and a hot spot fault scenario was

discussed. Also, in this chapter, DC /DC power converter for a PV panel was modeled, fault scenarios under hot spot, short circuit, junction box, and capacitor fault are discussed, and fault indicators are identified.

Chapter 3 discusses the hardware setup for PV panel I-V characteristics measurement. Also, hardware setup and equipment for measuring PV panel offline AC impedance are discussed. A 300 W solar panel simulator was designed to illuminate PV panels using LED sheets. With the solar simulator, illuminated PV panel I-V characteristics was compared under normal condition and faulty scenarios. Small signal injection equipment was used to measure PV panel offline AC impedance under normal conditions and compared with faulty procedures. In addition, multiple PV panel fault cases are also discussed, and the fault indicators were obtained.

Chapter 4 discusses the importance and updating DC /DC converters for power optimizer applications. LM5170EVM was operated as a boost converter; the inductance and switching frequency of the converter were updated to run the converter in continuous conduction mode. Boost converter inductor current was controlled using average current control. Converter close loop simulation was compared with hardware performance under 24 W and 75 W power.

In Chapter 5, single-tone small signal injection was implemented in DC/DC converter using a software-based frequency response analyzer (SFRA). The input impedance of the DC/DC converter with the PV panel was measured using a small signal injection. Indoor PV panel impedance was measured using a small signal injection via SFRA. PV panel impedance was computed and compared under normal and fault conditions. Outdoor PV panel impedance was measured using small signal measurement, and PV panel impedance was compared under normal

and fault conditions. The relative standard deviation of online impedance was calculated, and less than 5% deviation was recorded.

Chapter 6 summarizes the work done in this thesis and explores options for future work.

Chapter 2 Modeling of Photovoltaics Cell and Power Optimizer

2.1 Introduction

The photovoltaic panel generates electrical power from the sun and sources the electrical energy for the utility grid. The photodiode present in the PV panel sinks the energy from the sun's irradiance and generates an electrical current. In literature, many authors have provided a single diode-based PV model, but it fails to compute the dynamic characteristics of PV panels. The dynamic characteristics of the PV model considers the transient and steady-state response of PV panels under varying environmental conditions. The dynamic characteristics of PV panels consist of forward and reverse biased effects on PV cells which helps to model PV panels under different fault conditions. The PV dynamic model circuit consists of Photocurrent (Iph), Forward diode (Df), Parallel capacitance (Cp), Reverse diode (Dr), Reverse voltage breakdown (Vbd), Shunt resistance (Rsh), Series resistance (Rs), and Series inductance (Ls). As shown in Figure 2-1, the PV cell dynamic model generates PV panel current from photocurrent. The panel current gets affected by forward diode current, reverse diode current, parallel capacitance, shunt resistance, and other parasitic due to leads and tabbing wire for positive and negative cable.

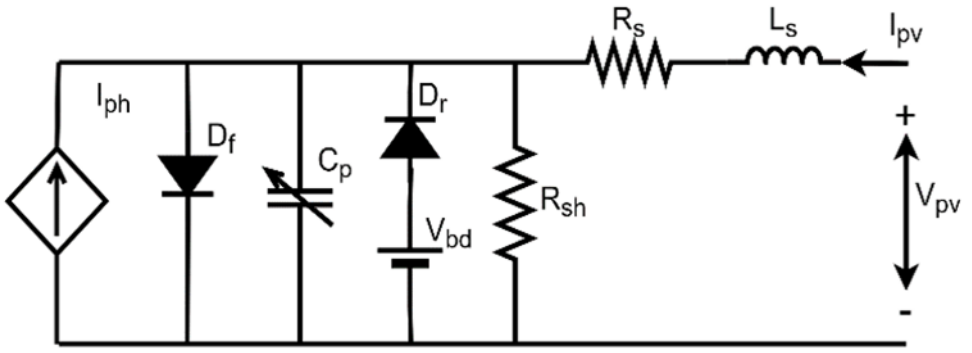

Figure 2-1 Dynamic PV cell equivalent circuit

Photovoltaics panel at a specific illumination (G) and temperature (T) produces current and voltage. With the change in temperature and irradiance, the PV panels' operating point shifts with the change in current and voltage delivered by the PV panel. Either illumination following the PV panel is directly proportional to the amount of current generated by the PV panel. Thus, a power converter is essential to sink maximum power from PV panels under varying environmental conditions. The power converter, like a power optimizer or microinverter, operates the PV panel under maximum power point (MPP) using the maximum power point tracking (MPPT) algorithm.

2.2 Modelling Photovoltaics Cell

2.2.1 Analytical Equations Governing Photovoltaics Cell

Diode voltage and PV panel current are used to calculate the voltage across the PV panel. The effect of photocurrent, forward diode, parallel capacitance, shunt resistance, reverse diode, and breakdown voltage forms PV panel current. Also, the equations governing the effects of the forward diode, reverse diode, parallel capacitance, and shunt resistance use diode voltage, and thus nonlinear solving techniques are used. The sets of analytical equations used in the Simulink-based PV model to compute PV panel voltage are shown below.

Table 2-1 Multicrystalline PV cell parameters

Parameter	Abbreviation	value	Units
Nominal irradiance	G_n	1000	J/K
Nominal temperature	T_n	298.15	C
Short circuit current	I_{scn}	7.61	A
Open circuit voltage	V_{ocn}	0.624	V
MPP current	I_{MPP}	7.03	A
MPP voltage	V_{MPP}	0.45	V
Current temperature coefficient	K_i	0.00495	A/K
Voltage temperature coefficient	K_v	-0.0022	V/K
Series resistance	R_s	0.046	Ω
Shunt resistance	R_{sh}	91.8	Ω
Series Inductance	L_s	5e-8	H
Ideality factor	α	1.31	
Breakdown voltage	V_{bd}	-23.5	V
Reverse saturation current	I_{sr}	0.0997	A
Reverse current temperature coefficient	K_r	0.0114	
zero voltage capacitance	C_{j0}	1.17e-5	F
zero voltage potential	Φ_0	0.82	V
mean carrier lifetime	τ	5.76e-6	s
breakdown mean carrier lifetime	τ_{bd}	0	s

Photocurrent: The photoelectric effect caused by light falling on the PV panel ejects electrons forming photocurrent I_{ph}. The photocurrent is directly proportional to illumination and change in temperature. The photocurrent is limited by the short circuit current I_{scn}, series resistance R_s, and shunt resistance R_{sh}. K_i is the current temperature coefficient, G_n is the nominal illumination in W/m^2, and T_n is the nominal temperature in K. Iscn and Ki are usually mentioned by the manufacturer's datasheet or taken from the literature. Table 2-1 says the internal parameters of the monocrystalline PV cell.

$$I_{ph}(G,T) = \left[I_{scn}\left(\frac{R_s + R_{sh}}{R_{sh}}\right) + K_i(T - T_n)\right]\frac{G}{G_n} \qquad (2\text{-}1)$$

Forward diode current: For a diode considering a P-N junction diode, with an increase in temperature, thermal voltage increases, as shown below. K is the Boltzmann constant, N_s is the number of series PV cells, and q is the electron charge.

$$V_t = \frac{KT}{N_s q} \quad (2\text{-}2)$$

Under the reverse bias condition of a PN junction diode, a small number of current flows independent of the bias voltage is termed saturation current I_s. V_{ocn} is the open circuit voltage, K_v is the voltage temperature coefficient, α is the ideality factor, and K_i is the current temperature coefficient.

$$I_s(T) = \frac{I_{scn} + K_i(T - T_n)}{\exp\left(\frac{V_{ocn} + K_v(T - T_n)}{\alpha V_t(T)}\right)} \quad (2\text{-}3)$$

The forward bias diode current has a dependency on temperature via thermal voltage. With the increase in temperature, the thermal voltage increase, also the potential barrier decreases; thus, the change in forwarding bias diode current increases.

$$I_{df}(T, V_d) = I_s(T)\left[\exp\left(\frac{V_d}{\alpha V_t(T)}\right)\right] \quad (2\text{-}4)$$

Reverse diode current: I_{sr} is the reverse saturation current, K_r is the reverse breakdown coefficient, and V_{bd} is the breakdown voltage.

$$I_{dr}(T, V_d) = I_{sr}\left[\exp\left(\frac{K_r V_{bd}}{\alpha V_t(T)}\right)\right]\left[\exp\left(\frac{-K_r V_d}{\alpha V_t(T)}\right) - 1\right] \quad (2\text{-}5)$$

Parallel capacitance: Photovoltaics (PV) cells operate under forward and reverse bias conditions. The PV cell capacitance is influenced by the panel voltage (Vpv), illumination (G), and temperature (T) of the PV cell. The parallel capacitance Cp of a PV cell is a summation of capacitance under three different regions of operation, such as junction, diffusion, and breakdown capacitance. As the name suggests, the junction or depletion capacitance Cj of a PV cell comes

from a charge stored in the depletion region of the PN junction diode. C_{j0} is the zero-voltage capacitance, and ϕ_0 is the zero-voltage potential.

$$C_j(V_d) = \frac{C_{j0}}{\sqrt{1 - \frac{V_d}{N_s \emptyset_0}}} \quad (2\text{-}6)$$

Diffusion capacitance C_d comes from the rate of change of injected charge with voltage; also, the injected charge lies in the junction outside the transition region. Referring to the charge control description of a diode, the diode current is proportional to the charge stored of the excess minority carrier and inversely proportional to the mean life of the minority carrier (τ).

$$C_d(T, V_d) = \frac{\tau I_{df}(T, V_d)}{\alpha V_t(T)} \quad (2\text{-}7)$$

The breakdown capacitance C_{bd} dominates when the PV cell reverse biasing voltage is higher than the PV cell breakdown voltage. The analytical equation considered for C_{bd} was modeled like C_d to avoid a complicated model where τ_{bd} is the mean lifetime of the carrier under the breakdown region.

$$C_{bd}(T, V_d) = \frac{\tau_{bd} I_{dr}(T, V_d)}{\alpha V_t(T)} \quad (2\text{-}8)$$

Therefore, overall parallel capacitance C_p

$$C_p(T, V_d) = C_j(V_d) + C_d(T, V_d) + C_{bd}(T, V_d) \quad (2\text{-}9)$$

The parallel capacitance computed C_j, C_d, and C_{bd} shouldn't be negative; thus, if added negative, the respective capacitance can be termed 0. The parallel capacitance current I_{cp}:

$$I_{cp}(V_d) = C_p(T, V_d)\, dV_d/dt \quad (2\text{-}10)$$

Shunt resistance current: The shunt resistance R_{sh} in a PV cell is caused due to the leakage current of the P-N junction, and the value is dependent on the fabrication process of the PV cell

$$I_{sh}(V_d) = V_d/R_{sh} \quad (2\text{-}11)$$

Diode voltage: By modeling all the above currents, adding the current at the nodal point, and using Kirchhoff's current law, V_d can be computed. The expression was a nonlinear equation and thus modeled in Simulink using algebraic constraint or using Newton -Raphson technique.

$$I_{ph}(G, T) - I_{df}(T, V_d) - I_{cp}(V_d) + I_{dr}(T, V_d) - I_{sh}(V_d) - I_{pv} = 0 \quad (2\text{-}12)$$

PV panel voltage: With the knowledge of diode voltage, PV panel voltage can be computed as the additional voltage drop will be across the series resistance (R_s) and series inductance (L_s).

$$V_{pv}(V_d, I_{pv}) = V_d - I_{pv}R_s - L_s\frac{dI_{pv}}{dt} \quad (2\text{-}13)$$

The series resistance of a PV cell is the summation of structural resistance either contact of the metal base with p doped semiconductor layer, the resistance of the base and emitter layers, the contact resistance of the n-doped layer with the top metal grid, the resistance of the grid and other contact resistances. The series inductance present was due to the low parasitic inductance of electrical wires, the tabbing wire connecting the cell to the electrical terminals. The effect of Rs can be seen when the operating point is to the right of MPP (constant voltage region). Also, with an increase in Rs, the short circuit current will decrease, and it does not affect open circuit voltage.

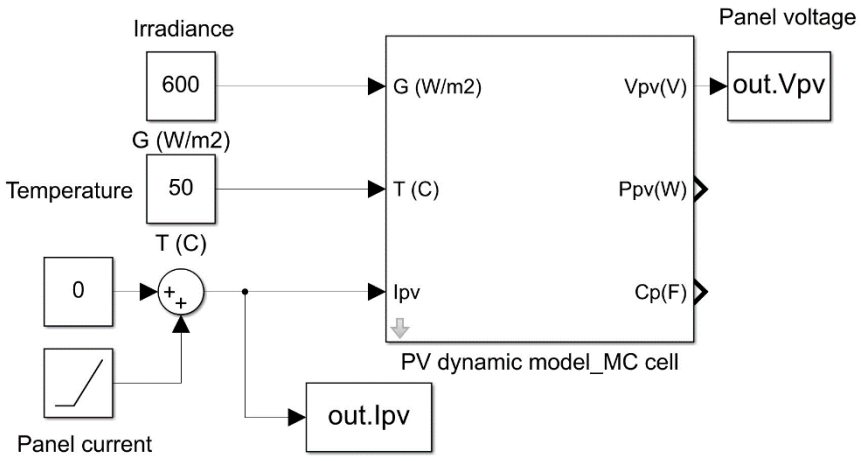

Figure 2-2 Simulink- based PV cell model

2.2.2 Simulink-based Photovoltaics Model

A monocrystalline PV cell was modeled in Simulink using the equations mentioned above, which is shown in Figure 2-2. The inputs to the model are illumination G, temperature T, and PV panel current Ipv, and the output of the model was PV panel voltage and parallel capacitance of the PV cell. To design the model, the internal parameters of the monocrystalline PV cell are to be considered for computing the diode and PV panel voltage. The list of parameters and their values are mentioned in Table 2-1. These monocrystalline PV cell parameters are taken from the literature. PV datasheet generally provides nominal operating characteristics of PV cells such as open circuit voltage, short circuit current, MPP voltage, MPP current, voltage temperature coefficient K_v, and current temperature coefficient K_i.

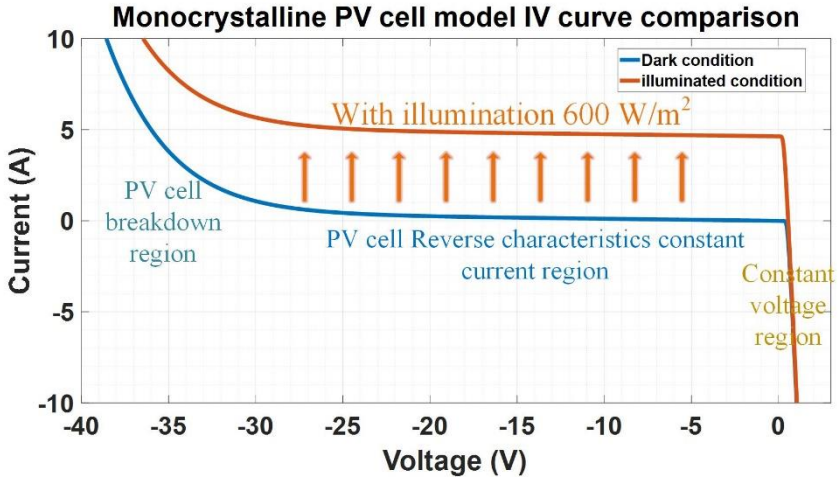

Figure 2-3 PV cell I-V characteristics comparison using Simulink model

The Simulink model was utilized to plot the Current-Voltage characteristics of monocrystalline PV cells under the dark condition with 0 W/m^2 and 600 W/m^2 illuminated conditions. The temperature was kept constant at 50 °C, and the current was swept from 10 A to –10 A. The I-V characteristics are compared between dark and illuminated conditions and are shown in Figure 2-3. The curve can be divided into three regions: the Breakdown region, where the PV cell breakdown characteristics are noticed under -23.5 V; the reverse bias region, where the current was constant between V_{bd} and 0 V and the forward bias region, above 0 V. With illumination, the photocurrent magnitude increases and thus the I-V curve can be observed to be shifted upwards.

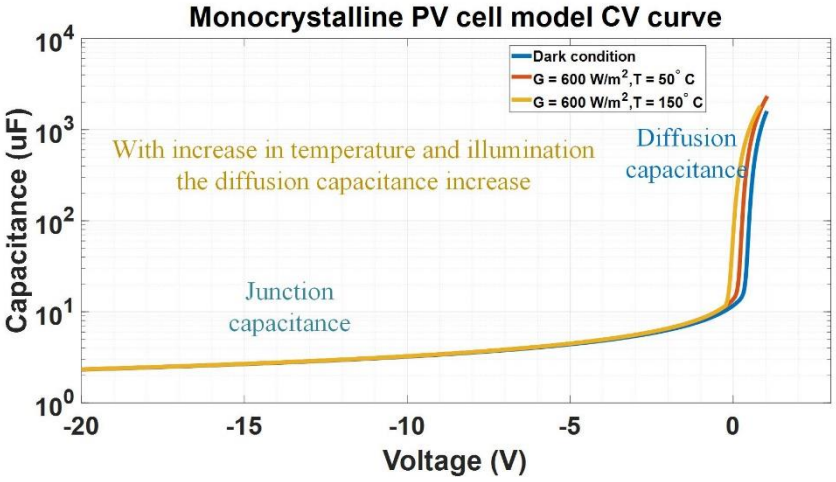

Figure 2-4 PV cell capacitance Vs. Voltage characteristics using the Simulink model

The Simulink-based PV cell model provides parallel capacitance information for the operating point. The PV cell current was a sweep in model from 10 A to -10 A under three different conditions: under dark conditions, G = 0 W/m^2 and T = 50 °C; under increased illumination conditions, G = 600 W/m^2 and T = 50 °C and under increase temperature condition G = 600 W/m^2 and T = 150 °C to compare capacitance-voltage characteristics of the monocrystalline PV cell. From the image, as shown in Figure 2-4, the diffusion capacitance was lower under dark conditions, and the diffusion capacitance increased with an increase in temperature and illumination. Also, in all three states, the junction capacitance was minimal, with lower in dark conditions.

2.2.3 PV cell AC Small Signal Model

A PV cell dynamic model includes the effect of diodes, voltage source, capacitance, resistance, and inductance. Under AC small signal injections, the effects of the current source, diodes, voltage source, and shunt resistance can be cumulatively considered parallel resistance of

PV cells. With the change in operating point, temperature, and illumination, the parallel resistance and parallel capacitance vary. Figure 2-5 shows the effective ac small signal model of PV cells.

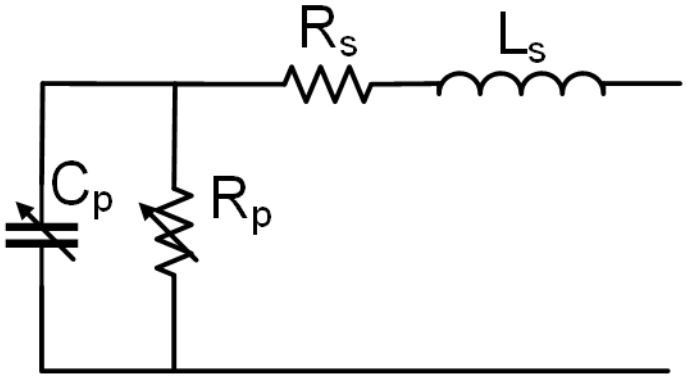

Figure 2-5 AC small signal PV cell circuit

The small signal mathematical equation of the figure mentioned above is,

$$Z = \left(R_p \parallel {}^{1}/_{sC_p}\right) + R_s + sL_s \qquad (2\text{-}14)$$

Solving the equation, we get,

$$Z = \left[R_s + \frac{R_p}{\alpha + 1}\right] + j\left[L_s\omega - \frac{\omega R_p^2 C_p}{\alpha + 1}\right] \qquad (2\text{-}15)$$

where $\omega = 2\pi f$ and $\alpha = \omega^2 R_p^2 C_p^2$

As shown above, the analytical equation for PV cell impedance can be plotted using a bode plot. The impedance response over frequencies can be compared with parallel resistance and capacitance variations. Under low frequency, the impedance was resistive with the constant magnitude of $R_s + R_p$ and impedance phase being 0 °; also, with an increase in R_p, the impedance magnitude increases. Under mid-frequency, the parallel capacitance was dominant, with phase decreasing towards -90 ° and impedance magnitude decreasing. With the increase in parallel

capacitance, the impedance magnitude and phase shift towards the left as the effect of capacitance can be seen at frequencies lower than mid-frequency. Also, the lowest impedance in the magnitude plot will be approximately R_s at a resonating frequency between C_p and L_s. The resonating frequency also sifts towards the left with the increased parallel capacitance. At high frequencies, the L_s effect dominates with phase increasing and reaching 90 ° and impedance magnitude increasing after resonating frequency.

2.2.4 Simulink-based PV Cell Model Impedance Measurement

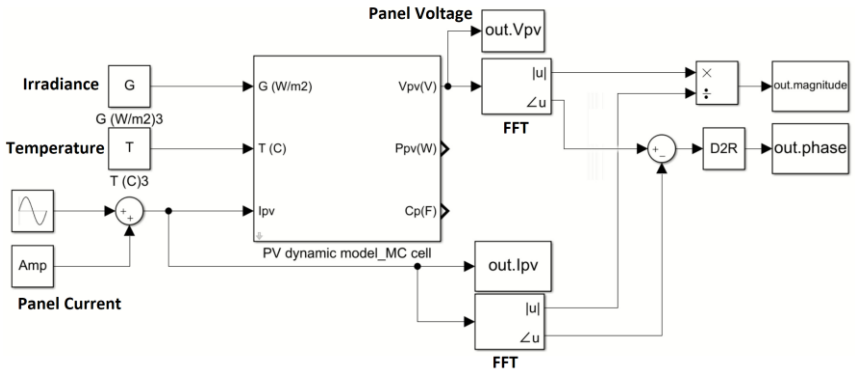

Figure 2-6 PV cell AC impedance measurement using Simulink model

Simulations are conducted using a Simulink-based PV cell model to measure the impedance under different operating conditions. The Simulink-based PV model, as shown in Figure 2-2, was injected with AC small signal with illumination and temperature, as shown in Figure 2-6. The AC small signal current was added to an operating point, and the output in terms of PV panel voltage has a DC and AC component. To measure the AC impedance of the PV cell, a set of frequencies from 10 Hz to 100 kHz on a logarithmic scale was injected into the PV panel current, and the voltage response was measured. FFT analysis was performed using a Simulink-based FFT block to compute the magnitude and phase of the PV panel voltage and current at the

injected AC signal fundamental frequency. Using the division operator, the magnitude of the PV panel voltage from the FFT block was divided by the magnitude of the PV panel current to compute the impedance magnitude of the PV cell under the mentioned operating point. Similarly, the phase of the PV panel voltage was subtracted from the phase of the PV panel current to compute the PV cell impedance phase. With the conditions mentioned above, the impedance plot was plotted in MATLAB.

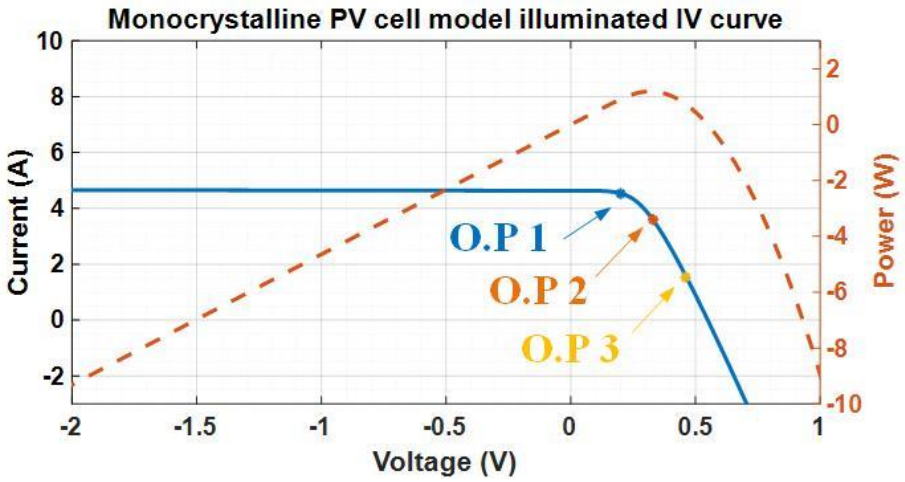

Figure 2-7 I-V characteristics of PV cell under 600 W/m^2 illuminations using Simulink model

A monocrystalline PV cell was modeled under 600 W/m^2 illumination, and 50 °C temperature in Simulink; PV cell current was swept to measure current – voltage and power-voltage characteristics as shown in Figure 2-7. The PV cell impedance was plotted in MATLAB using a bode plot, shown in Figure 2-8. Three operating points marked in the figure as mentioned above are considered to measure PV panel AC impedance.

Operational point (O.P.) 1 was the point at the left of the maximum power point (MPP); the O.P was under a constant current region, and with a change in current, the voltage difference

will be high, and thus the impedance magnitude will be increased as compared to point at MPP or on the right side of the MPP using the equation as shown below.

$$Z_{dc} = -\frac{\Delta V}{\Delta I} \quad (2\text{-}16)$$

The AC impedance phase of O.P. 1 shows phase drops earlier than other O.P. as the R_p was higher using the equation as shown below than compared to other O.P., and so the phase drop was also at a lower frequency.

$$\omega_p = \frac{1}{R_{low,f} C_p} \quad (2\text{-}17)$$

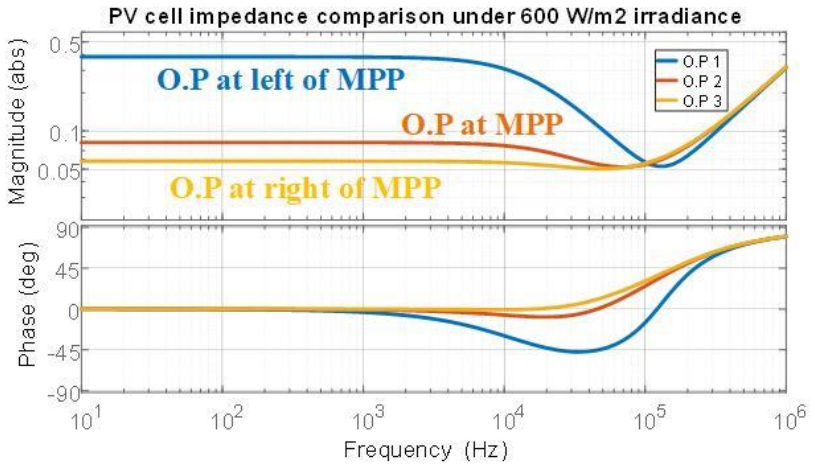

Figure 2-8 Simulink-based AC impedance measurement of PV cell under 600 W/m^2 illumination

The AC impedance magnitude of O.P 3 was lowered than other O.P. as the O.P. 3 was on the right side of the MPP and under a constant voltage region; with a slight change in PV current, the PV panel voltage change will be smaller, and thus the AC impedance magnitude will be less than the point at MPP and point on the left side of the MPP. The PV cell capacitance decreases

with voltage decreasing as shown in the figure above, comparing O.P 3 capacitance with other O.P., with larger capacitance, the phase drop in mid frequency will be less than other O.P. With higher capacitance, the resonating point was also at lower frequencies compared to other O.P using the equation as shown below.

$$\omega_r = \frac{1}{\sqrt{L_s C_p}} \quad (2\text{-}18)$$

The AC impedance magnitude and phase of O.P 2 stay in the middle of the other two O.P. as the O.P was at MPP of the PV cell. To conclude, the AC impedance magnitude of PV cell decreases from left to right of MPP, and the AC impedance phase at mid-frequency shows a higher phase drop from left to right of MPP.

2.2.5 Comparing Analytical AC Impedance Results with Simulation:

Table 2-2 Electrical parameter comparison of PV cell at the different operating points

Operating point	Voltage (V)	Current (A)	Parallel Capacitance (μF)	Parallel Resistance (Ω)
1	0.2	4.53	32	0.336
2	0.33	3.6	185	0.0352
3	0.46	1.54	500	0.0118

The PV cell Simulink model computes PV panel voltage under different operating conditions, as shown in Table 2-2. The PV cell model also calculates parallel capacitance based on PV panel voltage and current. The parallel resistance of the PV cell under different operating conditions was determined using a Simulation-based AC small signal model. The series resistance

and series inductance of PV cells are assumed constant with changes in operating conditions. Using parallel resistance and parallel capacitance of the PV cell, as shown in the table above, an analytical solution was compared with a simulation-based PV cell impedance solution.

The PV cell AC small signal impedance computed via the Simulink-based model matches well with the analytical solution under all three operating conditions. Further, to understand the average percentage error under all the frequency points of AC impedance % deviation was computed and compared of all the three operating points using the equations as shown below.

$$\%deviation = \left(\frac{Simulation\ -Analytical}{Simulation}\right) * 100 \qquad (2\text{-}19)$$

The average % error between PV cell AC impedance between Simulink – the based model and analytical solution was less than 5 % under all the frequencies computed, as shown in Figure 2-9.

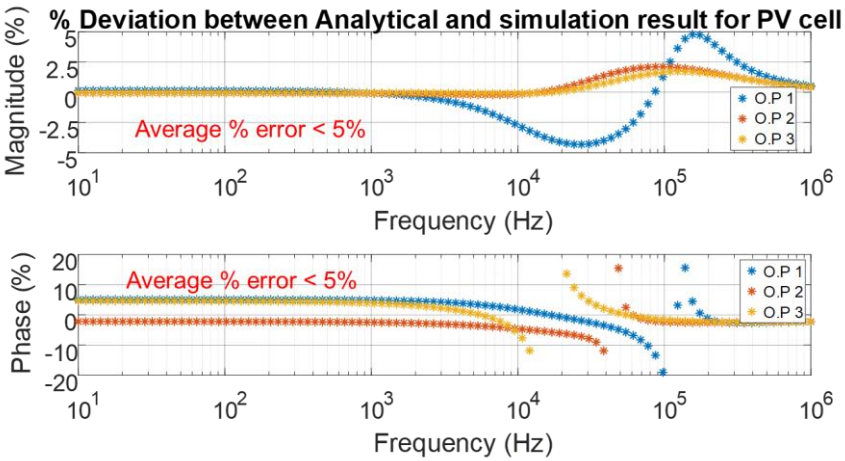

Figure 2-9 Relative standard deviations between analytical Vs. Simulation of PV cell AC impedance

2.2.6 PV cell Impedance Comparison:

2.2.6.1 Under Dark Conditions with G = 0 W/m^2 and T = 50°C:

The Simulink-based PV cell model was simulated under the dark condition with the illumination of 0 W/m^2 and a temperature of 30°C. The I-V characteristics are measured with a PV cell current sweep to obtain the forward and reverse characteristics of the PV cell. The measured I-V curve is shown in Figure 2-10, under dark conditions with G being 0 W/m$^{2;}$ thus, the PV cell's photocurrent using the equation in Chapter 2.1.1, will be 0 A. Four operating points mentioned in the image below are used to compare PV cell AC impedance using Simulink- the based small signal AC model. The PV cell AC impedance plot is shown in Figure 2-10 with a comparison of all four operating points. Under -2.1 V, the O.P. was at a reverse voltage biased region, and thus the parallel resistance and parallel capacitance will be higher in magnitude compared to the rest of the O.P. For O.P. at 0 V due to no illumination, the current will also be nearly 0 A, and the AC impedance magnitude will be lower than reverse biased condition; also AC impedance phase will be higher than reverse bias condition.

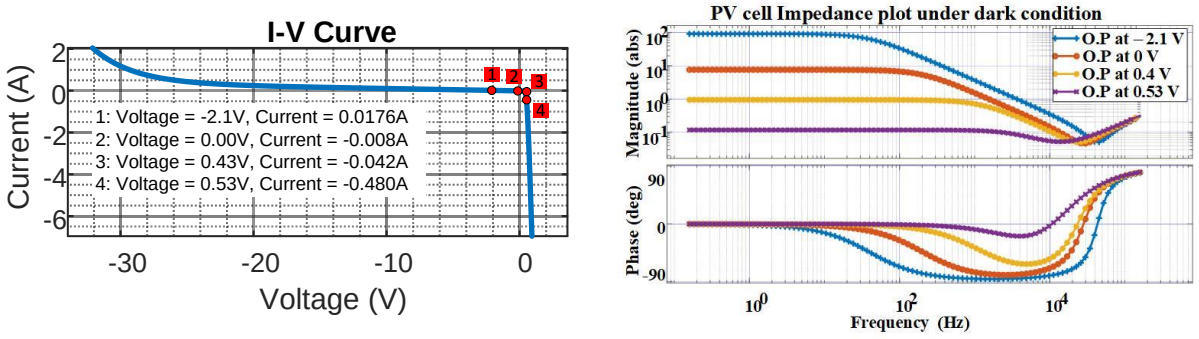

Figure 2-10 Left: PV cell I-V characteristics, right: PV cell AC impedance, condition: under 0W/m^2 illumination and 50 ˚C temperature

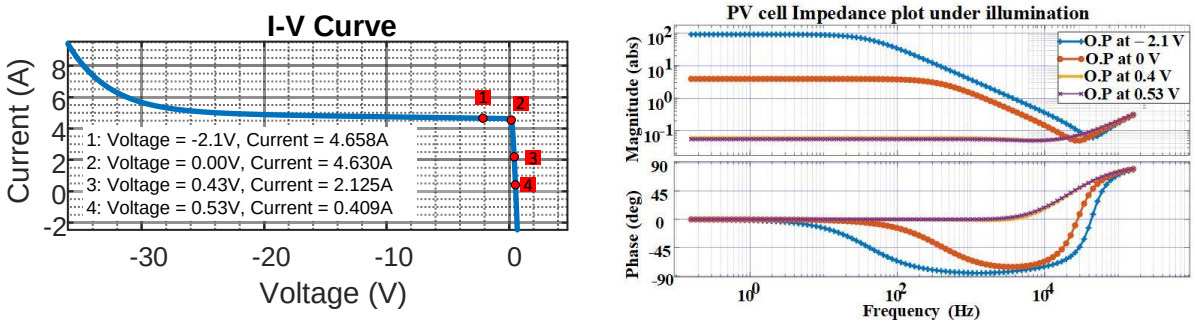

Figure 2-11 Left: PV cell I-V characteristics, right: PV cell AC impedance, condition: under 600W/m2 illumination and 50 ˚C temperature

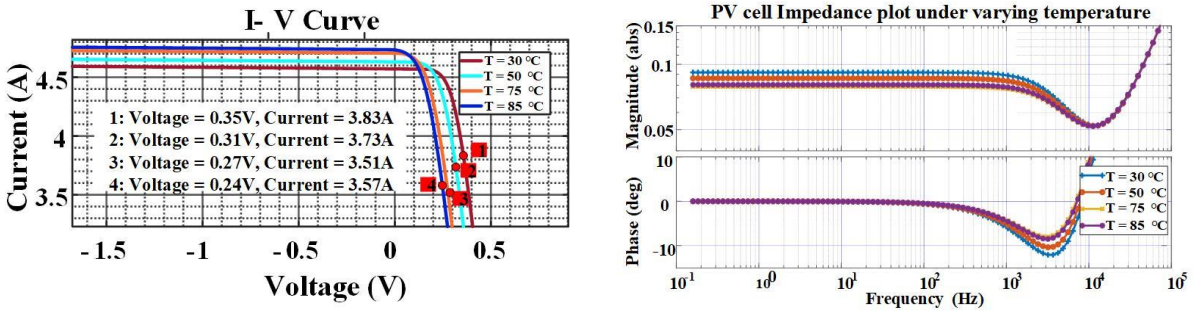

Figure 2-12 Left: PV cell I-V characteristics, right: PV cell AC impedance, condition: under 0W/m2 illumination and varying temperature

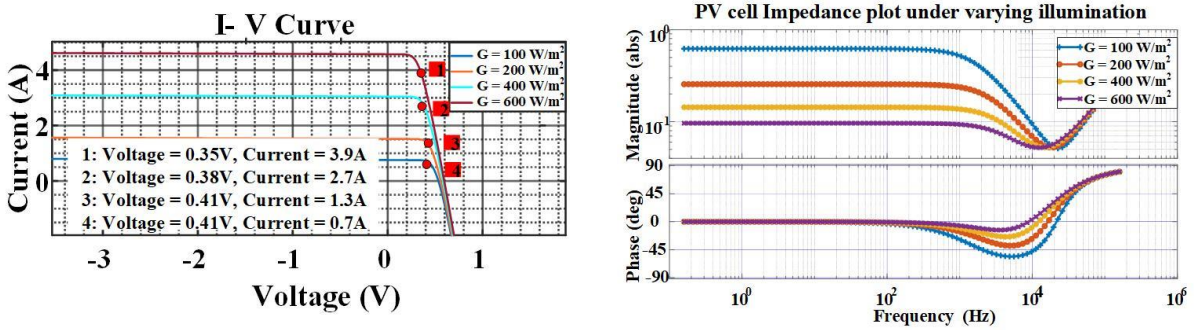

Figure 2-13 Left: PV cell I-V characteristics, Right: PV cell AC impedance, condition: under varying illumination and 50 ˚C temperature

The PV cell impedance plot shows impedance magnitude increasing with parallel resistance increasing and impedance phase increasing with parallel capacitance decreasing as the O.P. moves from the left to right side of MPP under dark conditions.

2.2.6.2 Under Normal Conditions with G = 600 W/m^2 and T = 50°C:

The illumination of the PV cell was increased from 0 W/m^2 to 600 W/$m^{2,}$ keeping the temperature at 30°C; the current was swept to plot the I-V characteristics of the PV cell. The I-V characteristics are shown in Figure 2-11, comparing the I-V characteristics of the dark and illuminated conditions; due to photocurrent, the current magnitude has increased, and the PV cell can source current. Four operating points with the same PV cell biased voltage as dark condition are considered to measure and compare PV cell impedance using the Simulink-based AC small signal model, and shown in Figure 2-11. Comparing PV cell AC impedance under dark and illuminated conditions, the impedance magnitude under reversed voltage biased region was similar. The operating point under forward-biased conditions with illumination shows a decrease in the AC impedance magnitude and a decrease in the phase. The MPP operating point can be easily distinguished with highly decrease in impedance magnitude under illumination, thus change in parallel resistance between dark conditions and illumination was effectively more at MPP.

2.2.6.3 Under Normal Conditions with G = 600 W/m^2 and T vary:

Figure 2-12 shows the simulation result of I-V characteristics of the PV cell under temperature variation keeping G at 600 W/m^2 constants. With a PV cell's temperature increase, the PV panel voltage and current decrease at MPP. Four test conditions were simulated with varying

temperatures, and AC impedance was plotted at MPP, as shown in Figure 2-12. The effective change noticed was under the low-frequency region where due to higher temperature, the parallel resistance decreases, and thus impedance magnitude decreases. With temperature, the diffusion capacitance increases, as stated above; therefore, the parallel capacitance change was small and unnoticed. Under the mid-frequency region, due to effective change in parallel resistance and parallel capacitance, the phase decreases with temperature increases.

2.2.6.4 Under Normal Conditions with T = 50°C and G varies:

Figure 2-13 shows the simulation result of I-V characteristics of the PV cell under illumination variation keeping T at 50°C constants. With the increase in the illumination of a PV cell, the PV panel current increases due to the rise in photocurrent. Also, the PV panel voltage decreases due to an increase in current as the voltage drop due to series resistance increases. Four test conditions were simulated with varying illumination, and AC impedance was plotted at MPP, as shown in Figure 2-13. The effective change noticed was under the low-frequency region where due to higher illumination, the parallel resistance decreases, and thus the impedance magnitude decreases. With illumination, the diffusion capacitance increases, as shown above; hence the parallel capacitance increases. Under the mid-frequency region, due to the rise in parallel capacitance and a decrease in parallel resistance, the phase decreases with an increase in illumination.

2.2.7 18 PV Cells in Series Forming PV String:

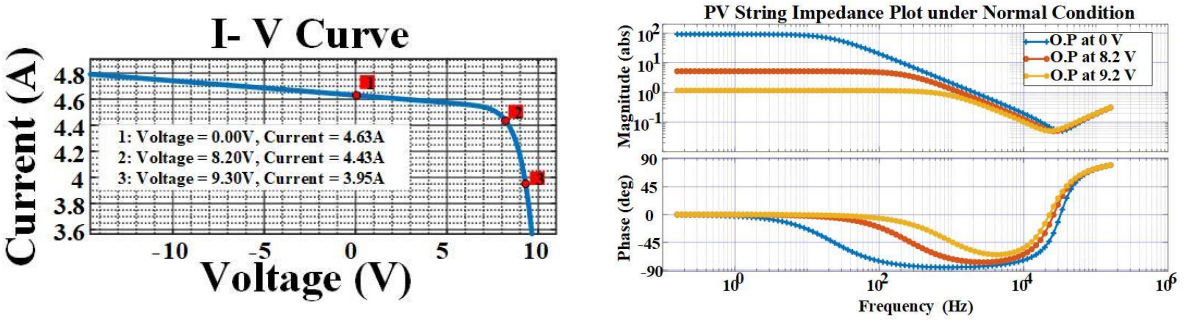

Figure 2-14 Left: 18 PV cell I-V characteristics, Right: 18 PV cell AC impedance, condition: under 600 W/m^2 illuminations and 50 ˚C temperature

The Simulink-based monocrystalline PV cell was series together with 18 PV cells forming a PV string. The PV string was simulated with G = 600 W/m^2 and T = 50 °C, and the PV string current was swept to plot the I-V characteristics of the PV string. Figure 2-14 is the I-V characteristics of monocrystalline PV string in the forward and reverse bias region. The I-V curve marks three operating points to measure the PV string AC impedance using PV string small signal model. The figure shown above shows PV string AC strings under different operating points. All three operating points are under the forward region, with O.P.1 having a high AC impedance magnitude under low frequency and O.P 3 having a low AC impedance magnitude under low frequency. O.P.2 being the MPP has AC impedance magnitude being both the O.Ps. The AC impedance phase of O.P. 2 was between the O.Ps, and as stated above, the parallel resistance increases and the parallel capacitance increases with O.P. shift from left to right.

2.2.7.1 PV String under Hot Spot Conditions:

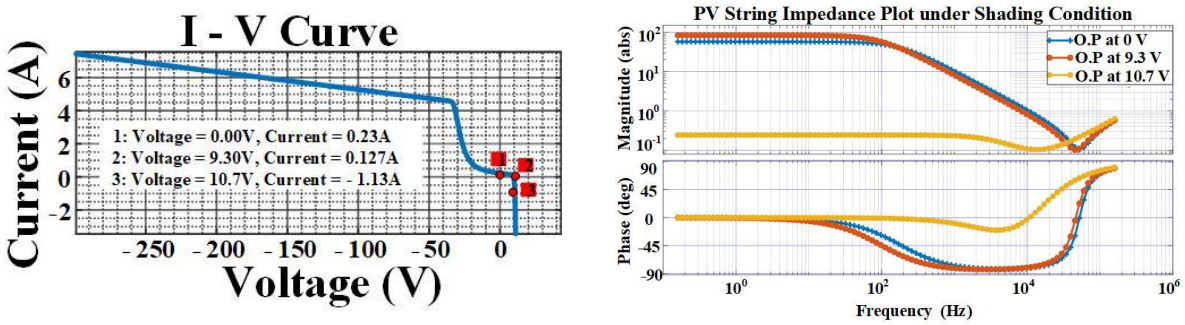

Figure 2-15 Left: 18 PV cell I-V characteristics, right: 18 PV cell AC impedance, condition: under 1 PV cell hot spot condition with 17 PV cell at 600 W/m2 illuminations and 50 ˚C temperature

The hot spot condition prevails when a particular PV cell or some of the PV cells in the PV string are shaded (illumination less than nearby PV cells in the PV string) so that the PV cell will sink power produced by PV cells or PV strings rather than the source. Due to sinking power, the temperature of the PV cell increases, and the PV cell gets damaged, damaging the entire PV string. The PV string is 18 monocrystalline PV cells series and was simulated under hot spot conditions. Under hot spot conditions, one of the PV cells of the PV string was shaded with G = 0 W/m^2 and T = 150 °C. the PV string current was swept, and the I-V characteristics are shown in Figure 2-15. Here, due to the shading of one PV cell in the entire PV string, the PV string current dropped compared to the normal condition. The PV panel voltage increased for MPP; the 17 illuminated PV cells have higher forward biased voltage due to low PV string current compared with fully illuminated PV string (18 illuminated PV cells), and the shaded PV cell in the hot spot conditions was reverse biased with positive PV string current and sinking power rather than sourcing power thus creating hot spot condition. Comparing the AC impedance of the PV string under a hot spot

and normal conditions at MPP, the AC impedance magnitude at low frequency was higher in hot spot conditions than normal conditions; thus, the parallel resistance was higher in hot spot conditions than normal conditions. In the mid-frequency region, the AC impedance phase dropping of the hot spot region was at a slightly low frequency than normal conditions showing the effect of an increase in parallel capacitance. At a resonating point, the resonating frequency of the hot spot condition was slightly lower than normal; thus, with increased parallel capacitance, the resonating frequency decreased. Thus, from above, due to the hot spot condition when one PV cell was shaded in PV string and considering the O.P.at MPP, the PV string current changes, PV string voltage changes, under low-frequency AC impedance magnitude increase, the AC impedance phase at mid-frequency decreases, the resonating frequency decreases the parallel resistance increases and parallel capacitance increases cumulatively.

2.3 A Power Converter for PV Panel:

Renewable energy in the form of solar energy feeds the power to the electrical grid. Power from the PV panel is DC in nature, and so is converter to AC using inverter topology and supplied to the electrical grid. To obtain maximum power from the PV panel, the maximum power point tracking (MPPT) algorithm is used in the power converter; with changes in environmental conditions like illumination and temperature, the power produced by the PV panel varies and utilizing the MPPT algorithm power extraction will be maximized. In a residential rooftop PV system, 30-40 PV panels produce kilowatts of power, and the generated power is supplied to the electrical grid. In this PV system, each PV panel has a power optimizer where power from each power optimizer gets into the DC bus. From the DC bus, the central inverter converts DC power to AC power to supply the electrical grid, as shown in Figure 2-16. The power optimizer has

features such as voltage step up or steps down, MPPT algorithm, maintaining the DC voltage, monitoring PV panel performance, etc. Figure 2-17 is a power optimizer with boost topology; also, using voltage and current sensors, the MPPT block diagram is shown.

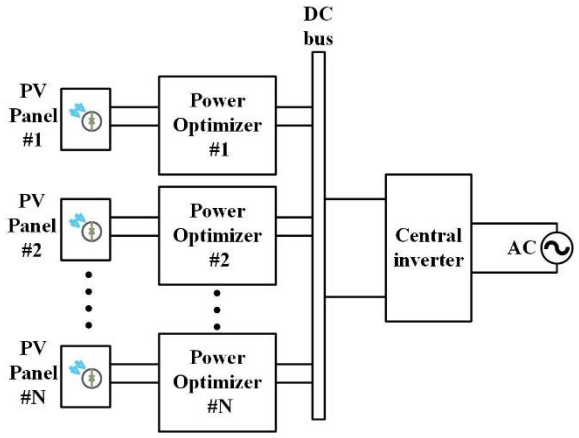

Figure 2-16 PV system with DC to AC power conversion using power optimizer and central inverter

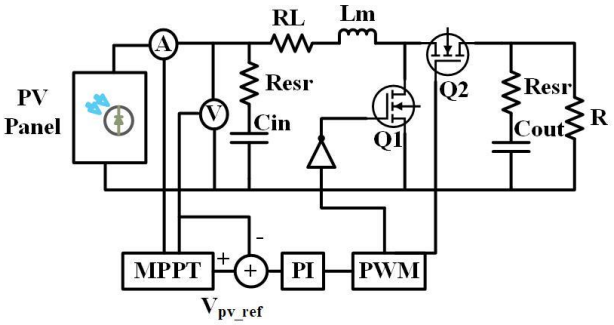

Figure 2-17 PV panel with a boost converter and MPPT control circuit diagram

2.3.1 Modeling Boost Converter:

PV panel with a boost converter will step up the output voltage depending upon the duty given to the power converter. Figure 2-18 is a boost converter with PV panel sourcing power to the output, input dc link capacitor C, inductor L resistance of inductor R, two MOSFETs Q1 and Q2, output capacitor $C_{dc,}$ and DC bus voltage V_{DC}. The current from the inductor is termed $i_{L,}$ and the output current to the DC bus is i_{DC}. The MPPT algorithm sets the reference voltage as the input voltage to operate the PV panel under MPP, the reference voltage then gets subtracted from the PV panel voltage, and the error signal is given to the PI controller. Based on its gain and pole, the

PI controller sets the reference duty, and the output is given to the MOSFETs drivers. The drivers provide switching signals to MOSFETs based on the duty assigned by the PI controller.

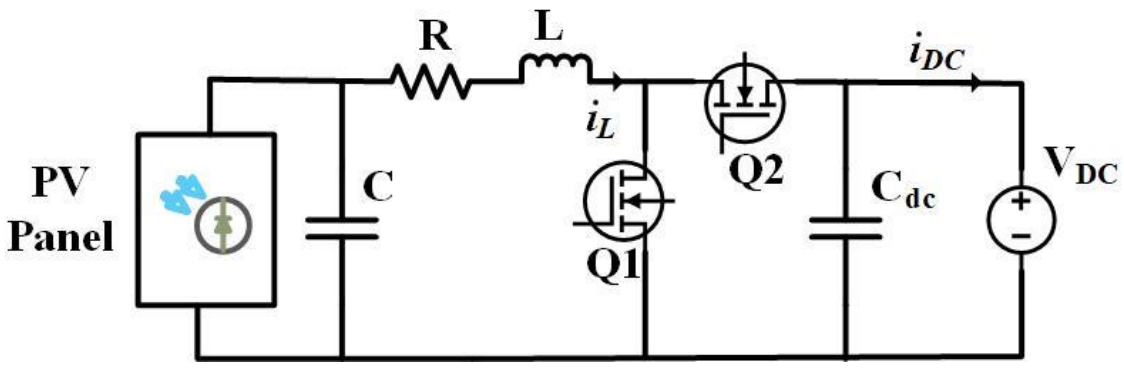

Figure 2-18 PV panel with a boost converter

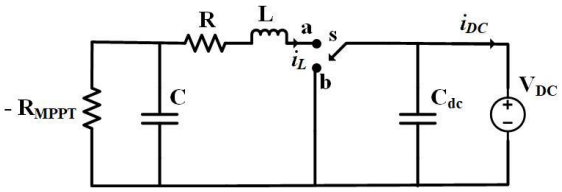

Figure 2-19 Boost converter with three port switch network

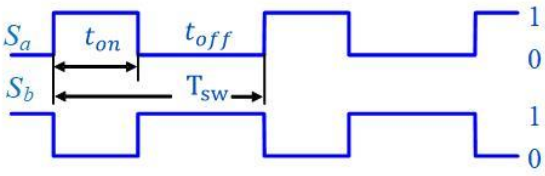

Figure 2-20 Timing diagram for three-port switch network

Initially, the PV panel was modeled as a negative impedance to model the boost converter as it sources power based on the voltage across it, as shown in Figure 2-19. Single-throw switches replace the MOSFETs. If s is connected to node point *a*, the voltage from the input and inductor will be provided to the output capacitor and DC bus, and if s is connected to node point *b*, the inductor will gets charged. The output capacitor will source power to the DC bus. The switching state is shown in Figure 2-20, and based on the duty cycle, the t_{on} and t_{off} will vary.

$$v_s = \begin{cases} V_{dc} & when\ s = 1 \\ 0 & when\ s = 0 \end{cases} \qquad v_s = sv_{dc} \tag{2-20}$$

$$i_s = \begin{cases} i_L & when\ s = 1 \\ 0 & when\ s = 0 \end{cases} \qquad i_s = si_L \tag{2-21}$$

$$d = \int_t^{t+T_{sw}} sdt \qquad \bar{v}_s = d\bar{v}_{dc} \quad \bar{\imath}_s = d\bar{\imath}_L \tag{2-22}$$

From the equations, as shown above, the voltage at node s is termed as $v_{s.,}$ and the current to the nodal point is termed as i_s. The average model of the boost converter with a PV panel is where the controlled voltage source is present due to duty and output voltage $V_{dc,}$ and the controlled current source is present due to duty and inductor current i_L. The average model helps convert the time-discontinuous system to a time-continuous one.

$$\mathrm{V_{pv}} = \mathrm{L}\frac{\mathrm{di_L}}{\mathrm{dt}} + \mathrm{Ri_L} + \mathrm{dV_{dc}} \tag{2-23}$$

The above equation is computed using Kirchhoff's voltage law (KVL) and considering voltage across the PV panel as V_{PV}.

$$\mathrm{i_{pv}} = \mathrm{C}\frac{\mathrm{dV_{pv}}}{\mathrm{dt}} + \mathrm{i_L} \tag{2-24}$$

Applying Kirchhoff's current law (KCL) at the node of the PV panel and dc link capacitor, we get the equation as shown above.

$$\frac{-\mathrm{V_{pv}}}{\mathrm{R_{mppt}}} = \mathrm{C}\frac{\mathrm{dV_{pv}}}{\mathrm{dt}} + \mathrm{i_L} \tag{2-25}$$

The PV panel current is equivalent to the voltage drop across R_{MPPT} ; the equation (2-24) can be rewritten as equation (2-25).

$$\frac{di_L}{dt} = \frac{V_{pv}}{L} - \frac{Ri_L}{L} - \frac{dV_{dc}}{L} \quad (2\text{-}26)$$

Equation (2-23) can be divided with inductor L and rewritten as equation (2-26)

$$\frac{dV_{pv}}{dt} = \frac{-V_{pv}}{CR_{mppt}} - \frac{i_L}{C} \quad (2\text{-}27)$$

Equation (2-25) can be divided by capacitor C and rewritten as equation (2-27)

$$\frac{d}{dt}\begin{bmatrix}\overline{i_L}\\ \overline{v_{pv}}\end{bmatrix} = \begin{bmatrix}-R/L & 1/L\\ -1/C & -1/CR_{mppt}\end{bmatrix}\begin{bmatrix}\overline{i_L}\\ \overline{v_{pv}}\end{bmatrix} + d\begin{bmatrix}V_{dc}\\ 0\end{bmatrix} \quad (2\text{-}28)$$

Taking inductor current i_L and PV panel voltage V_{PV} as the state variables, the state space equation is given by equation (2-28)

The above equations are computed using the average model; the average model still holds non-linearity in the system. Multiplication of time-varying signals generates harmonics and is a non-linear process. To further compute the model, linearization was performed;

$$\frac{d}{dt}\begin{bmatrix}\widetilde{i_L}\\ \widetilde{v_{pv}}\end{bmatrix} = \begin{bmatrix}-R/L & 1/L\\ -1/C & -1/CR_{mppt}\end{bmatrix}\begin{bmatrix}\widetilde{i_L}\\ \widetilde{v_{pv}}\end{bmatrix} + \tilde{d}\begin{bmatrix}V_{dc}\\ 0\end{bmatrix} \quad (2\text{-}29)$$

The system considers perturbation in duty and PV panel voltage to compute control to PV panel voltage response, as shown above.

$$s\widetilde{i_L} = \frac{\widetilde{v_{pv}}}{L} - \frac{R\widetilde{i_L}}{L} - \frac{\tilde{d}V_{dc}}{L} \quad (2\text{-}30)$$

Equating state variable $\widetilde{i_L}$ as shown in the above equation

$$s\widetilde{v_{pv}} = \frac{-\widetilde{v_{pv}}}{CR_{mppt}} - \frac{\widetilde{\imath_L}}{C} \quad (2\text{-}31)$$

Equating state variable $\widetilde{v_{pv}}$ as shown in the above equation

$$\left(s + \frac{R}{L}\right)\widetilde{\imath_L} = \frac{\widetilde{v_{pv}}}{L} - \frac{\tilde{d}V_{dc}}{L} \quad (2\text{-}32)$$

Solving the above equations and collecting the inductor current component together obtains the equation as shown above.

$$\left(s + \frac{1}{CR_{mppt}}\right)\widetilde{v_{pv}} = -\frac{\widetilde{\imath_L}}{C} \quad (2\text{-}33)$$

Solving the above equations and collecting the PV panel voltage component together obtains the equation as shown above.

$$\frac{\widetilde{v_{pv}}}{\tilde{d}} = \frac{-V_{dc}}{L\left[C\left(s + \frac{1}{CR_{mppt}}\right)\left(s + \frac{R}{L}\right) + \frac{1}{L}\right]} \quad (2\text{-}34)$$

Solving the above equations, the control to PV panel voltage transfer function is shown above.

$$\frac{\widetilde{\imath_L}}{\tilde{d}} = \frac{C\left(s + \frac{R}{L}\right)V_{dc}}{L\left[C\left(s + \frac{1}{CR_{mppt}}\right)\left(s + \frac{R}{L}\right) + \frac{1}{L}\right]} \quad (2\text{-}35)$$

Solving the above equations, the control to inductor current transfer function is shown above.

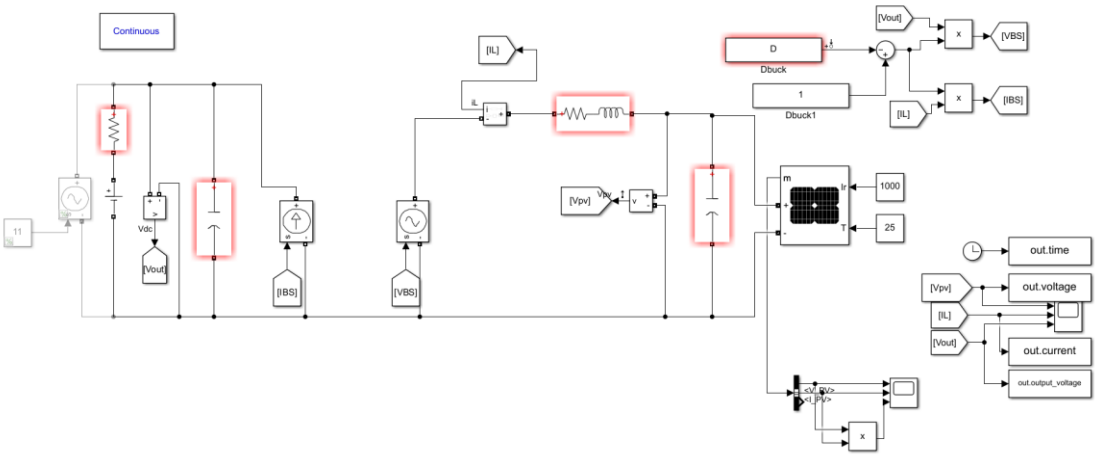

Figure 2-21 Simulink-based boost converter average model with PV panel as input

Simulink-based power converter model was built, as shown in Figure 2-21. A 30 monocrystalline PV cells-based PV panel was used in Simulink with G = 1000 W/m^2 and T = 25 °C to produce 13.5 V PV panel voltage and 7 A PV panel current at MPP.

Table 2-3 Boost converter along with PV panel parameters used in Simulation

Parameter	Value	Units
Number of PV cells	30	-
Output voltage	60	V
PV panel MPP voltage	13.5	V
Input Capacitance	470	µF
Series resistance	1	mΩ
Inductor	4.7	µH
Output Capacitance	100	µF

The boost converter average model parameters are shown in Table 2-3. An open loop boost converter model was simulated with a duty of 77.5% to obtain PV panel voltage and current at MPP. The analytical equation (36) provides the control for the PV panel voltage frequency response. To compute RMPPT, the impedance data was extracted from the analytical equation (18). The series resistance, parallel resistance, parallel capacitance, and series inductance parameters were calculated from the Simulink-based monocrystalline PV cell model.

The model linearization toolbox in Simulink was used to obtain linearization of control to PV panel voltage of the Simulink-based boost converter average model. The solution obtained was compared with the analytical solution from equation (2-26) and shown in Figure 2-22. The analytical solution of control to PV panel voltage frequency response well matches the Simulink-based linearization model; thus, the analytical solution was utilized to design the closed loop operation of control to PV panel voltage.

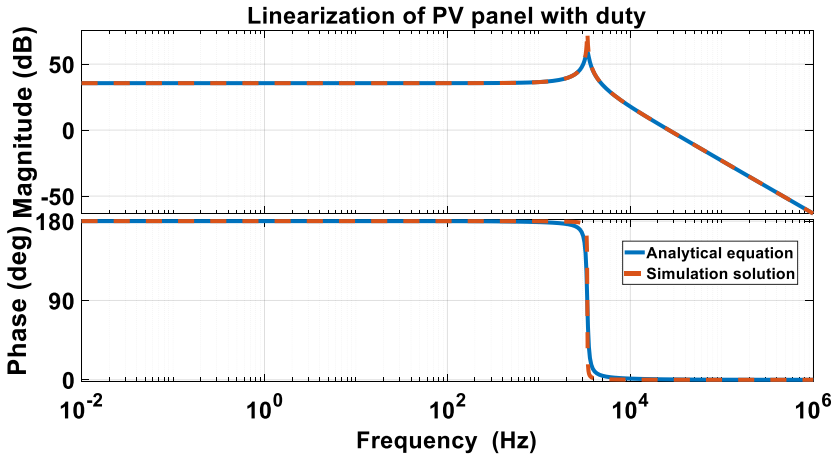

Figure 2-22 Comparison between analytical equation and simulation solution for PV panel with duty

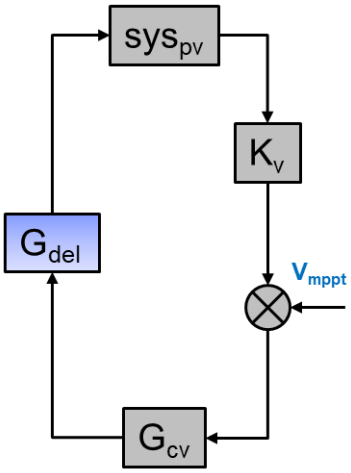

Figure 2-23 Boost converter voltage loop gain block diagram

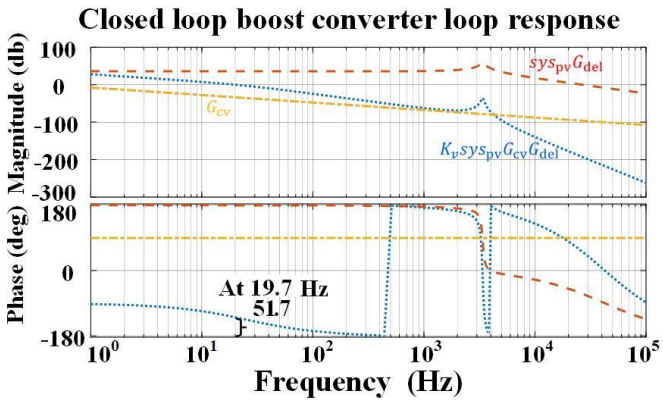

Figure 2-24 Boost converter closed loop response comparison with compensation and plant frequency response

Figure 2-23 shows the block diagram of the loop gain for control to PV panel voltage with input as PV panel MPP voltage. The control to PV panel voltage response is called sys_{pv}. K_v is the antialiasing filter with value 1, and the compensator Gcv was utilized to decrease the error between the measured and MPP voltage of the PV panel. As shown in equation (2-36), the system considers delay in encountering one delay of one switching cycle in the system.

$$G_{\text{del}} = \frac{1 - 0.5T_{\text{del}}s}{1 + 0.5T_{\text{del}}s} \qquad (2\text{-}36)$$

The PI tuner was used in MATLAB to design the compensator G_{cv}; the closed loop boost converter loop responses are shown in Figure 2-24. The loop gain has a crossover frequency of 19.7 Hz and a phase margin of 51.7 °. The designed compensator, as discussed above, was utilized to close the loop and obtain a closed-loop solution under desired PV panel voltage. With the closed loop, the system's transients and settling time have decreased.

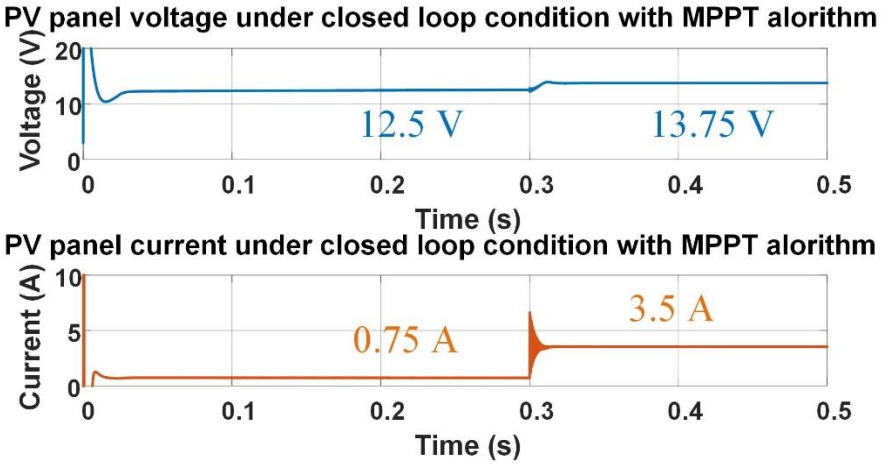

Figure 2-25 PV panel output voltage and current under input voltage closed loop with MPPT algorithm

Perturb and observe (P&O) MPPT algorithm was implemented in a boost converter with PV panel voltage control. P&O utilized PV panel voltage and current; the algorithm evaluates the change in PV panel voltage and power by injecting a small perturbation in PV panel voltage. The algorithm further computes the change in power by the change in voltage ($^{\Delta P}/_{\Delta V}$), if the value is negative, the reference voltage present value is smaller than the past value, and if the value is positive, then the present value is higher than the past value. In this manner, the O.P. will reach MPP and then toggle between the MPP's left and right sides. Using a C-based code, P&O was implemented with a boost converter and PV panel. Initially, the illumination given to the PV panel was 100 W/m^2; after 0.3 seconds, the illumination was increased to 500 W/m^2. With the increase in illumination, the PV panel voltage, and current increase, as shown in Figure 2-25.

2.4 PV Panel Fault Detection using Power Converter:

The Simulink-based monocrystalline PV cell model was simulated with the boost converter model to operate the PV panel under MPP. The AC small signal model of the PV panel was further evaluated under MPP to obtain the AC impedance of the PV panel at MPP and compare the AC impedance under normal and fault conditions.

2.4.1 PV Panel Details:

The PV panel was modeled using 60 monocrystalline PV cells in series; the maximum power of the PV panel was 307 W, the MPP voltage was 33.7 V, and the MPP current was 9.1 A. The model was designed with series resistance 0.046 Ω, shunt resistance 91.8 Ω, and PV panel model parameters are listed as shown in Table 2-4.

Table 2-4 Commercial 300 W PV panel parameters

Cells Type	Monocrystalline	
Number of Cells	60	cells
Maximum power at STC	307	Watts
Voltage at MPP	**33.7**	**V**
Current at MPP	**9.1**	**A**
Open circuit Voltage	**40.45**	**V**
Short Circuit Current	**9.91**	**A**
Temperature Coefficient of Voc	-0.22%	V/K
Temperature Coefficient of Isc	0.40%	I/K
Series Resistance	0.046	Ω
Shunt Resistance	91.8	Ω

The boost converter was designed to provide 60 V output voltage with input power from a PV panel. The PV panel was a model with 50 PV cells in series with 10 PV series in a total of 60 PV cells, as shown in Figure 2-26.

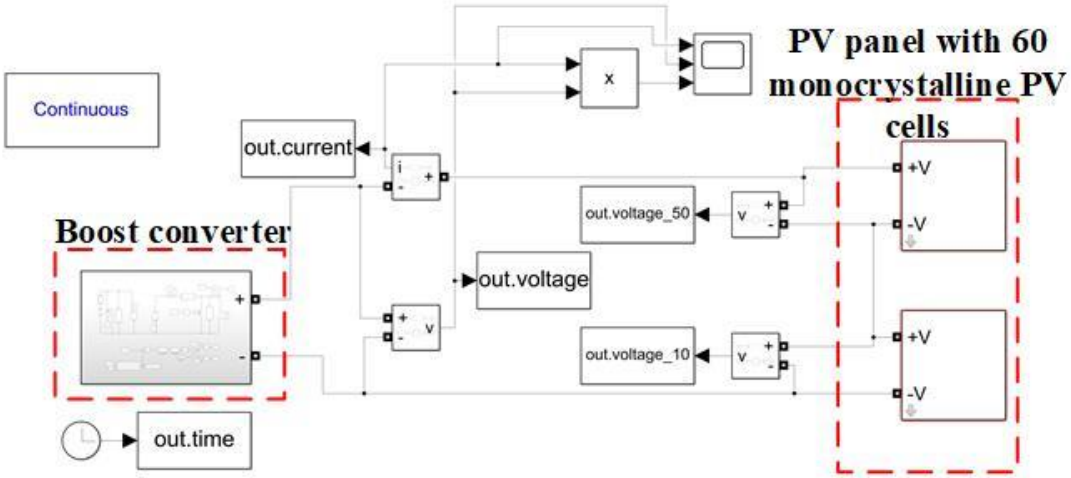

Figure 2-26 Simulink-based PV panel mode with a boost converter

2.4.2 Hot Spot Fault:

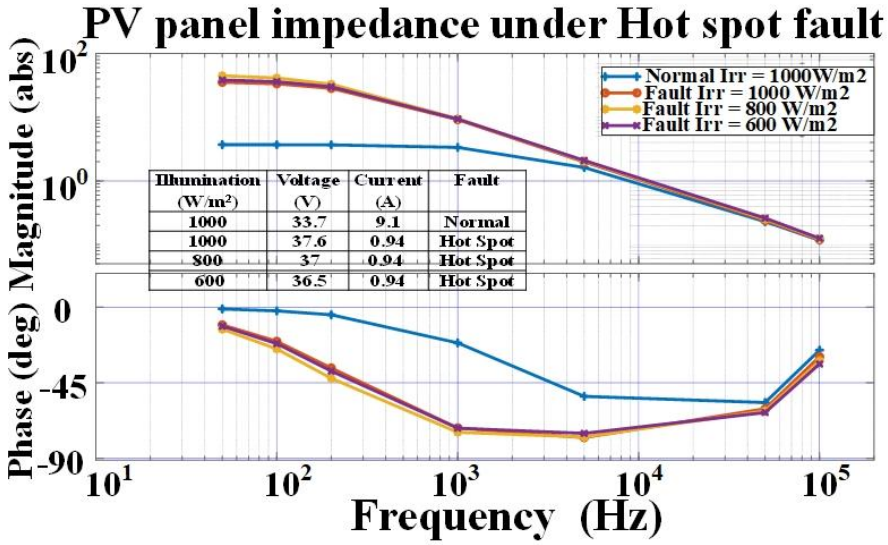

Illumination (W/m²)	Voltage (V)	Current (A)	Fault
1000	33.7	9.1	Normal
1000	37.6	0.94	Hot Spot
800	37	0.94	Hot Spot
600	36.5	0.94	Hot Spot

Figure 2-27 PV panel AC impedance comparison under hot spot fault and normal condition

The hot spot fault was simulated with 10 PV cells at the illumination of 100 W/m^2, temperature of 150 °C, and the rest of 50 PV cells under normal conditions. The PV panel (60 PV cells) was initially modeled for normal conditions with G = 1000 W/m^2 and T = 50 °C. The boost

converter operates the system at MPP, and the O.P. under normal conditions was determined. AC small signal model was simulated with a PV panel under the normal condition O.P, and the PV panel AC impedance magnitude and phase are plotted as shown above. The normal condition result is the benchmark result compared to the fault conditions. Later, the hot spot fault was simulated with a boost converter with 50 PV cells under normal conditions with G = 1000 W/m^2 and T = 50 °C and 10 PV cells under hot spot conditions. The O.P. at MPP was determined, and AC small signal model was simulated to obtain AC impedance under hot spot conditions. Further, the illumination of 50 PV cells was decreased from 1000 W/m^2 to 800 W/m^2 and later to 600 W/$m^{2,}$ and the results are compared as shown in Figure 2-27.

Comparing O.Ps under normal conditions and hot spot fault, the change in all three scenarios is shown in the image above. The voltage increased, and the current decreased w.r.t normal conditions due to hot spot conditions; the change is also observed with different illumination conditions. Comparing AC impedance under normal and hot spot conditions, with an increase in parallel resistance due to hot spot, the impedance magnitude under low frequencies is higher in hot spot conditions than in normal conditions. Also, due to an increase in parallel capacitance under hot spot conditions, the phase decreases in mid-frequencies with comparing the results under normal conditions. Thus, hot spot faults can be modeled with a boost converter and PV panel. Also, AC impedance measurement tests using low and mid-frequency small signals can identify hot spot faults.

2.4.3 The Line-Line Fault:

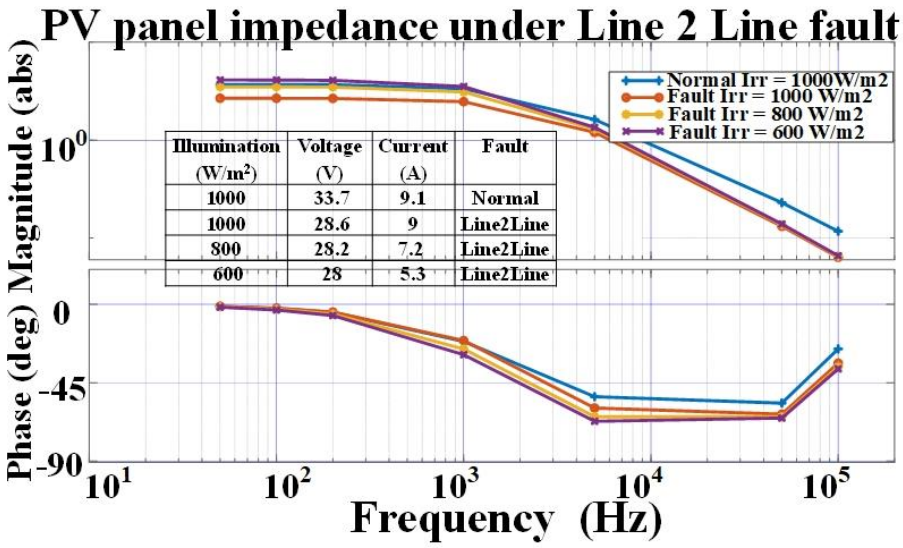

Figure 2-28 PV panel AC impedance comparison under line-to-line fault and normal condition

The line-to-line fault was simulated with 10 PV cells' short circuits and the rest of the 50 PV cells under normal conditions. As the benchmark result discussed above, the normal condition result was compared to the fault conditions. The line-to-line fault was simulated with a boost converter with 50 PV cells under normal conditions with G = 1000 W/m^2 and T = 50 °C and 10 PV cells under short circuit conditions. The O.P. at MPP was determined, and AC small signal model was simulated to obtain AC impedance under line-to-line conditions. Further, the illumination of the PV panel was decreased from 1000 W/m^2 to 800 W/m^2 and later to 600 W/m^{2,} and the results are compared as shown in Figure 2-28.

Comparing O. Ps under normal conditions and line-to-line fault, the change in all three scenarios is shown in the image above. The voltage decreases w.r.t normal conditions due to short circuit conditions; the difference is also observed with different illumination conditions, as 10 PV cells are not contributing to the PV panel voltage. Comparing AC impedance under normal and

line-to-line conditions, with a decrease in resistance due to short circuit conditions, the impedance magnitude under low frequencies is lower in line-to-line conditions than in normal conditions. Also, the phase increases due to a decrease in parallel capacitance under line-to-line conditions. Still, due to a decrease in operating voltage, the effective change in parallel capacitance is a decrease in phase under mid-frequencies with comparing the results under normal conditions. Thus, line-to-line fault can be modeled with a boost converter and PV panel, and also AC impedance measurement test using low and mid, and small high-frequency signals can identify the line-to-line fault.

2.4.4 Junction Box Fault:

The junction box fault was simulated by adding a small resistance of 0.5 Ω between 10 PV cells and the rest of the 50 PV cells. As the benchmark result discussed above, the normal condition result was compared to the fault conditions. The junction box fault was simulated with a boost converter with 60 PV cells under G = 1000 W/m^2 and T = 50 °C and 0.5 Ω resistance in series. The O.P. at MPP was determined, and AC small signal model was simulated to obtain AC impedance under junction box fault conditions. Further, the illumination of the PV panel was decreased from 1000 W/m^2 to 800 W/m^2 and later to 600 W/m^{2,} and the results are compared as shown in Figure 2-29.

Comparing O.Ps under normal conditions and junction box fault, the change in all three scenarios is shown in the image above. The voltage decreases w.r.t normal condition due to adding a series resistance in junction box fault conditions; the change is also observed with different illumination conditions. Comparing AC impedance under normal conditions and junction box fault conditions, the impedance magnitude under high frequencies is higher in junction box fault conditions than in

normal conditions as under higher frequencies, the effect of series resistance at the resonating point is noticed, and due to adding of series resistance, the cumulative resistance will be higher. Also, due to the increase in series resistance under junction box fault conditions, the phase increases at high frequency as the effective resistance has increased. Thus, junction box faults can be modeled with a boost converter and PV panel. Also, an AC impedance measurement test using a small high-frequency signal can identify junction box faults.

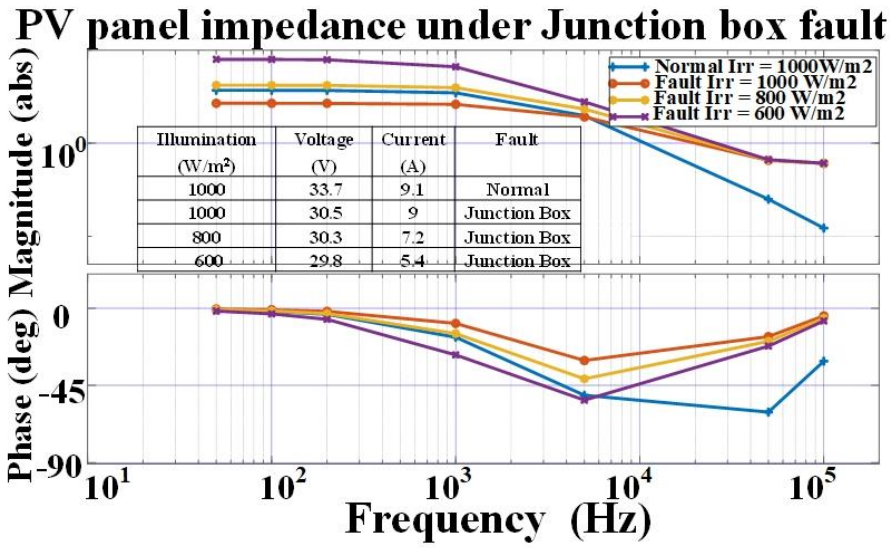

Figure 2-29 PV panel AC impedance comparison under junction fault and normal condition

2.4.5 DC Link Capacitor Fault:

The boost converter has a DC link capacitor parallel to the PV panel; the capacitor helps provide a switching current to the converter. Under normal operation, the impedance of the PV panel will always be calculated with an impedance of the PV panel and dc-link capacitor in parallel. Later with the knowledge of capacitors, the PV panel impedance can be computed. With the age of the power converter, the life of the capacitor decreases, causing the capacitance to reduce

and increase in the ESR of the capacitor. These effects can cause an increase in ripple voltage and current from the PV panel. The manufacturer claims capacitor end-of-life (EOF) as a decrease in capacitance by 20% and an increase in ESR by twice. The normal condition was simulated by adding a capacitance of 180 μF and 18 mΩ in parallel to the PV panel model under G = 1000 W/m^2 and T = 50 °C. The capacitor fault scenario was simulated with the capacitance of 144 μF and 36 mΩ parallel to the PV panel model under G = 1000 W/m^2 and T = 50 °C. The O.P. at MPP was determined, and AC small signal model was simulated to obtain AC impedance under normal and capacitor fault conditions.

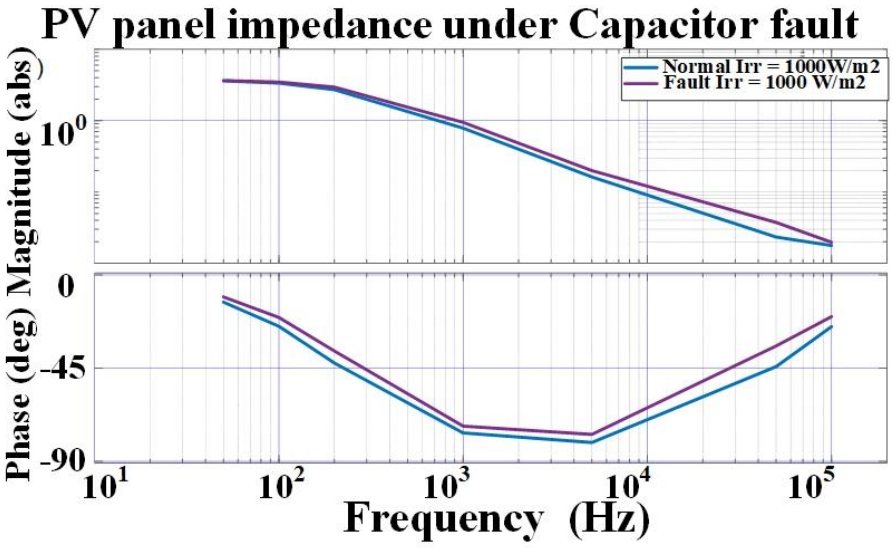

Figure 2-30 Boost converter input AC impedance comparison under capacitor fault and normal condition

The change in comparing O.Ps under normal conditions and capacitor fault is shown in Figure 2-30. Under mid and high-frequency regions, the AC impedance magnitude of capacitor fault is higher than in normal conditions. Due to an increase in ESR and a decrease in capacitance under the EOF of the capacitor, the effective change has caused to increase in impedance

magnitude, as shown in the image above. A reduction in capacitance and an increase in ESR also cause an increase in the impedance phase, as seen in the impedance phase in the image above.

2.5 Conclusion:

Table 2-5 PV panel fault indicator comparison using AC impedance measurement

% change						
	Normal with Irradiance ↓	Fault-Hot Spot	Fault-Line to Line	Fault-Open Circuit	Fault-Junction Box	End of life - CAPACITANCE
Voltage	<5% ↓	> 10% ↑	> 10% ↓	> 30% ↓	< 10% ↓	> 90% ↑ (P2P)
Current	> 10% ↓	> 50% ↓	< 3% change	< 1% change	< 1% change	> 80% ↑ (P2P)
Magnitude	> 20% ↑	> 100% ↑ @ 50 Hz	> 30% ↓ @ 50 kHz	> 30% ↓ @ *50 Hz*	> 100% ↑ @ 50 kHz	> 25% ↑ @ 1 kHz > 80% ↑ @ 10 kHz
Phase	< 3% change	> 20% ↓ @ 1 kHz	< 1% change	< 1% change	> 20% ↑ @ 50 kHz	< 3% change

The boost converter with a PV panel model can detect hot spot faults, line-to-line faults, open circuit faults, junction box faults, and EOF of a capacitor using effective change in the operating points and with change in AC impedance magnitude and phase under at the MPP. The PV panel's illumination during the day changes due to a change in the sun's irradiance falling on the PV panel. The difference in illumination also changes the MPP, and with the shift in O.P., the AC impedance also changes. Table 2-5 shows the effects of change in illumination on PV panels with a decrease in illumination. To identify a PV panel fault, the fault detection nature should be distinctive for all the faults and different from the change in illumination under normal conditions. The fault indicators, as mentioned above, can be helpful to identify faults using AC impedance small signal PV cell model with O.P. at MPP of PV panel.

Chapter 3 Photovoltaics Panel Impedance Measurement using Offline Technique

3.1 Introduction

Analyzing I-V characteristics of a PV cell in simulation under different operational points, the nature of current and voltage varies. PV panel impedance fluctuates with changes in operating point, temperature, and illumination. The offline technique discussed in this chapter utilizes equipment to measure PV panel impedance and gather a benchmark to compare PV panel impedance measured using Simulink- based model and can be further compared with the online technique discussed in the next chapter. The procedure followed in the offline impedance technique to illuminate the PV panel, measure the operating point, and inject a small signal into the PV panel to measure impedance is also repeated in the online impedance measurement technique to evaluate the effectiveness of online impedance measurement. The conditions for creating a PV panel fault mentioned in the offline impedance measurement technique are repeated in the online impedance measurement technique.

3.2 Photovoltaics Cell I-V Characteristics

3.2.1 Forward Bias Condition

PV cell forward I-V characteristics are determined by experimental tests, as shown in Figure 3-1. A monocrystalline PV cell with the parameters given in Table 3-1 was illuminated using an LED sheet to illuminate the PV cell. The LED sheet can provide 3400 lumens and consumes 36 W power under 24 V DC voltage. With illumination, the photocurrent current of the PV cell sources power to the electronic load, as shown above. With the change of illumination, the

PV cell current will increase; thus, to maintain an MPP, the resistance of the electronic load was decreased.

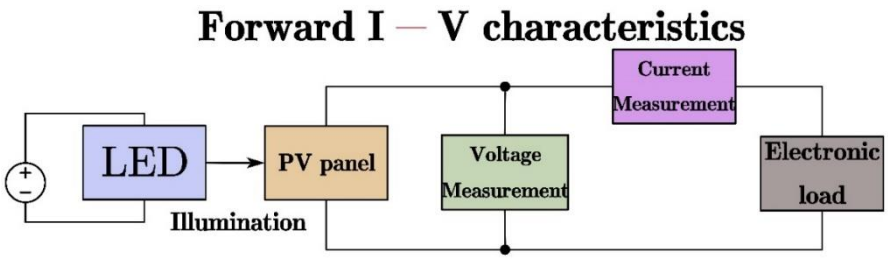

Figure 3-1 Forward-biased PV cell I-V characteristics measurement block diagram

Table 3-1 Commercial monocrystalline PV cell parameters

Detail	Value	Unit
Maximum power	5	W
Maximum power point voltage	0.558	V
Maximum power point current	9.09	A
Open circuit voltage	0.665	V
Short circuit current	9.65	A
Dimension	156.75*156.75	mm^2

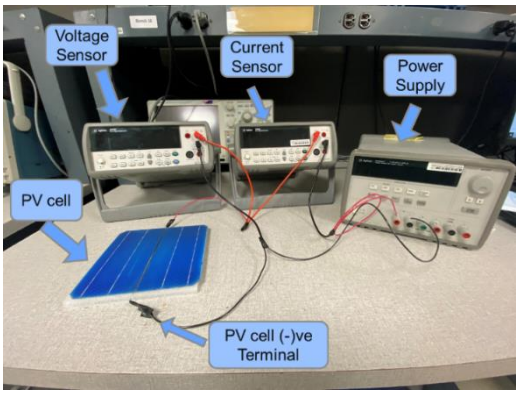

Figure 3-2 Hardware setup for PV cell I-V characteristics

Figure 3-3 PV cell with LED sheet

The experimental setup is shown in Figure 3-2; the PV cell's positive and negative terminals are connected to the voltage sensor to measure the voltage across the PV cell. The positive terminal is further connected to the current sensor positive terminal to measure the current sourced by the PV cell after being illuminated. The PV cell was illuminated using an LED sheet, and the LED sheet was biased with an external power supply; with 20 V across the LED sheet, the sheet provides illumination of 60 W/m2, and with an increase in biased voltage, the illumination increases. The PV cell was kept in an enclosed box to avoid illumination from the surroundings and avoid 60 Hz AC mains frequency in light from the external source, as shown in Figure 3-3.

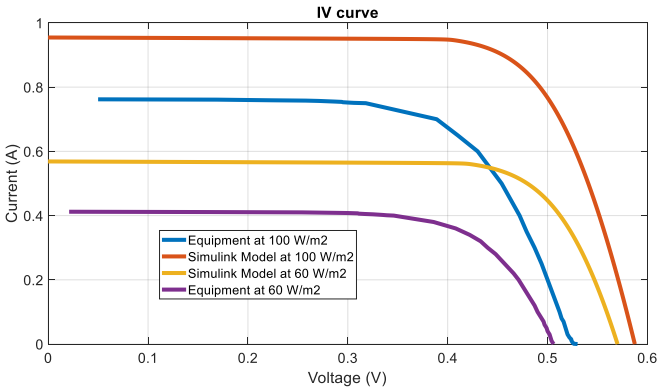

Figure 3-4 PV cell I-V characteristics comparison between Simulink model and experiment at 60 W/m^2 and 100 W/m^2 illuminations using Figure 3-1

An illuminated PV cell was connected to BK precision 8500 electronic loads to sink the current from the PV cell. Agilent 34405 A multimeter was used to sense the voltage across the PV cell and the current flowing from the PV cell. The illuminated PV cell sources current to the electronic load, and with a change in resistance, the PV cell current and voltage vary. The forward I-V characteristics of PV cell under illumination is shown above. The illumination was changed from 60 W/m^2 to 100 W/m^2 by increasing the bias voltage across the LED sheet. The PV cell forward I-V characteristics are compared with the Simulink model under the illumination of 60 W/m^2 and 100 W/m^2 and are shown in Figure 3-4. The Simulink model PV cell internal parameters are considered via literature; thus, the I-V characteristics of experiment and Simulation vary. The figure above shows that with an increase in the illumination, the PV cell current increases for the Simulink model and the offline hardware experiment. Also, constant current-like behavior was observed under voltages below MPP, and with an increase in voltage after MPP, the current decreases rapidly in Simulation and experimental data. The open circuit voltage and short circuit

current appear different for all the conditions due to different internal parameters of the PV cell and changes in illumination on the PV cell.

3.2.2 Reverse Bias Condition

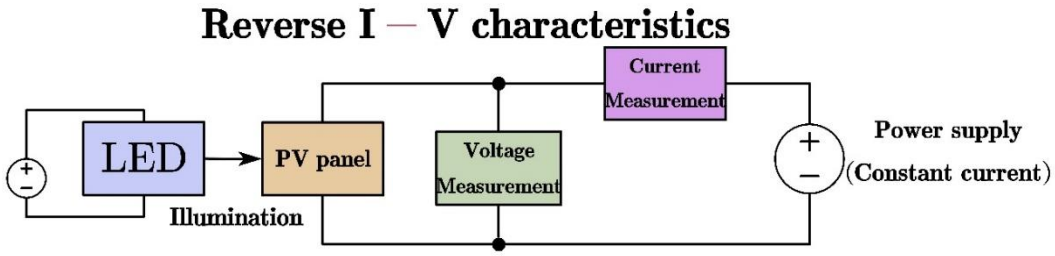

Figure 3-5 Reverse biased PV cell I-V characteristics measurement block diagram

The illuminated PV cell reverses I-V characteristics are measured using the block diagram as shown in Figure 3-5. The PV cell was biased with negative voltage using a power supply, as shown in the block diagram. Due to illumination, the PV cell will source current rather than a sink; thus, the power supply must have the capability to sink current from the PV cell.

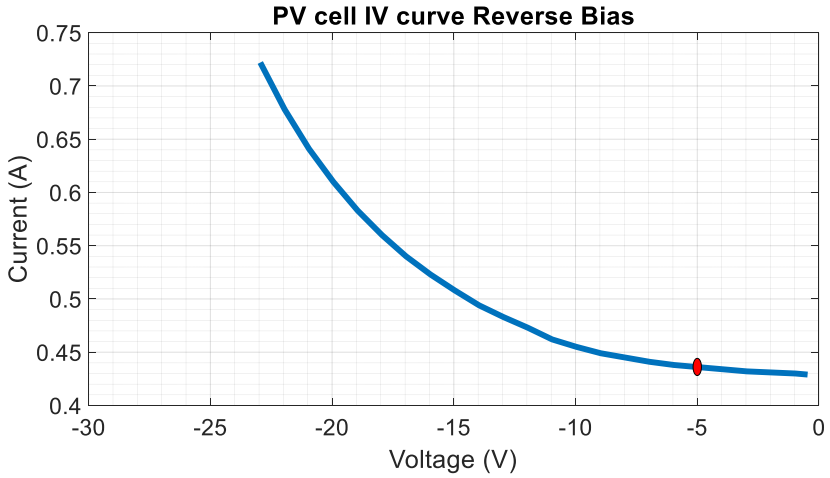

Figure 3-6 PV cell reverse bias I-V characteristics using Figure 3-5 test setup

The reverse I-V characteristics of the PV cell under 60 W/m^2 illuminations is shown in Figure 3-6, the PV cell was sourcing current under illuminated condition, and thus the PV panel current was positive. The reverse biased condition by the power supply maintains the negative voltage across the PV cell; thus, the I-V characteristics are in the second quadrant of the graph. Before the reverse breakdown voltage of the PV cell, the PV cell current was constant and didn't change due to the high impedance of the PV cell. With the increase in the reverse voltage after the reverse breakdown voltage across the PV cell, the PV cell current increases exponentially due to the PV cell's avalanche breakdown and diode tunneling effect. The similar nature of PV cell I-V characteristics under illumination and reverse bias is seen in the Simulation above. Beyond the reverse voltage of -23 V across the PV cell, the power supply cannot supply a higher reverse voltage, and thus the measurement was stopped.

3.3 Offline Impedance of Photovoltaics Cell

3.3.1 Equipment Details

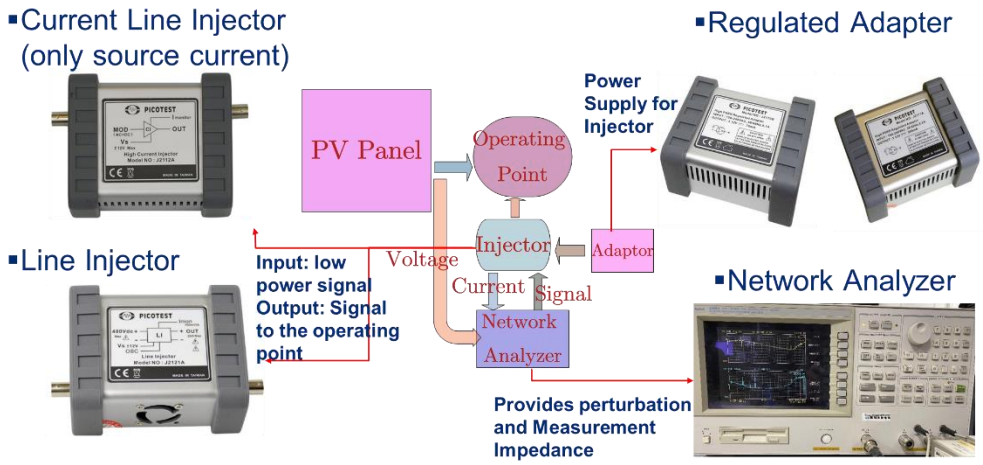

Figure 3-7 Equipment details for AC small signal injection and measurement

The IV characteristics help determine the operating point for measuring the impedance of the PV cell. If the operating point is at the slope, then impedance can be measured with less power in the perturbation signal (magnitude of sine wave). If the point is in the linear region, then the power for the perturbation signal will be higher as the change in current will be governed by a change in voltage for a PV cell. Figure 3-7 shows the block diagram for the small-signal injection in the PV cell at a particular operating point to measure the impedance of the PV cell. The impedance was measured using the network analyzer Agilent 4395A, and the incoming and outgoing signals from the network analyzer were transported using BNC connectors. The network analyzer injects small signal perturbation, the sine wave was swept with the power of 0dbm from bandwidth 100 Hz to 200 kHz, and the voltage measured via terminal A and current measured via terminal B was divided using A/B computation in network analyzer to measure the impedance of PV cell. The incoming signal to the network analyzer passes through the 1 MΩ line input adapter Agilent 41802A to avoid high current from the system to the network analyzer. The bandwidth to

measure impedance at the fundamental frequency was kept at 2 Hz, and thus it takes 5 minutes as an operation time to compute impedance with 200 frequency data points. The PV panel impedance was measured at an operating point where the voltage and current are at MPP or near MPP, the small signal perturbation will be added on the operating point, and thus line injector or current injector was needed to add the perturbation on the operation point. The injector used was Line Injector J2121A for voltage injection if the perturbation was added to the voltage, and Current Injector J2112A can also be used for small signal perturbation injection in current. Regulated adapters J2170B and J2171A are used for the current and voltage injectors. Both the injector provides the sense current, i.e., senses the current flowing from the injector. The sense current from both injectors has a gain of 0.1V/A.

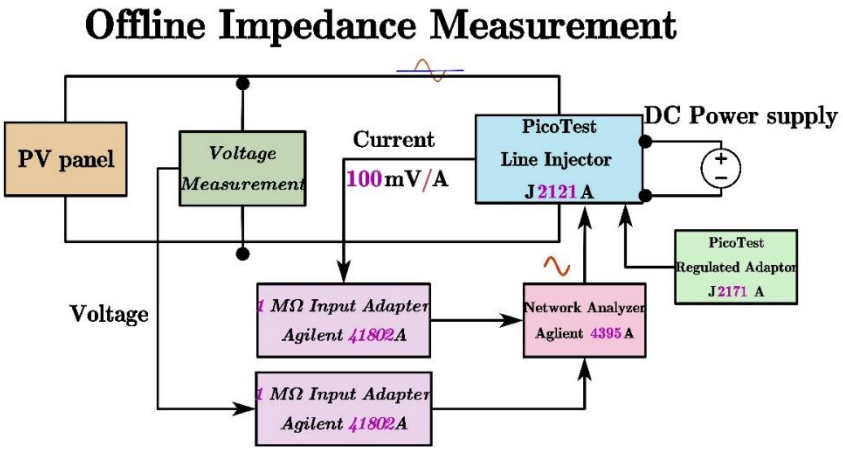

Figure 3-8 Offline AC impedance measurement for PV cell using voltage injection with equipment as shown in Figure 3-7

Figure 3-8 shows the block diagram for measuring PV cell impedance offline. The PV cell was illuminated at 60 W/m^{2,} and the PV cell current was sourced to the power supply. The line

injector PicoTest J2121A was used to inject voltage perturbation to an operating point. The operating point was set using a DC power supply; thus, with the operating point given by the power supply, the injector adds the small signal perturbation to the operating point and applies the voltage across the PV cell. The hardware setup for measuring PV cell impedance is shown in Figure 3-9.

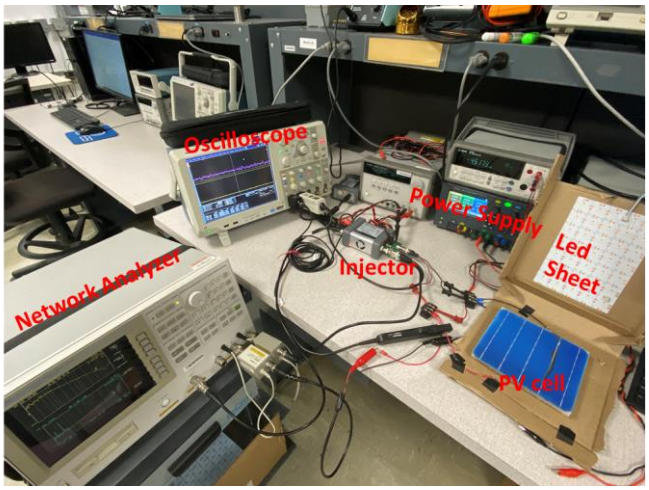

Figure 3-9 Hardware setup for offline AC impedance measurement of PV cell

The PV cell current was measured through a line injector and given to the network analyzer B terminal to compute impedance (A/B). The network analyzer injects a small signal into the line injector. The PV cell voltage was measured directly and given to the network analyzer. A terminal, the network analyzer with a 1 MΩ input adapter, has a maximum voltage rating of up to 50 V.

3.3.2 Offline Impedance Measurement of Photovoltaics Cell

The PV cell under 60 W/m^2 illumination I-V characteristics comparison between Simulation and hardware is shown in Figure 3-10. The operating point to measure impedance is marked with a red dot on the I-V characteristics; for simulation, the voltage setting was 0.55 V, the current was 0.2 A for hardware setup, the voltage setting was 0.55 V, and the PV panel current

was -0.35 A. The current being negative was due to the power supply sourcing the current to the PV cell.

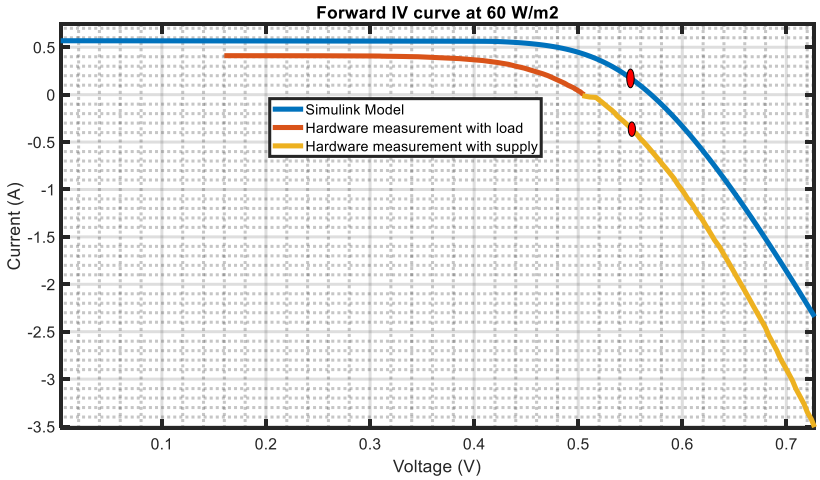

Figure 3-10 PV cell forward bias I-V characteristics comparison with operating points for AC small signal injection

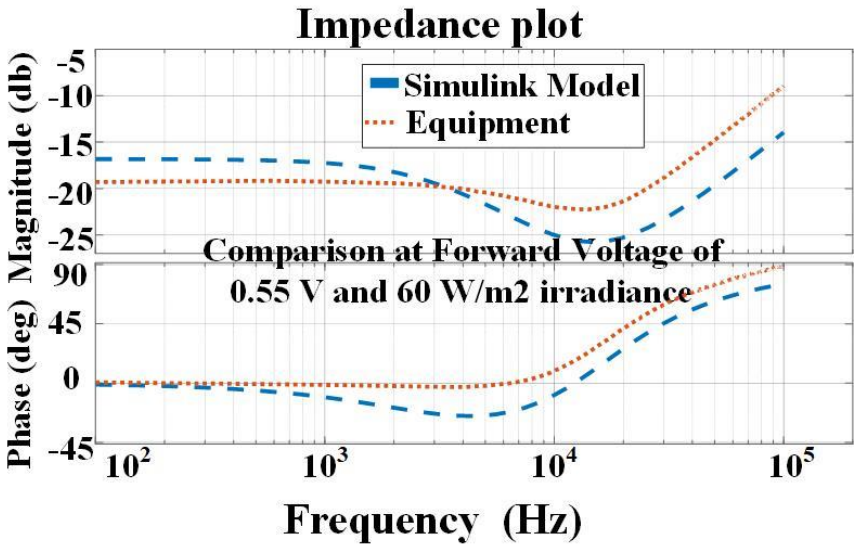

Figure 3-11 PV cell AC impedance comparison between Simulink model and hardware experiment at O.Ps as shown in Figure 3-10

With the operating points mentioned above, the illuminated PV cell impedance was measured using the test setup discussed above. The impedance plot comparison between the Simulation and hardware setup is shown in Figure 3-11. Under low-frequency regions, both conditions' impedance magnitude constantly shows a resistive behavior. The capacitive nature can be observed in the mid-frequency region, where the impedance magnitude and phase decrease. The impedance magnitude and phase increase under high frequency due to the inductance nature can be seen in both plots. The results don't overlap due to different internal parameters, operational points, and parasitic involved due to hardware setup. Still, the general trends of impedance can be observed in both results.

Figure 3-12 AC small signal perturbation in PV cell voltage and current and reference current under low frequency at left plot and high frequency at right plot

Figure 3-12 shows the waveforms of the illuminated PV panel under reverse biased voltage of -5 V, the voltage measured via TPP1000 voltage probe, current via current probe TCP0030A and sensed current measured via injectors. Under low frequency, small signal perturbation was added to the operating point using a voltage injector. The PV panel waveform is shown in yellow; due to the high impedance nature under reverse bias conditions at low frequency, the small signal perturbation in the blue waveform is significantly low, and thus the measured current seen in pink via injector is also low. With the increase in frequency, the impedance of the PV cell decreases the due effect of capacitance; at the mid-frequency region, the waveforms of PV cell voltage, PV cell current, and measured current via injector are shown above. With low PV cell impedance magnitude, the small signal perturbation in current will be higher than the low-frequency perturbation and can be compared with the figure above.

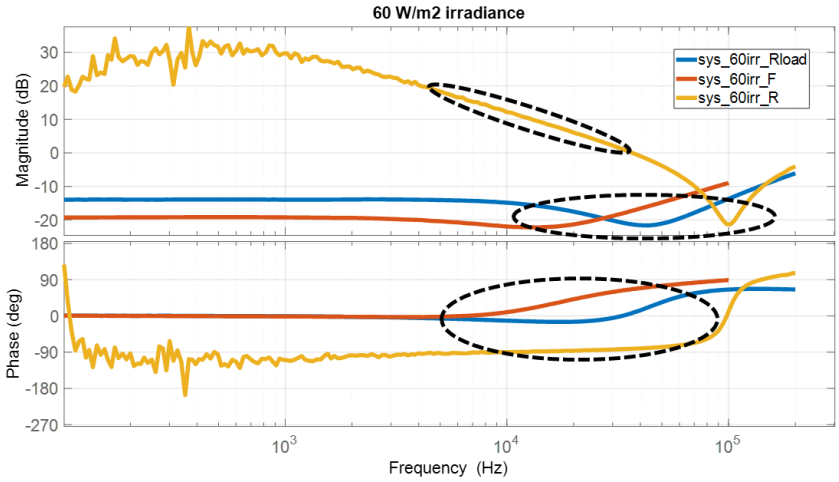

Figure 3-13 PV cell offline AC impedance at forward and reverse bias condition comparison

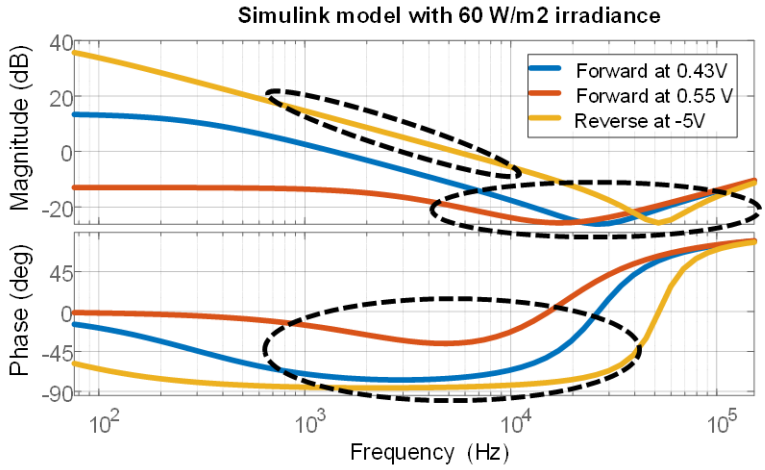

Figure 3-14 Simulation-based PV cell AC impedance with O. Ps similar to Figure 3-13

Further, the PV cell under 60 W/m^2 illumination was tested under forward and reverse-biased conditions. The experimental results, as shown in Figure 3-13, are compared with the simulation results in Figure 3-14. Three operating points are used for comparison keeping illumination and temperature the same. The impedance at 0.43 V, termed O.P. 1, was measured and plotted in blue under forward conditions, PV cell sources voltage, and current to the external

load. The impedance at 0.55 V, termed O.P. 2, was measured and plotted in orange; with higher PV cell voltage, the power supply sources the current to the PV cell, and the PV cell voltage was forward-biased. The impedance at -5 V, termed as O.P. 3, was measured and plotted in yellow; under reverse biased conditions, the PV cell sources current; thus, the power supply across the PV cell sinks the PV cell current and maintains reverse biased voltage. The impedance characteristics for all three O. Ps are compared with the Simulink model maintaining similar illumination and temperature. The general trend of PV cell impedance is observed in both figures, as shown above. Considering the experimental result, the PV cell impedance magnitude under low frequency decreases from O.P. moving left to the right side of MPP; a similar can be seen in the figure. Assuming series resistance is identical in all three tests, the parallel resistance dominates under low frequency; thus, the parallel resistance decreases with O. Ps moving to the right of MPP. The resonating frequency due to the inductor and capacitor is shifted to the left with O. Ps going to the right; thus, the parallel capacitance increases with O. Ps moving to the right of MPP. The simulation-based result shows a similar nature of parallel resistance and parallel capacitance. The results from the experiment don't match the result from the Simulation due to differences in the internal parameters of the PV cell and parasitic involved in the hardware setup.

3.4 Offline Impedance Measurement of PV panel

3.4.1 Under Dark Condition with 0 W/m^2 Illumination

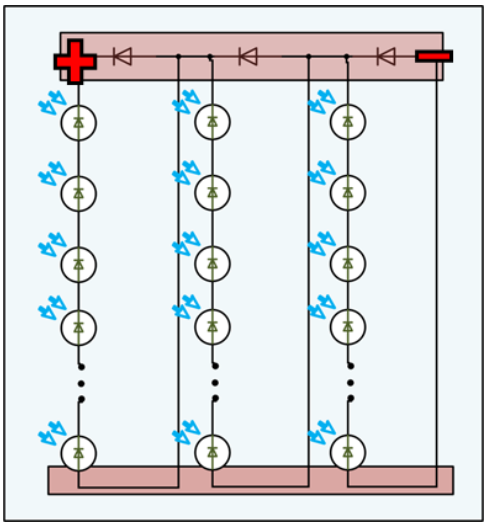

Figure 3-15 PV panel diagram with PV cell connected in series and junction box with three bypass diodes

Table 3-2 Commercial 300 W PV panel used for AC impedance measurement

Details	Values	Units
Company	Grape Solar	
Cells Type	Monocrystalline	
Number of Cells	60	cells
Maximum power at STC	300	Watts
Standard temperature	25	degrees
Standard Irradiance	1000	W/m2
Voltage at MPP	**32.48**	**V**
Current at MPP	**9.24**	**A**
Open circuit Voltage	**40.45**	**V**
Short Circuit Current	**9.91**	**A**
Module Efficiency	18.40%	
Temperature Coefficient of Voc	-0.28%	per °C
Temperature Coefficient of Isc	0.04%	per °C
Temperature Coefficient of Pmax	-0.38%	per °C
Length	1640	mm
Width	992	mm
Thickness	40	mm

A PV panel with 60 monocrystalline PV cells connected in series was purchased. The PV panel characteristics can be seen in Table 3-2. The Panel was kept on the mounting racks at an angle of 60°. The PV panel contains three bypass diodes in the junction box; a similar configuration can be seen in Figure 3-15. Early in the satellite system, due to shading or partial shading on the PV cell, PV cells use to undergo permanent damage. The prevention technique is commonly called bypass diode; the bypass diode provides an alternate current path when the PV cells undergo negative biasing due to the reverse property of shaded PV cells. Studies have shown that hot spotting is a major cause of PV panel performance degradation, even with a bypass diode connected across the PV cell. Once a PV cell is damaged, it becomes a weak point in the string that causes performance reduction of the entire PV panel. The hot spot damage could be avoided if bypass diodes were placed across several PV cells. The cumulative reverse bias power

dissipation through a shaded PV cell is proportional to the number of cells attached to the PV string. One bypass diode is kept in series to 20 PV cells, thus totaling up to 3 bypass diodes for 60 PV cells.

Figure 3-16 PV panel under dark condition

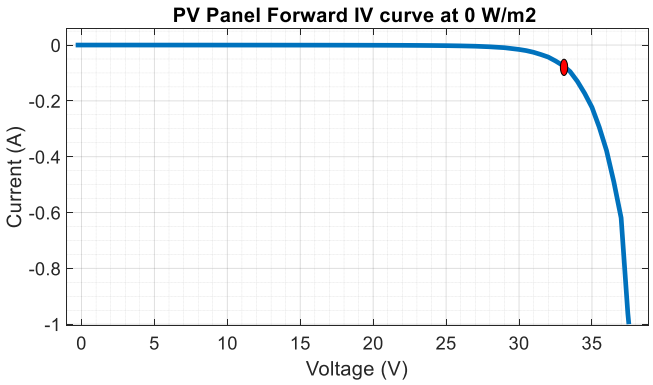

Figure 3-17 PV panel forward I-V characteristics under dark condition

PV panel I-V characteristics under forward bias conditions were measured with illumination 0 W/m^2. For dark conditions, with the illumination of 0 W/m^2, a reflective tarp was used to place it over the PV panel; thus, the light from outside was blocked by the reflective trap, as shown in Figure 3-16. The positive and negative terminals of the junction box are the terminals of the PV panel to measure the voltage across the PV panel and current into the PV panel under dark conditions. The experimental method used to measure forward I-V characteristics for a PV panel was the one used above to measure forward I-V characteristics of a PV cell. The PV panel was operated under dark conditions; thus, the PV panel will sink current as the current produced by the photodiode was proportional to the illumination on the PV panel. Under dark conditions,

the illumination was 0 W/m^2. The PV panel voltage was set by a power supply connected across the PV panel; the voltage was swept to measure the I-V characteristics of the PV panel shown in Figure 3-17. The current, as observed in the figure above, is negative. Thus PV panel is sinking current from the power supply. With the increased illumination, the I-V curve will shift upwards from the 4th quadrant to the 1st quadrant of the graph.

3.4.2 Solar Simulator

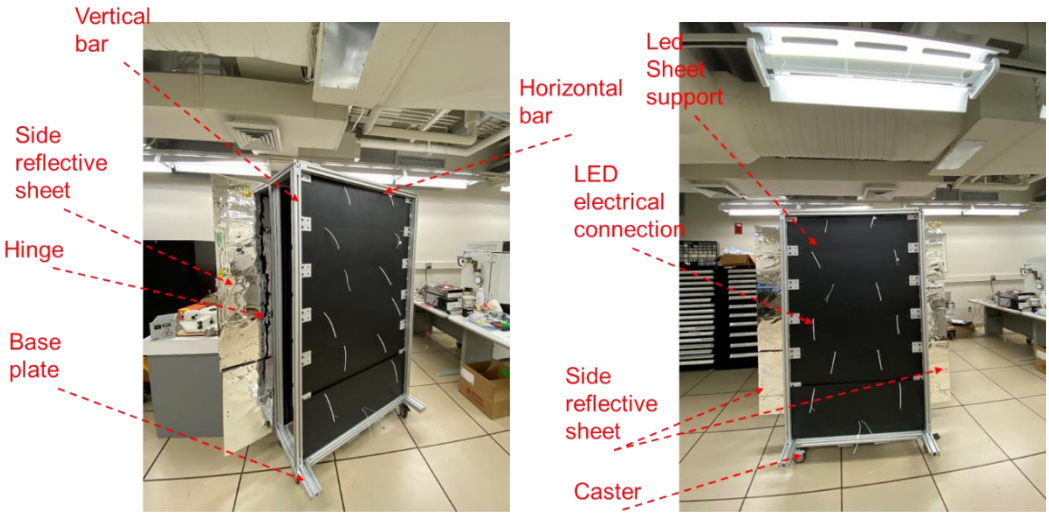

Figure 3-18 Solar simulator for illuminating PV panel using LED sheets and reflection sheets

A panel rack structure was designed and modeled in Inventor software for illuminating PV panels using LED sheets, structure strength, and mobility. The design used aluminum T-slot bars to deliver structure holding and stability. The base of the structure has a caster for mobility access. The left, right, top, and bottom sides have reflective sheets to reflect the illumination on the PV panel. The structure was built and assembled at the CPES facility. Figure 3-18 shows the Panel rack with PV panel, reflective sheet, and LED, and the support structure mounted on the caster with LED sheets connects open. The PV panel was attached to one of the sides with LED sheets,

and its support was parallel to the PV panel. The height of the structure is 64.6 inches, like the PV panel height; the reflective sheets are attached with hinges to access the PV panel front view, as seen in the figure keeping the distance between LEDs and the PV panel at 15 inches. 13 LED sheet combination was used to illuminate the PV panel as seen in figure with a width of panel rack 42 inches. The LED sheet used in the panel rack to illuminate the PV panel has 576 LEDs sinking 120 W power with 12000 lumens at 24 V biasing voltage. Two LED sheets, in combination, are connected to ABS sheets to maintain the strength of the structure. 3M specular reflective film was used for reflection in panel rack affix on ABS sheet to maintain rigidity.

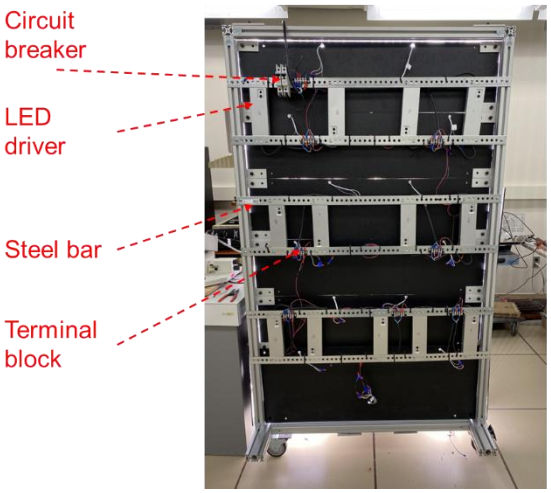

Figure 3-19 Front views of the solar simulator with LED drivers and circuit breaker

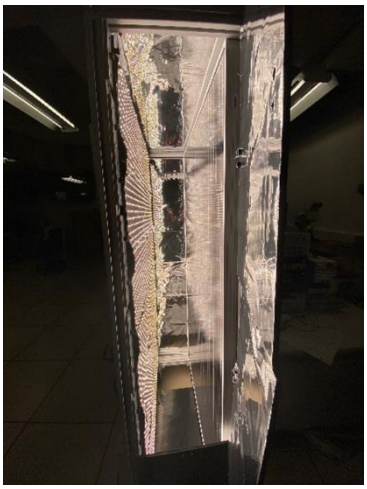

Figure 3-20 Side view of solar simulator illuminated

LED sheets are powered using AC/DC LED driver with adjustable output voltage and current for 13 LED sheets, and 13 AC/DC LED drivers are connected in parallel. The converters with an output voltage of 24 V are attached to the panel rack using a slotted steel bar. A circuit

breaker of 25 A was connected in series for AC connection, and a terminal block was used to connect AC points to all AC/DC converters, as seen in Figure 3-19. The LED sheet illumination with PV panel in parallel and reflective sheet at sides are shown in Figure 3-20. The panel rack was powered with AC mains and a standard AC plug socket consuming a current of 15.6 Arms. The converter with 24 V output voltage across the LED sheet provides an illumination of 300 W/m^2 over the PV panel with reflective sheets flaps closed; illumination was measured using a Fluke irradiance meter.

3.4.3 PV Panel Impedance Measurement under Normal Conditions:

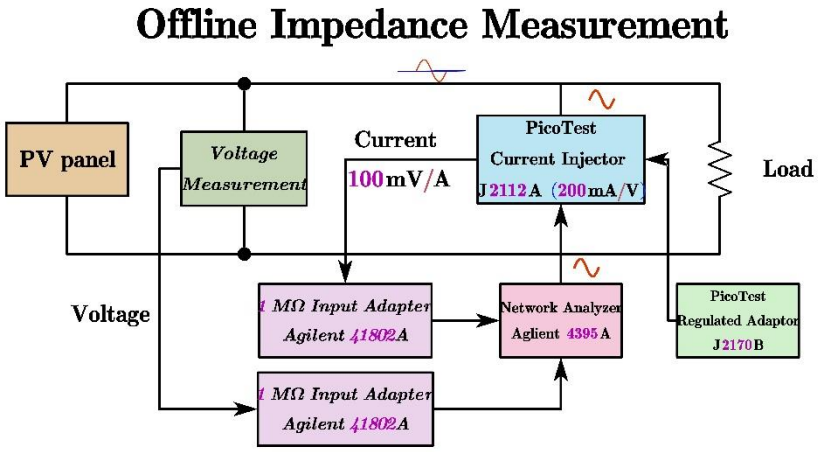

Figure 3-21 Offline AC impedance measurement of PV panel using current injection

`Illuminated PV panel offline impedance measurement block diagram is shown in Figure 3-21. The PV panel was illuminated, and the current was sinking to the external load connected to the PV panel. The PV panel current and voltage change with a change in the external load. The operating point was selected for measuring offline PV panel impedance; a small signal perturbation in current was injected into the PV panel using the current injector PicoTest J2112A. The current

injector behaves as a voltage-controlled current source with a gain of 200 mA/V, the small signal perturbation in voltage was given by the network analyzer. The current injector was parallel to the PV panel and the external resistive load; the current will get divided based on the effective impedance of the PV panel and the load. The small signal current injected into the system was obtained through the current injector, the voltage across the PV panel was measured, and impedance was computed using a network analyzer. The impedance obtained has an effective impedance of the PV panel in parallel with the external resistive load; MATLAB was used to calculate PV panel impedance by compensating the effect of resistive load.

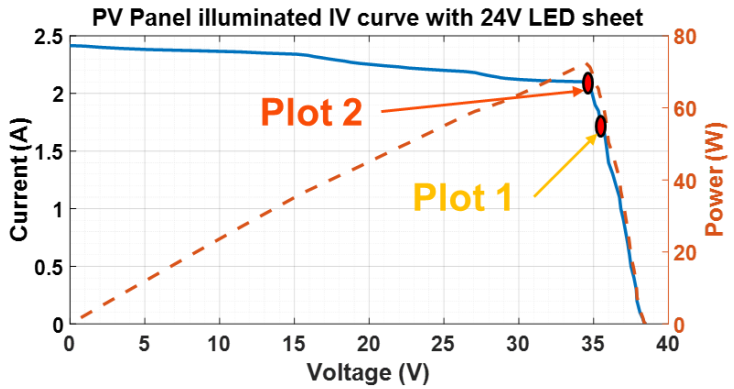

Figure 3-22 PV panel I-V characteristics with 300 W/m^2 illuminations under normal condition

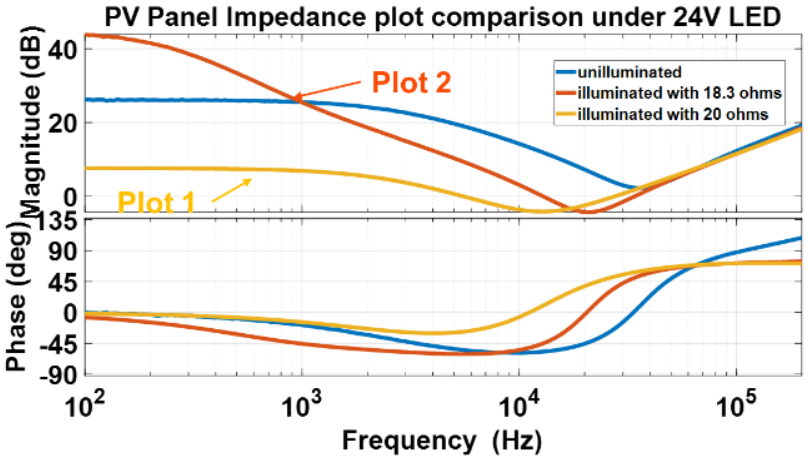

Figure 3-23 PV panel offline AC impedance comparison with O. Ps as shown in Figure 3-22

The illuminated PV panel I-V characteristics is shown in Figure 3-22. The MPP power from the PV panel under the illumination of 300 W/m^2 was 75 W. The two points marked in the figure above are used to measure the impedance of the illuminated PV panel. The impedance plot compares three different situations as shown in Figure 3-23; 1st is an unilluminated condition where the PV panel was kept in the dark with 0 W/m2 illuminations, plot 2 is the impedance plot for point 1 under the illuminated condition where the point is slightly below MPP and 20 Ω

resistive load to the sink power of PV panel. The 3rd condition is point 2 of the illuminated condition, where the point is at the left side of MPP, and 18.3 Ω is used as the resistive load to sink power of the PV panel. Comparing plot one and plot two from Figure 3-23, under MPP conditions, the PV panel impedance is low in the low frequency of plot one than in plot 2. Plot 2 falls on MPP's left side, and the voltage change is greater. Also change in current is low, and thus impedance is higher in plot 2. As mentioned above, under O.P. on the left side of the I-V characteristics, the parallel resistance increases, and parallel capacitance decreases; thus, the resonating point shifts to the right. Plot 1 is considered for normal conditions and is further used for comparison with the fault conditions.

3.4.4 PV Panel Impedance Measurement under Hot Spot Fault:

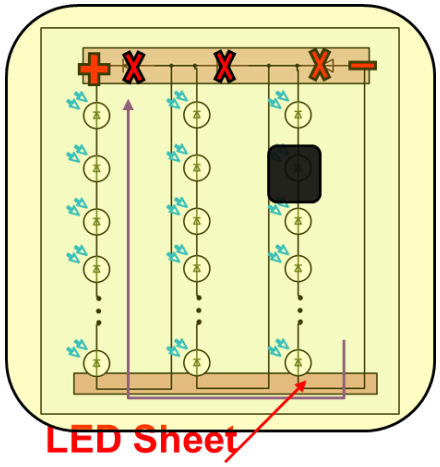

Figure 3-24 Illuminated PV panel diagram under hot spot fault

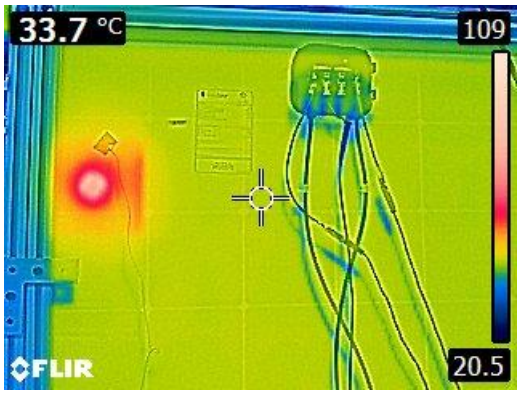

Figure 3-25 PV panel hot spot temperature measurement using a thermal imager

Under Hot spot conditions, the shaded PV cell goes in the reverse biased state; the voltage across the shaded PV cell is negative and is sourcing current, and the PV cell-shaded will sink

power rather than sourcing it. Due to sinking PV panel power, the temperature of the PV cell will increase, and the PV cell can be permanently damaged due to excess heating. The damaged PV cell leads to a hot spot in the PV panel. The PV industry uses a bypass diode to avoid hot spot conditions. The bypass diode blocks the current flow from the PV string with shaded PV cells as the PV string voltage will be negative under higher percentage shading conditions of the PV cell. Under harsh weather conditions and fluctuating shading conditions, the bypass diode might fail. Due to shading conditions, the shaded PV cell with a faulty bypass diode in the PV string will be damaged, leading to hot spot conditions.

Figure 3-24 shows the test scenario of shading one PV cell of the illuminated PV panel with the bypass diode open-circuited. With the PV cell shaded and maximum power being sunk through the PV panel, the temperature of the shaded PV cell increases rapidly. The change in temperature of the shaded PV cell depends on the series and parallel resistance of the PV cell. Figure 3-25 shows the temperature of the shaded PV cell, the temperature increase was 85 °C, and the temperature increase for the unshaded PV cell was 15 °C. The test was performed for 5 minutes, and the Figure above was taken after the 5th minute using FLIR E5 thermal imager.

3.4.4.1 Single PV Cell Hot Spot:

Figure 3-26 shows the I-V and P-V curve comparison of the illuminated PV panel's normal and shading (1 PV cell shaded) conditions. Comparing the shaded condition curve with the normal state, the shaded PV cell reverses voltage increases under a high voltage region as the current is low. Point 3, marked in the figure mentioned above, is the knee point where the PV string voltage drops. Also, the low current under the high voltage region is due to the shaded PV cell sinking power. The I-V characteristics of the PV panel under shading situation picturizes normal PV panel

I-V characteristics with reverse biases PV cell I-V characteristics. 4 different points are marked in Figure 3-26. They are injected with a small signal to measure the impedance of the PV panel under 1 PV cell-shaded condition. The resistive load used for impedance measurement will be depended on the voltage and current of the marked points in the figure, as discussed above.

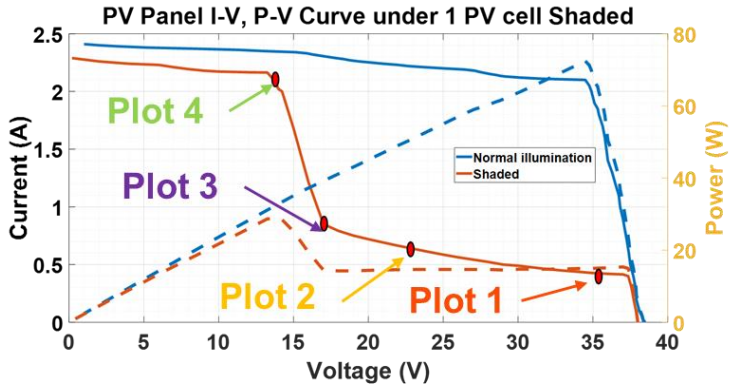

Figure 3-26 PV panel I-V characteristics with 300 W/m^2 illumination comparison under normal condition and hot spot fault condition

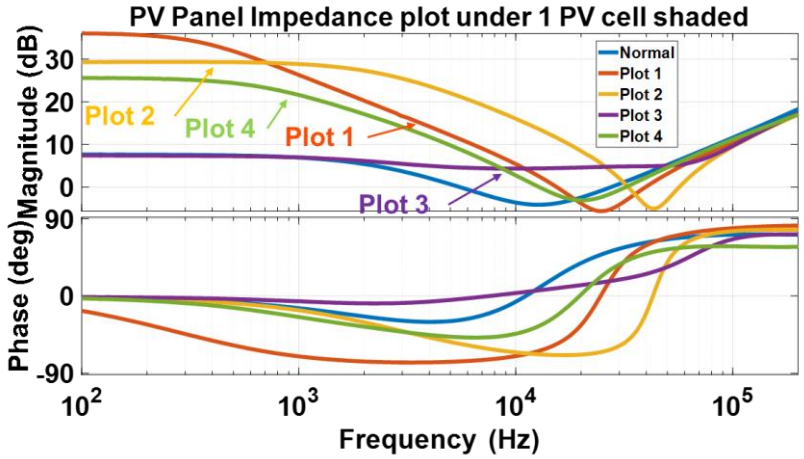

Figure 3-27 PV panel offline AC impedance comparison under hot spot fault condition with O. Ps as shown in Figure 3-26

Figure 3-27 compares the impedance for the shaded PV cell in the illuminated PV panel with different power points. Comparing the impedance plot of plot 1 with the expected condition, under shading, the magnitude and decrease in the phase of impedance increase can be seen in low frequency. The increase in phase can be seen in the mid-frequency region due to the increase of

parallel resistance and parallel capacitance and the change in the operating point of the shaded PV cell. Similarly, plots 2 and 4 resemble shading conditions with increased parallel resistance and capacitance of shaded PV cells. Plot 3, the knee point, fails to mimic the results of the shading condition. All four shaded PV cell plots of impedance show impedance under the different slopes of the P-V curve, as seen in Figure 3-26. Plot 4, near the 2nd knee point of the P-V curve, is considered as 1 PV cell-shaded fault impedance for further fault comparison.

3.4.4.2 Multiple PV Cell Hot Spot:

Figure 3-28 shows the comparison of I-V and P-V characteristics of illuminated PV panels with 1 PV cell-shaded and 2 PV cells (similar PV string) shaded. The location of multiple shaded PV cells of the same string shows identical I-V and P-V characteristics; thus, the location of a shaded PV cell in the same string doesn't alter the results. The O.P. taken into consideration is near the MPP, as seen in the P-V characteristics. Plot 3 shows a decrease in current due to an increase in sinking power by both the shaded PV cells. Also, as 2 PV cells are shaded, the reverse bias voltage will increase, so higher negative voltage results in low voltage at a higher current for plot 3. Comparing plot two and plot 3, under a high voltage region due to 2 PV cells shaded current is lower for plot 3.

Figure 3-29 shows the comparative results of the impedance of illuminated PV panels with shaded PV cells. Under 2 PV cells shaded (plot 3), the impedance magnitude for the low-frequency region is slightly higher than 1 PV cell shaded (plot 2). Under the mid-frequency region where the impact of parallel capacitance can be seen, the phase of impedance for plot 3 is lower than plot two due to an increase in parallel resistance of 2 PV cells shaded than 1 PV cell shaded. Also, the resonating point frequency shifts due to increased capacitance and change in the O.P. of the shaded

PV cells. Thus, with a higher number of PV cells shaded in the PV panel, the PV cell sinking power increases, and so the current magnitude also decreases the magnitude of the impedance of the PV panel increases with an increase in parallel resistance and parallel capacitance and change in the O.P.

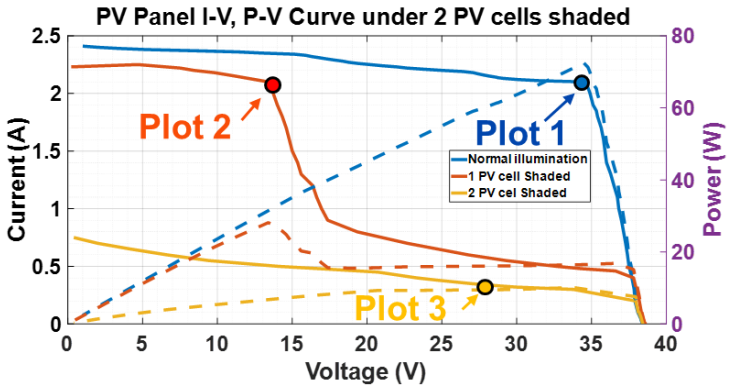

Figure 3-28 PV panel I-V characteristics with 300 W/m^2 illumination comparison under normal condition, single and multiple hot spot fault condition

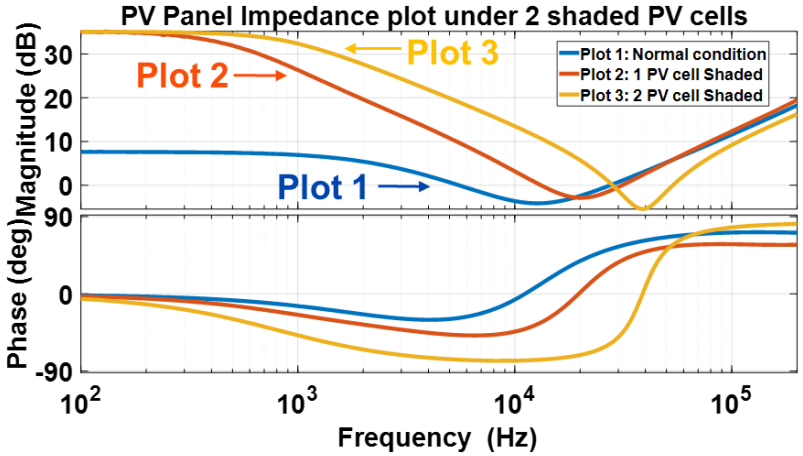

Figure 3-29 PV panel offline AC impedance comparison under multiple hot spot fault condition with O. Ps as shown in Figure 3-28Figure 3-26

3.4.4.3 % Shading PV Cell:

A PV cell enters a reverse bias condition due to shading. Also, the % shading or covering of the PV cell alters the reverse bias voltage of the shaded PV cell. Figure 3-30 shows the I-V and P-V characteristics comparison of an illuminated PV panel with 1 PV cell shaded under 100%

shading, 75% shading, and 50% shading conditions. As the figure mentioned above shows, plot 4 (75% shading) is near plot 2 (100% shading) as the reverse bias voltage is higher in higher % shading. Under high voltage conditions, the current is higher in lower % shading conditions due to less sinking power by shaded PV cells. From plot 3, plot 4, and plot two, the reverse voltage increment can be deduced, and the decrease in current can be noticed. Thus, with the increase in % of the shading of 1 PV cell, the reverse-biased voltage of the shaded PV cell increases, and the effective PV current decreases due to the sink power increase by the shaded PV cell.

The impedance plot for the points mentioned above on the I-V and P-V characteristics is shown in Figure 3-31. The impedance magnitude for lower % shading is less than for higher % shading. Also, plot three and plot 4 show a discrepancy with a phase of impedance compared with plot 2; a probable reason would be the test point considered for plot three, and plot four might not be the exact MPP and be at the left side of MPP. So lower % shading conditions show a decrease in a phase when compared to plot 2.

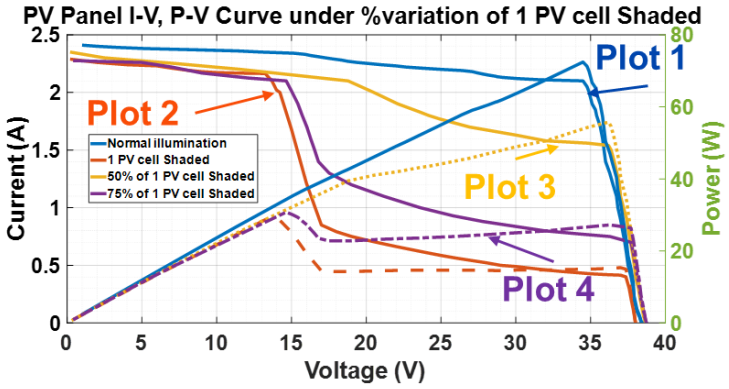

Figure 3-30 PV panel I-V characteristics with 300 W/m^2 illumination comparison under normal condition and % shaded in a hot spot fault condition

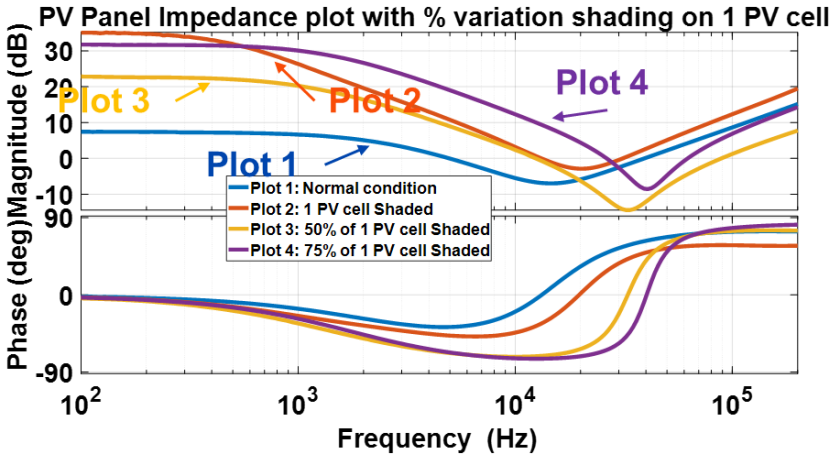

Figure 3-31 PV panel offline AC impedance comparison under % shaded in hot spot fault condition with O. Ps as shown in Figure 3-30

3.4.5 PV Panel Impedance Measurement under Short Circuit Fault:

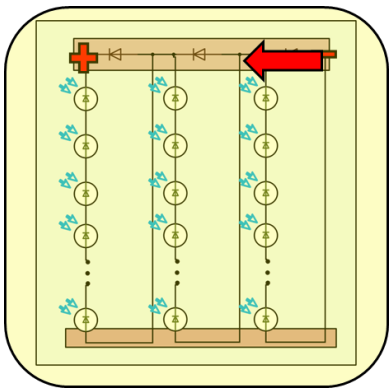

Figure 3-32 Illuminated PV panel diagram under short circuit fault

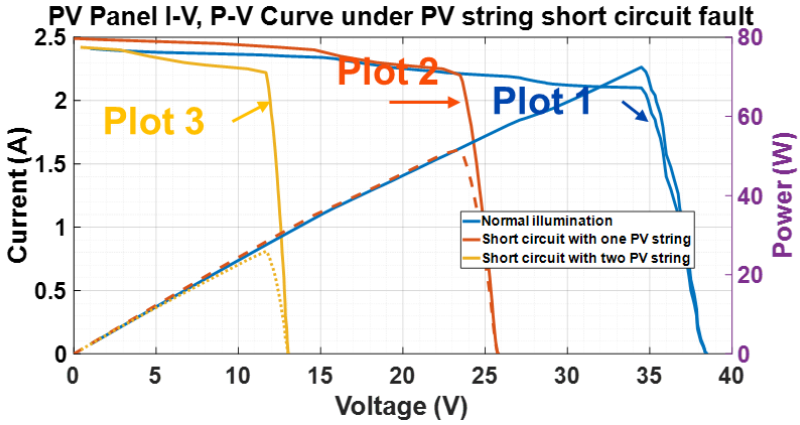

Figure 3-33 PV panel I-V characteristics with 300 W/m^2 illumination comparison under normal condition, single and double short circuit fault

Under harsh weather conditions, the bypass diode in the junction box of the PV panel can be a short circuit which leads to a short circuit fault, as shown in Figure 3-32. Due to a short circuit

fault, the total power from the PV panel decreases as the voltage across the PV panel decreases. Figure 3-33 compares I-V and P-V characteristics of illuminated PV panels with different short circuit conditions. With 1 PV string short circuit, 1/3rd of the power decreases, and with 2 PV string short-circuited, 2/3rd of the power from the PV panel decreases, as can be noticed in the figure mentioned above. As discussed above, the impedance can be measured by injecting a small signal to the MPP of the conditions. Figure 3-34 compares the impedance plot for the short circuit with normal conditions. Due to short circuit conditions, the impedance of the PV panel should decrease as the PV string impedance decreases to zero. The impedance magnitude at a resonating point is lower for plot 3 than for plot 2 and lower for plot 1; the decrease in series resistance due to short circuit conditions will lower the impedance magnitude under resonating point. The impedance magnitude under low-frequency region decreases under short circuit conditions, as seen in the figure below. The impedance under low frequency is governed by parallel and series resistance. Thus the parallel resistance also decreases with short circuit conditions. The PV cells in a PV panel are connected in series, and the impedance of the PV cell with short circuit conditions, the PV cells short-circuited will not contribute in voltage, and the current and effective impedance will be negligible.

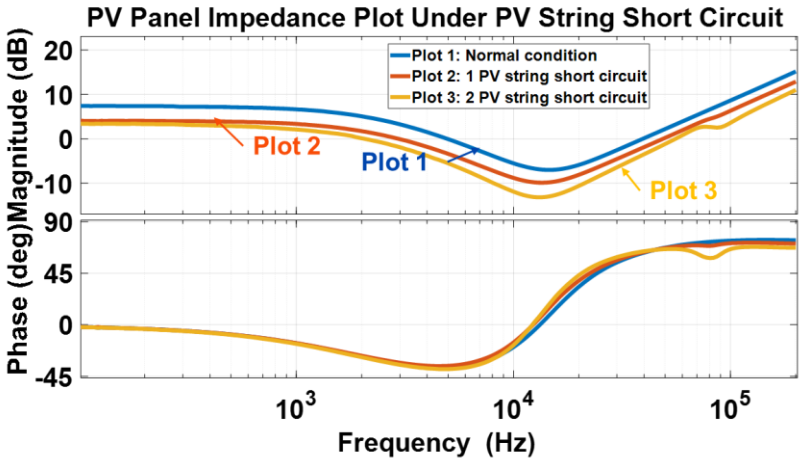

Figure 3-34 PV panel offline AC impedance comparison under short circuit fault with O. Ps as shown in Figure 3-33

3.4.6 Junction Box Fault:

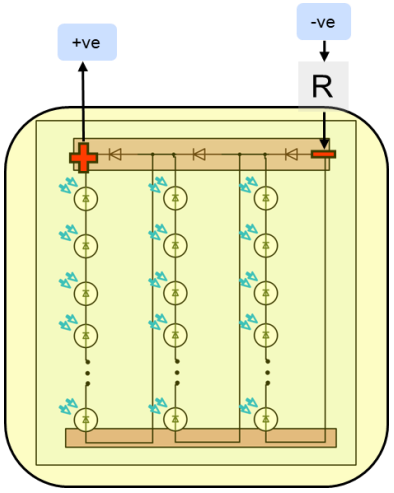

Figure 3-35 Illuminated PV panel diagram under junction box fault

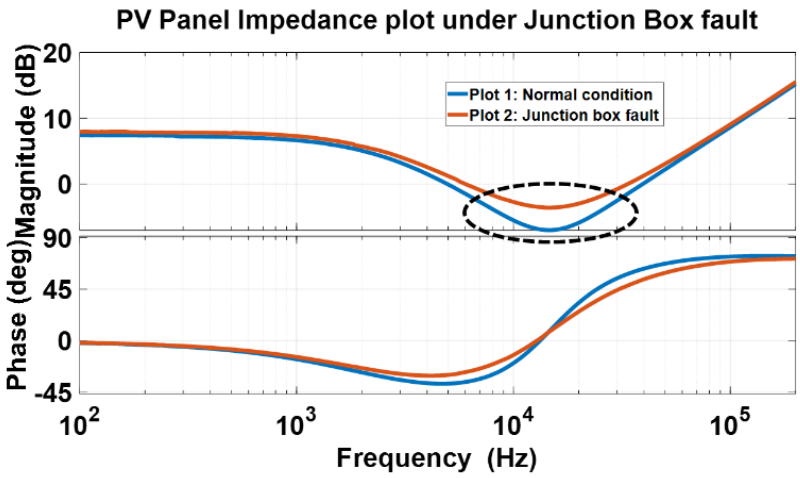

Figure 3-36 PV panel offline AC impedance comparison under junction box fault and normal condition

The junction box (JB) of a PV panel with 60 PV cells has three bypass diodes at the terminal to connect PV cells. PV cells divided equally share a bypass diode, i.e., 20 PV cells connect across one bypass diode. Over time contact resistance R(ohms) due to joints and soldering in the junction box increases, thus causing Junction Box fault. A series resistance of 0.22 Ω was added to the PV panel to evaluate the junction box fault, as shown in Figure 3-35. Due to the small magnitude of series resistance and lower current from the PV panel, the I-V and P-V characteristics of the Junction box fault are like normal conditions. Figure 3-36 shows the impedance plot of the Junction box; under the low-frequency region, a slight increase in impedance magnitude can be noticed. A junction box fault can be detected with an increase in magnitude under the mid-frequency region. At the resonating point, the magnitude of the impedance is equal to the magnitude of series

resistance; thus, an increase in the magnitude of impedance can be noticed due to the junction box fated.

3.5 Conclusion

Under the continuous operation of the PV panel for a long time, it might go into multiple fault conditions where it can witness one or more than one faults. Figure 3-37 compares I-V and P-V characteristics of multiple fault scenarios with illuminated PV panels. The fault scenarios considered are hot spot fault, where one PV cell was shaded, the bypass diode was open-circuited; junction box fault, where a series resistance was added to the PV panel; and short circuit fault, where 1 PV string was short-circuited. Comparing hot spot faults with short circuit faults to normal conditions, we notice the voltage has decreased due to short circuit faults. At the mid-region of voltage, the current is lower than normal due to shading fault influence. Also, the total current has been decreased due to the shaded PV cell sinking power.

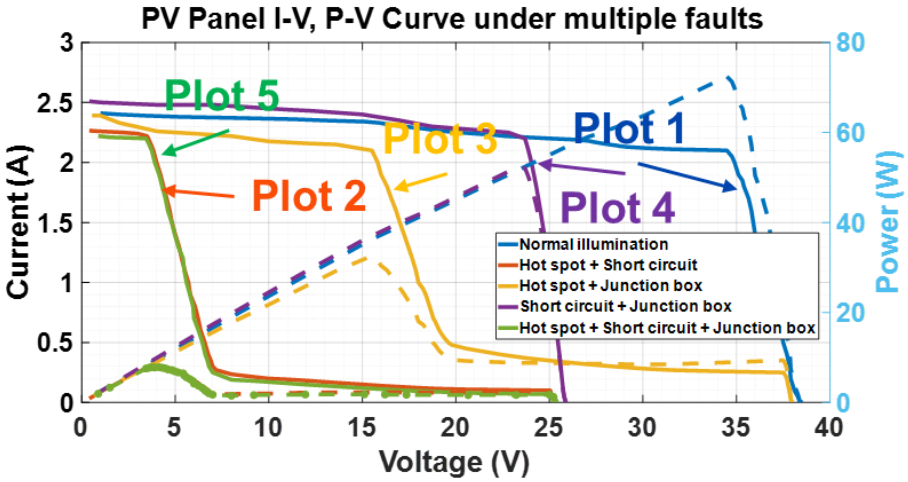

Figure 3-37 PV panel I-V characteristics with 300 W/m^2 illumination comparison under normal condition and multiple fault condition

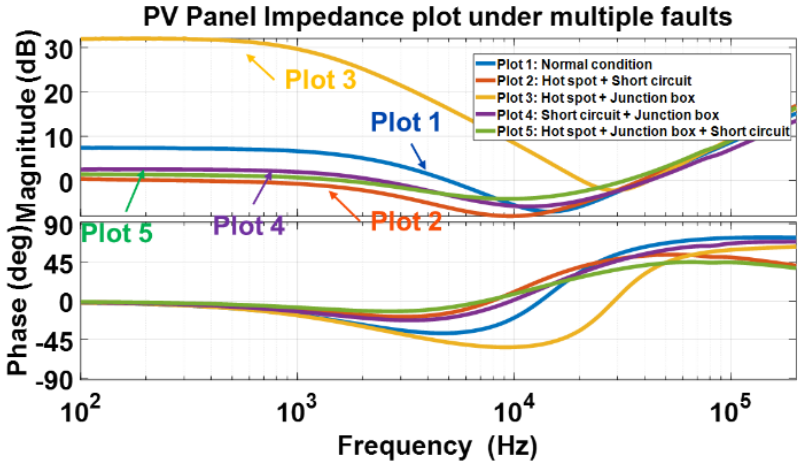

Figure 3-38 PV panel offline AC impedance comparison under multiple fault condition with O. Ps as shown in Figure 3-30

Comparing hot spot and Junction box fault to normal conditions, the influence of hot spot can be seen as with regards to the junction box, the I-V characteristics will not change and so hot spot fault influences more in this case. With short circuit fault and junction box fault, the influence of sort circuit fault dominates and can be a witness in the figure too. Under all three-fault conditions, the I-V and P-V characteristics are like hot spot and short circuit fault conditions. Not much change is witnessed due to series resistance in the faulty junction box being the small and lower magnitude of PV current. The PV rack setup was used to measure the impedance of the PV panel under multiple fault conditions. Figure 3-38 compares impedance plots for multiple fault conditions. Comparing plot 2 with plot 1, the effect of short circuit fault is dominant as the operating point is not entirely MPP; thus, impedance magnitude is lower than normal conditions. Also, the phase is increased due to a short circuit fault. Comparing plot 3 with plot 1, the hot spot fault indicators dominate under low-frequency and mid-frequency regions; under the mid-

frequency region, the phase is decreased because of parallel capacitance. Also, due to additional series resistance, the impedance magnitude is higher than the normal condition at the resonating point. Thus, individual effects of hot spots and junction boxes can be noticed. Plot 4 is when the short circuit and junction box fault are noticed in the PV panel, the impedance plot resembles the short circuit fault, and at the mid-frequency region, because of the junction box fault, the magnitude of the impedance is higher than the plot 1. Under all three-fault conditions, the impedance plot is like hot spot and short circuit fault conditions, adding on the impedance magnitude at the resonating point due to junction box fault.

Chapter 4 DC /DC Converter for Power Optimizer Application

4.1 Introduction

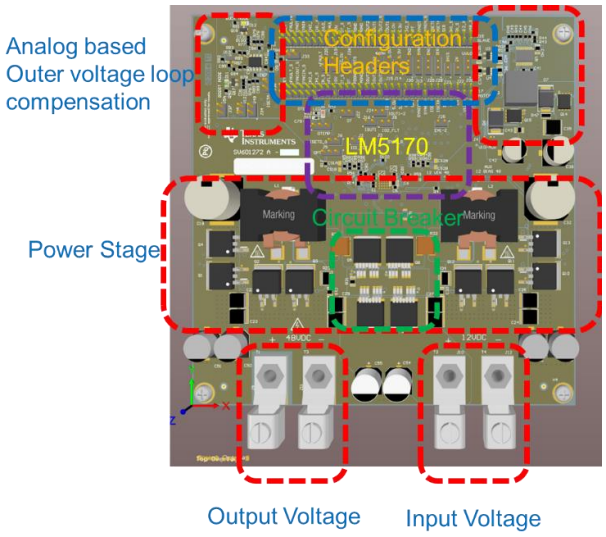

Figure 4-1. P.O peripheral details

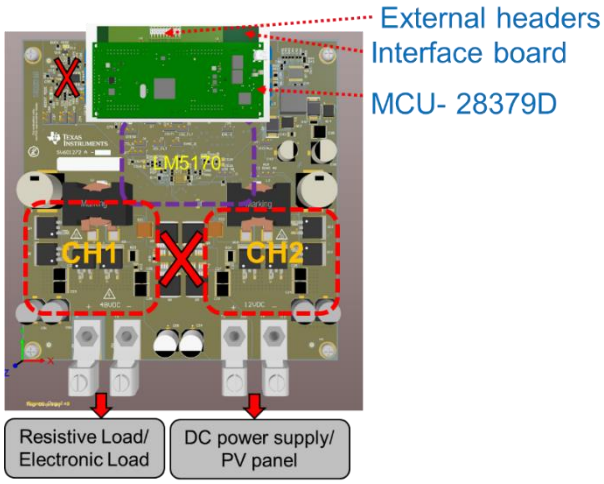

Figure 4-2. P.O hardware test block diagram with interface board and MCU

PV industry today sink PV power to the grid to extract maximum power from PV panel. A power optimizer is a dc-dc converter connected to a PV panel on one end and dc-ac inverter on the other end to transfer power from the PV panel and deliver it to the dc-ac inverter, which can be connected to the grid. LM5170EVM is a dc-dc converter used as a boost converter in this project. Figure 4-1 shows LM5170EVM has a power stage with a buck-boost converter with two-channel configurations. The power stage was controlled with average current mode control via the LM5170 chip; thus, the inductor current was always controlled based either on an internal compensator or via external control signal through a microcontroller unit (MCU). The LM5170EVM has an analog

base outer voltage loop to provide a fixed 50.5 V at the output end with input voltage from 12 V to 48 V in boost operation. The configuration header pins shown in the figure above are used to configure LM5170EVM and provide a control command for the required PV panel-based operation. An external interface board can be connected to LM5170EVM, as shown in Figure 4-2. To utilize LM5170EVM as a boost converter for solar applications, the circuit breaker of the evaluation board (EVM) was disabled, outer voltage loop compensation was turned off, and channel 1 of EVM was turned ON to operate EVM in single-channel mode.

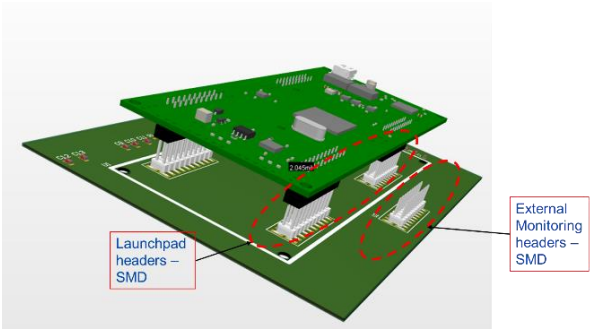

Figure 4-3. Interface board 3D view

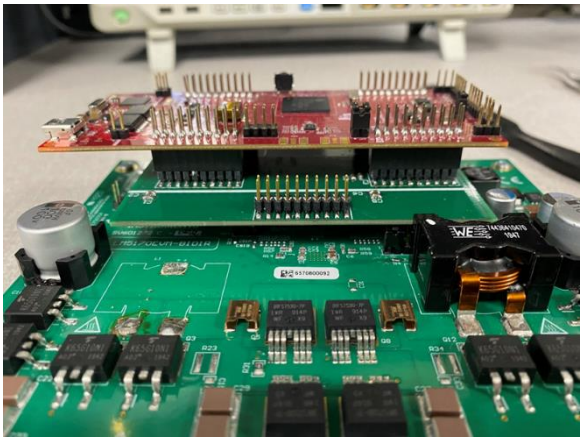

Figure 4-4. MCU and interface board attached with P. O

The control signal to EVM and sensor data from EVM are transferred to MCU via the interface board. As shown in Figure 4-2, the input and output end source and load can be connected. LM5170EVM can be configured for the application via a configuration header pin, where an interface board can be connected to LM5170EVM, and then an MCU can be connected on the top. Figure 4-3 shows the 3D view of the top side of the interface board with a launchpad – 28379D MCU. A few extra header pins are kept for monitoring EVM data on the oscilloscope. The complete assembly of the interface board with MCU and EVM is shown in Figure 4-4.

4.2 DC /DC Converter Performance:

4.2.1 DC /DC Converter Analysis using Simulation

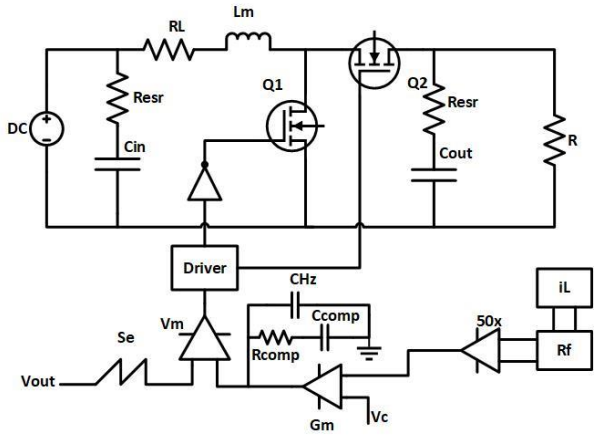

Figure 4-5. P.O circuit diagram with the average current control mode

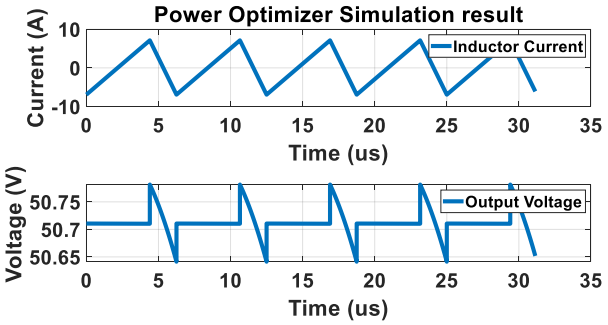

Figure 4-6. P.O simulation result

The power optimizer inductor current was controlled through average current mode control; the circuit diagram of a boost converter with average current mode control is shown in Figure 4-5. The average current mode control simplifies compensation by eliminating the right half plane zero in the boost operating point and by maintaining a constant loop gain regardless of the operating voltage and load level. Based on the EVM datasheet, the value of the passive component was determined, and a simulation was performed to understand the operation of P.O. via SIMPLIS software, as shown in Figure 4-6. Simulation results show the inductor's ripple current was 20 A, and the operation was in discontinuous mode (DCM), either the inductor current was below 0 A. Such operation is not recommended for solar applications.

4.2.2 DC/ DC Converter Hardware Performance prior updating

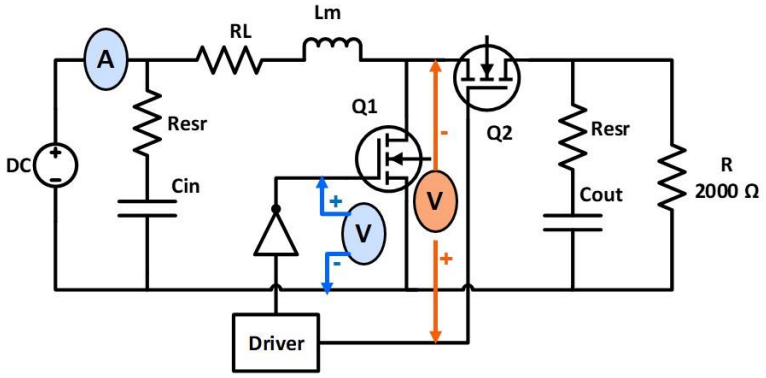

Figure 4-7. P.O circuit diagram under light load

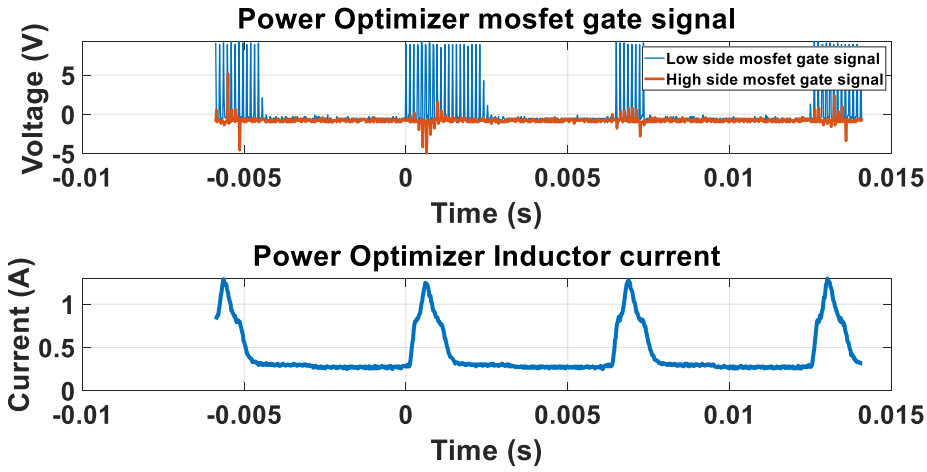

Figure 4-8. P.O under light load with MOSFET gate signal and inductor current waveform

P.O. was also evaluated with hardware where the input voltage was supplied using the power supply, output was connected to the electronic load, internal analog voltage loop compensator was used to operate the system in boost mode with 50.5 V output voltage. Under light load conditions, as shown in Figure 4-7, where the output was connected to 2000 Ω load, the P.O waveform is shown in Figure 4-8. Due to current 0A, either in DCM mode, the P.O diode emulation shuts off the MOSFET high side gate signal, as shown in the figure mentioned above, and thus, the operation was discontinuous. The LM5170EVM has LM51702 – Q1 average current control IC, and each

channel in the IC has a real-time current zero crossing detector to monitor instantaneous current sensed voltage (V_{CS}). When V_{CS} is detected to cross zero, the LM5170-Q1 turns off the gate drive of the synchronous rectifier to prevent a negative current. In this way, the negative current is prevented, and the light load efficiency is improved. Thus, the inbuild diode emulation controls the IC gate signal under light load conditions, and to inject a small signal in the PV panel under light load, the DC/ DC converter was updated.

4.3 Updating DC /DC Converter

4.3.1 Continuous Vs. Discontinuous Conduction Mode

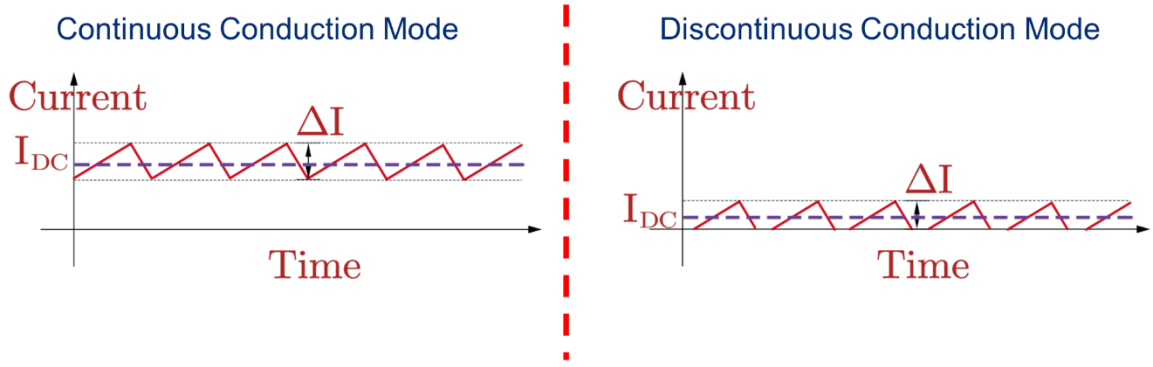

Figure 4-9. Continuous current mode vs. discontinuous current mode

To operate the PV panel under light load conditions, the system needs to operate in continuous current mode (CCM); the difference in the operation is shown in Figure 4-9. Under CCM, the ripple current should be low, so to operate the system in CCM, a few parameters need to be changed P.O.

$$\frac{V_{in}}{\acute{D}^2 R} > \frac{DT_s V_{in}}{2L} \quad for\ CCM \tag{4-1}$$

Based upon equation (4-1), the dependent variable for CCM operation is the input voltage, duty, switching frequency, and inductance.

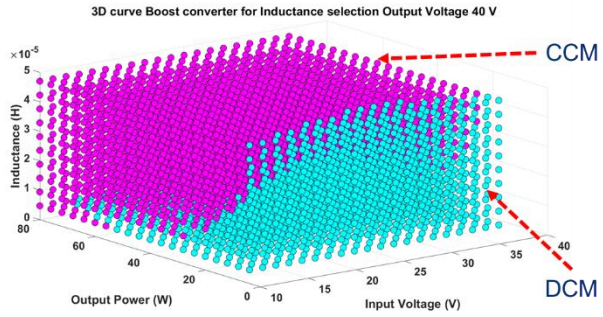

Figure 4-10. The 3D curve for CCM and DCM mode comparison with the varying input voltage, output power, and inductance

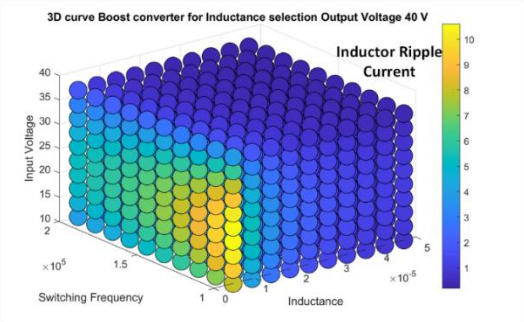

Figure 4-11. P.O inductor ripple current under varying inductance, switching frequency, and input voltage

A Simulink-based 3D curve is shown in Figure 4-10 to analyze CCM and DCM operation and select inductance value for CCM operation.

$$Inductor\ ripple\ current = \frac{V_{in}D}{2F_{sw}L} \quad (4\text{-}2)$$

A Simulink-based 3D curve is shown in Figure 4-11 to understand ripple current fluctuation based on the inductance, switching frequency, and input voltage. Also, the inductor ripple was analytically computed, as shown in equation (4-2), to select the inductance value and change the switching frequency. For solar applications, the inductor ripple should be low than 1 A to obtain an average DC at the output of the PV panel.

4.3.1.1 Updating Inductance and Switching Frequency of DC /DC Converter

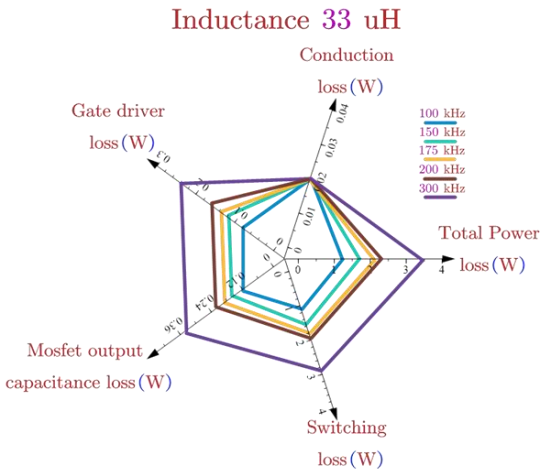

Figure 4-12. MOSFET loss comparison

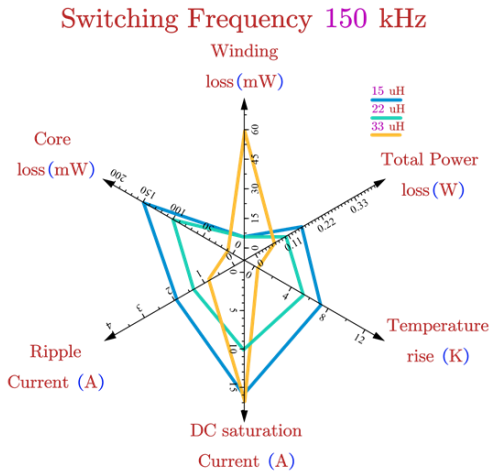

Figure 4-13. Inductor loss comparison

Based on the analysis, as shown above, the inductance and switching frequency of MOSFET should be increased for CCM operation.

Table 4-1 LM5710EVM parameters to calculate MOSFET losses

Parameter	Value	Units
Output Voltage	40	V
Inductor	33	µH
Output load	22	Ω
Input Voltage	35	V
T_{ON}	44	nS
T_{OFF}	85	nS
R_{DS-ON}	3.8	mΩ
∂	1/30	
Gate charge	81	nC
Gate voltage	10	V
Q_{coss}	33	nC

$$Switching\ loss = \frac{V_{in}}{2}\left(I_o - \frac{\Delta i_{LPP}}{2}\right) f_{sw} t_{on} + \frac{V_{in}}{2}\left(I_o + \frac{\Delta i_{LPP}}{2}\right) f_{sw} t_{off} \quad (4\text{-}3)$$

$$Conduction\ loss = R_{dson}(1+\partial) I_o^2 \left(1 + \frac{1}{12}\left(\frac{\Delta i_{LPP}}{I_o}\right)\right) \quad (4\text{-}4)$$

$$Gate\ driver\ loss = Q_g V_{drive} f_{sw} \quad (4\text{-}5)$$

$$Mosfet\ output\ capacitance\ loss = Q_{coss} V_{in} f_{sw} \quad (4\text{-}6)$$

MOSFET loss comparison using analytical equations (4-3)-(4-6) and parameters in Table 4-1 is shown in Figure 4-12, where the MOSFET switching frequency was increased. As noticed, with an increase in frequency, MOSFET loss increases as switching losses increase, and thus switching frequency of 150 kHz was selected for the project. Figure 4-13 shows a comparison of inductor loss with an increase in the value of inductance. Based on the above analysis and inductor loss, 33 µH inductance was selected for the project. Inductor losses are computed using REDEXPERT

WÜRTH ELEKTRONIK software. P.O inductance and switching frequency are increased, so system stability needs to be also calculated, and the inner current loop needs to be updated.

4.3.2 Closed Loop Control for DC/DC Converter using Average Current Mode Control

Figure 4-14 shows the block diagram for computing the inner current loop gain, where G_{id} is plant transfer as shown in equation (4-7) with duty as input and inductor current as output, R_f is sensor gain, G_m is transconductance gain, G_{comp} is compensator gain, and V_m is modulator gain.

$$G_{id} = \frac{2V}{\acute{D}^2 R}\left(\frac{1 + s\frac{RC}{2}}{1 + s\frac{L}{\acute{D}^2 R} + s^2\frac{LC}{\acute{D}^2}}\right) \quad (4\text{-}7)$$

$$T_i = G_{id} * G_{comp} * R_f * V_m * G_m \quad (4\text{-}8)$$

Equation (4-8) was used to compute the loop gain of the system and design a compensator with higher bandwidth and higher phase margin for stable operation.

$$G_{comp} = \frac{1}{C_{comp}}\left(\frac{1 + sR_{comp}C_{comp}}{s\left(1 + sR_{comp}C_{HZ}\right)}\right) \quad (4\text{-}9)$$

Considering the RC network for the inner current loop and designing the compensator as shown in equation (4-9), the updated RC network was R_{comp} 25 kΩ, C_{comp} 1 nF, C_{HZ} 100 pF.

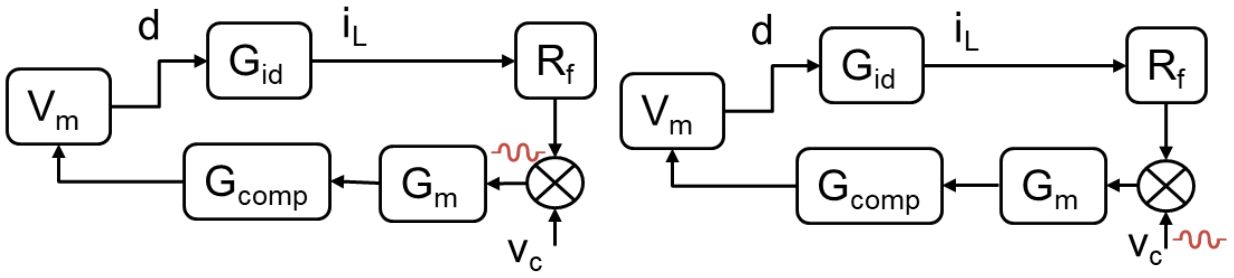

Figure 4-14. Uncompensated inner current loop gain block diagram

Figure 4-15. Inner current control to output gain block diagram

$$G_{ci} = \frac{1}{R_f}\left(\frac{T_i}{1+T_i}\right) \quad (4\text{-}10)$$

With an updated RC network, inner current control to output gain can be computed using the block diagram shown in Figure 4-15 and with equations (4-10). Similarly, inner current control to output gain can be measured in simulation using SIMPLIS software, as shown in Figure 4-16. The analytical result was compared with simulation-based results and shown in Figure 4-17. As shown in the figure mentioned above, the closed-loop gain is constant under the low to mid-frequency region. Thus, the inner current loop is stable for the operation.

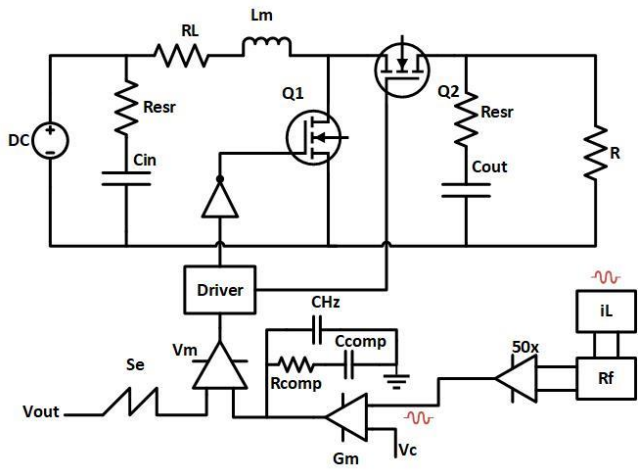

Figure 4-16. Circuit diagram of P.O with inner current control to output control

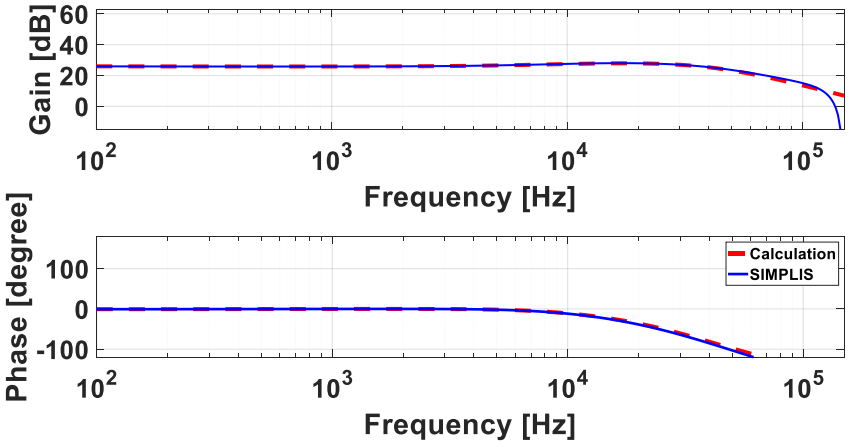

Figure 4-17. Inner current control to output gain bode plot

4.4 Microcontroller and Power Optimizer Performance

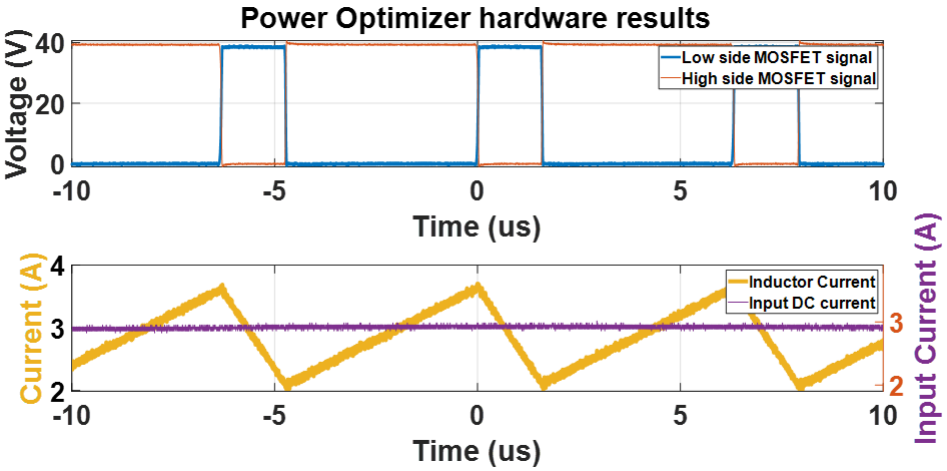

Figure 4-18 DC-DC converter hardware result at 24 W

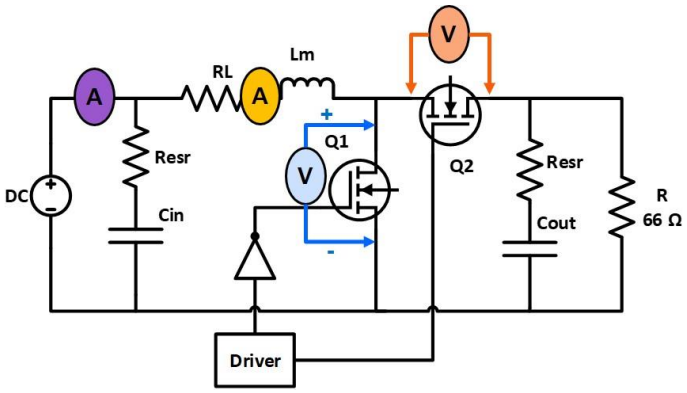

Figure 4-19 DC-DC converter equivalent circuit at 24 W

The DC-DC converter, as shown in Figure 4-19, was used as a boost converter with an output voltage of 40 V. The rack setup designed in the CPES laboratory has a PV panel sourcing power of 75 W under 300 W/m^2 illuminations with maximum power point at a PV voltage of 35 V and PV current of 2.2 A; thus, the P.O. was tested up to 75 W power. The P.O. was evaluated with hardware where the input voltage was supplied using the power supply. The output was connected to the electronic load under the resistive load of 66 W. The P.O. has an input voltage of 10 V, the DC of the P.O. can be measured using the current probe, and the AC into the inductor can be measured using the Rogowski coil. The voltage across MOSFETs can be measured using a differential voltage probe. The waveform of input current, inductor current, and MOSFET pulses for 24 W output power can be seen in Figure 4-18. With a duty cycle of 75%, the low-side MOSFET switch's turn-on time was longer than the high-side switch's turn-on time, as seen in the figure mentioned above.

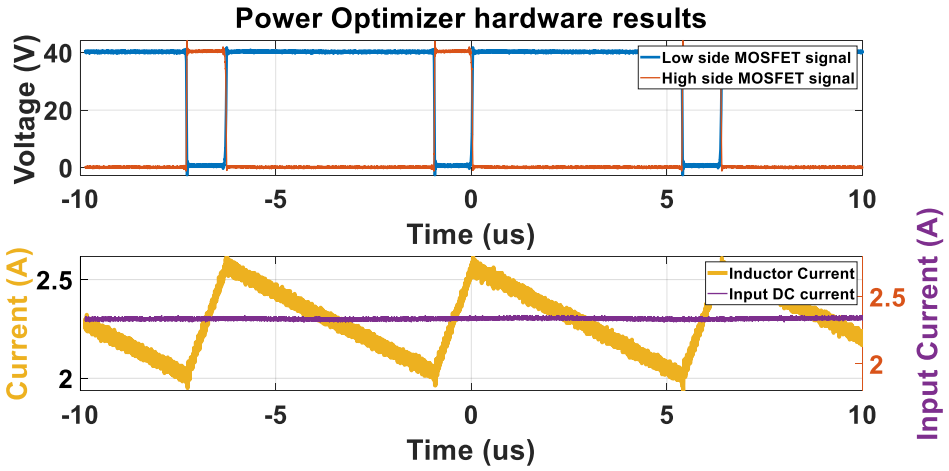

Figure 4-20 DC-DC converter hardware result at 75 W

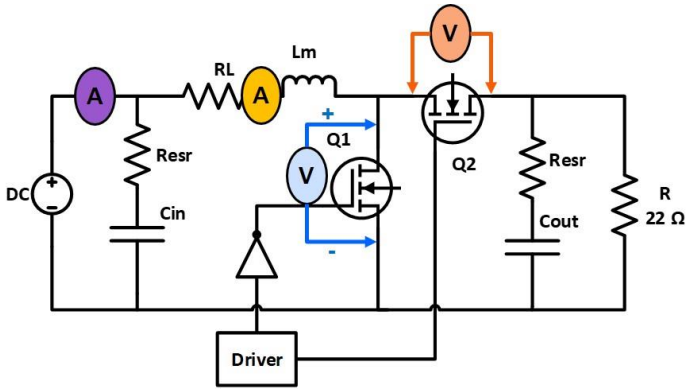

Figure 4-21 DC-DC converter equivalent circuit at 75 W

The P.O. was evaluated with 75 W output power with an input voltage of 35 V and output voltage of 40 V; the output was connected to the electronic load under the resistive load of 22 Ω, as shown in Figure 4-21. The waveform of input current, inductor current, and MOSFET pulses for 75 W output power can be seen in Figure 4-20. With a duty cycle of 12.5%, the high-side MOSFET switch's turn-on time was longer than the low-side switch's turn-on time, as seen in the figure mentioned above.

4.5 Conclusion

TI- based DC/ DC boost converter LM5170EVM was configured using header pins, and inductor current was regulated to control the converter in boost operation. TI launchpad F28379-D was interfaced with a boost converter to operate the evaluation board under normal operation and generate a control signal for regulating the inductor current. DC/ DC converter was tested under light load using evaluation boards' analog outer voltage loop prior to update. Under light load operation, diode emulation mode was noticed, and DC/ DC converter updated for CCM was further studied. DC/ DC boost converter inductance was updated from 4.7 µH to 33 µH, and MOSFET switching frequency was increased from 100 kHz to 160 kHz to operate the boost converter from 24 W to 300 W. With updating inductance and switching frequency, MOSFET losses, and inductance losses were studied for boost converter application. The current sensor was updated for better resolution under the low current application. The average current control mode was simulated, and the inner current compensation circuit was updated for inner current close loop operation. The converter was tested under 24 W and 75 W with inner current close loop operation. The DC/ DC converter evaluation board was further used as a power optimizer to measure PV panel impedance.

Chapter 5 Photovoltaics Panel Impedance Measurement using Online Technique

5.1 Introduction

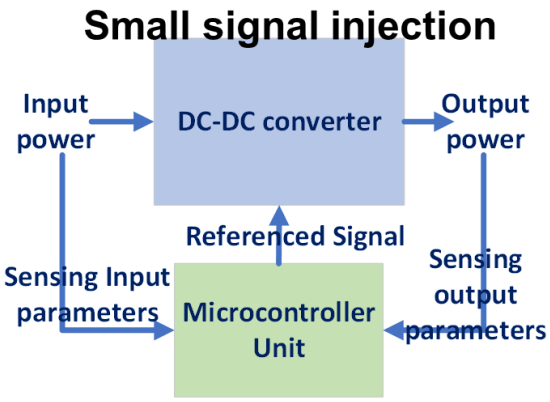

Figure 5-1 Small signal injection via reference signal in DC-DC converter

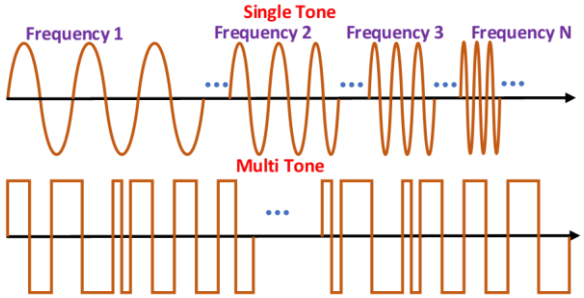

Figure 5-2 Types of small signal injection

The P.O. has an average current mode control LM5170 TI-based chip to control the average inductor current. MCU provides the control signal to the P.O. via a referenced signal; the MCU also senses voltage and current at the input and output node, as shown in Figure 5-1. The small signal was injected into the converter using the reference signal. The small signal perturbs above the reference signal and thus be injected in P.O., the perturbation in the reference signal will generate perturbation in the inductor current via the RC network. The small signal injected in the P.O. can be either single-tone in nature or multi-tone, as shown in Figure 5-2.

Table 5-1 Single-tone Vs. Multi-tone

Small Signal Injection		
	Single-tone	**Multi-tone**
Injection	Single frequency + multiple pulses	Single frequency + 1 pulse
Response computation	One frequency at a time	Complete band of frequency
Time taken	Long	Short
Memory	Short	Long
Method	**SFRA**	**PBRS**
Software	**C based code**	**Simulink code generator**
Implementation	**Simple**	**Complex**
High frequency response	**Difficult to implement**	**Can be implemented**
Online impedance measurement	**Implemented**	**To be implemented in future**

Table 5-1 shows a comparison of single-tone vs. multi-tone small signal injection. A single-tone small signal injects a single frequency with multiple pulses at a time; thus, the response computation duration is long. As the response is computed in real-time thus, the data memory required will be small. Single-tone small signal injection was performed using a TI-based software response frequency analyzer (SFRA). The SFRA is a C-based code and is simple to implement. Multi-tone small signal injects a single frequency with a single pulse at a time; thus, the response computation duration is small. The system records the data in real time, and after the injection, the response is computed; thus, the data memory required will be long. Multi-tone small signals can be generated using a pseudo-binary random signal (PBRS) generator. The multi-tone small signal injection can be performed using a Simulink-based embedded code generator. The code generator has a few bugs while deploying code in MCU and is thus currently difficult to implement. Single-tone online impedance measurement was implemented to detect faults in the PV panel.

5.2 Software-based Frequency Response Analyzer

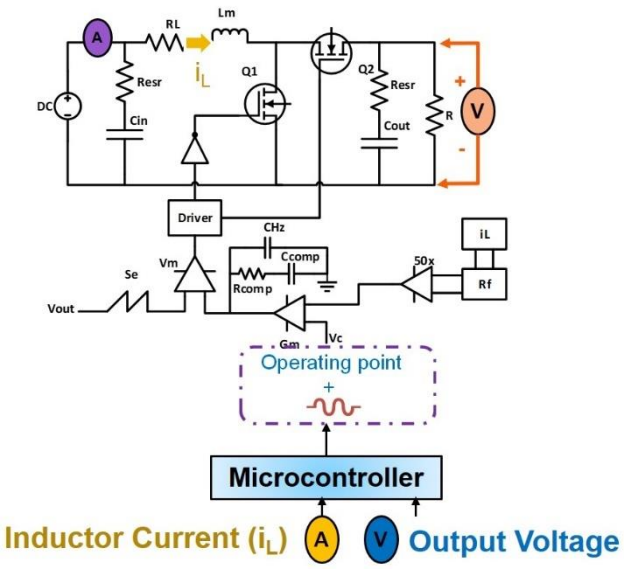

Figure 5-3 Small signal injection via SFRA

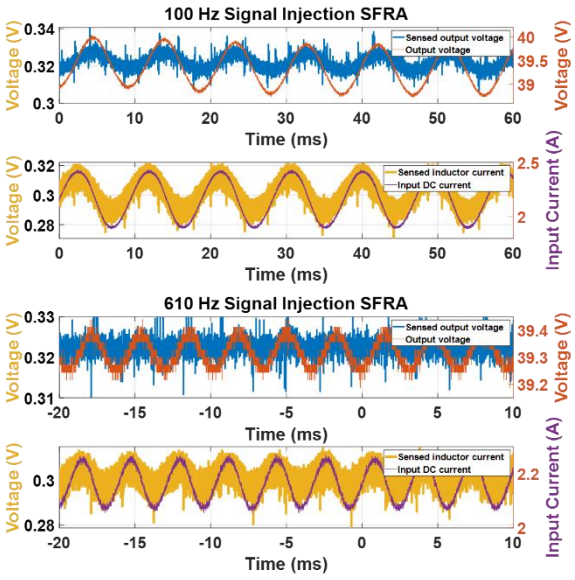

Figure 5-4 Small signal injection in input current and output voltage of DC-DC converter

The MCU utilizes code composure studio (CCS) IDE to monitor and deploy software in MCU. The CCS can, in real time, monitor the variable stored in the SRAM of the MCU; thus, real-time ADC value monitoring helps debug errors. The SFRA generates a single-tone small signal which perturbs the reference signal. Figure 5-3 demonstrates the use of SFRA with P.O. The P.O has an input supply of 35 V and was connected to a resistive load of 22 Ω; the MCU sets the referenced signal to generate an output voltage of 40 V. Using SFRA, single tone small signal was injected into the P.O via reference signal and the MCU stores the ADC value for few perturbations in an array and CCS can be utilized to real-time monitor the array. Figure 5-4 shows the waveform for 100 Hz and 610 Hz small signal of input current and output voltage via oscilloscope and sensed inductor current and sensed output voltage via CCS. The inner current loop bandwidth needs to be

higher than the small signal frequency injections to avoid attenuation in the small signal. Also, the ADC encounters noise and attenuation in sensing high-frequency responses due to low pass filter and parasitic. Thus, the figure mentioned above shows that the small signal nature of sensed output voltage and inductor current is dominant at a low frequency of 100 Hz, but at 610 Hz, the signal attenuates.

5.2.1 PWM vs. DAC:

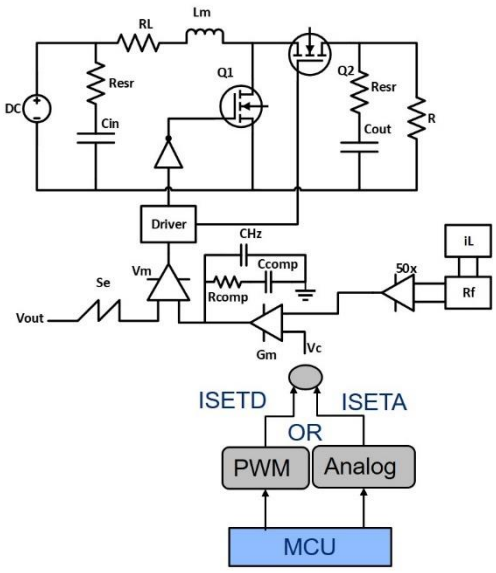

Figure 5-5 Boost converter with a control signal from either PWM or Analog pin

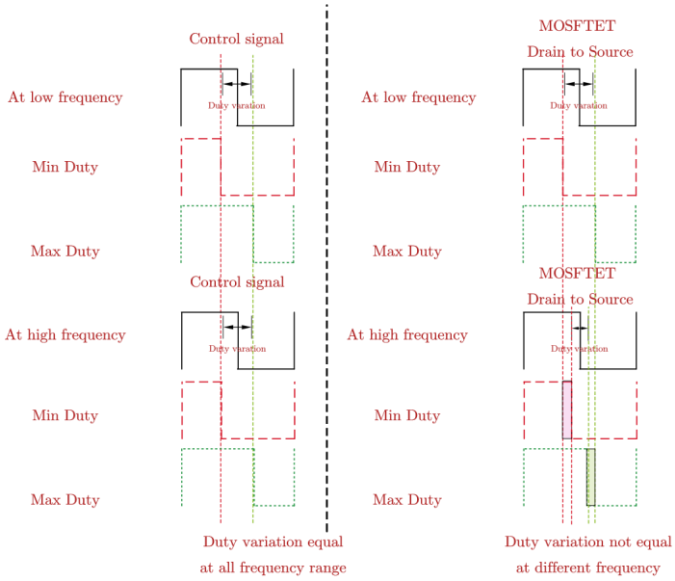

Figure 5-6 Control signal duty comparison with MOSFET drain to source during small signal injection

The small signal generated by SFRA is added to the operating point either in the digital signal via ISETD or analog signal ISETA. The current regulation level to DC/ DC converter is controlled by an analog signal applied at the ISETA pin or digital PWM signal at the ISETD pin, as shown in Figure 5-5. The internal ISETD decoder converts the PWM duty ratio at the ISETD

pin to an analog voltage at the ISETA pin. Monitoring the operation using digital control with ISETD pin, under low-frequency operation, the perturbation in PWM at control signal had similar duty witness in MOSFET drain to source. Under high frequency with the small signal injection in the ISETD pin, the perturbation injected in the MOSFET drain to the source didn't match the duty injected in ISETD due to the decoder's presence, as explained in Figure 5-6. Thus, for small signal injection, ISETA was used, and the control signal from MCU to LM5170EVM was generated using DAC.

5.2.2 Small Signal Perturbation in the Control System

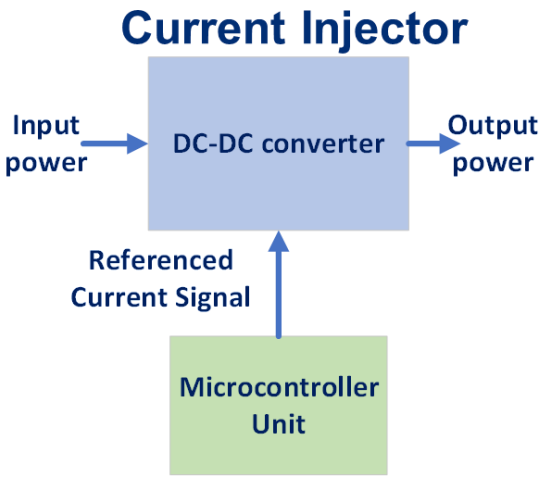

Figure 5-7 Current injector block diagram

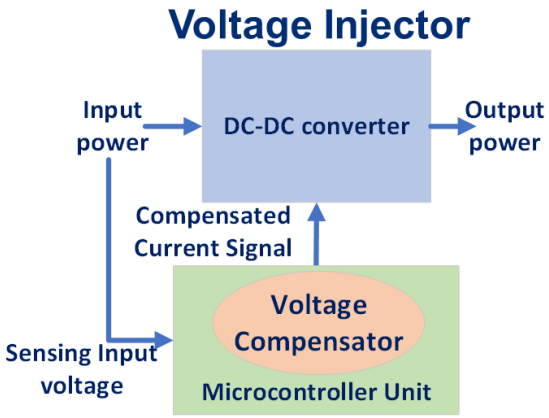

Figure 5-8 Voltage injector block diagram

The P.O. has different control methods, either inner current loop control to set the inductor current or input voltage with inner current loop control to set the input voltage of the PV panel. For only inner current loop control, the MCU injects perturbation in a referenced current signal called the current injector, as shown in Figure 5-7. For input voltage and inner current loop control, the MCU senses the input voltage and utilizes the voltage compensator, and a compensated current

signal was given to the P.O. The small signal perturbs the reference voltage before the voltage compensator called the voltage injector, as shown in Figure 5-8.

Table 5-2 Comparison between voltage injector and current injector

	Voltage Injector	Current Injector
Additional compensator	Required	Not required
Perturbation at high impedance region	Can be possible	Not possible
System stability	Depends upon bandwidth of inner current loop	Stable with 2 kHz bandwidth
Online Impedance measurement	**Difficult to implement**	**Implemented**

For a PV panel, if an operating point move left the maximum power point (MPP), the operating point enters a high impedance region. Here, with a change in voltage, the difference in current is significantly small as compared to the right of MPP. A voltage injector can be used to inject perturbation in a high-impedance region; for the current injector, the amplitude of a small signal will be high, and the system might become unstable. Also, the bandwidth of the voltage compensator in the voltage injector is dependent on the bandwidth of the inner current loop; thus, the voltage injector stability is difficult to implement. Table 5-2 compares a voltage injector with a current injector; for this project, the results below are based on the current injector.

5.3 Power Optimizer with Photovoltaic Panel

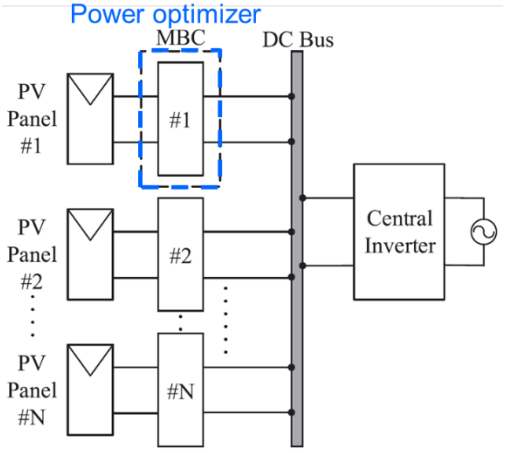

Figure 5-9 PV panel power extraction using power optimizer

LM5170 EVM		
	TI	**SETO-PV**
Application	Battery charging	Power Optimizer
Operation	CCM+DCM	CCM
Inductance	4.7 µH	33 µH
Switching frequency	100 kHz	> 100 kHz
System stability	-	Improvised
Current sensor	1 mΩ	5 mΩ

Table 5-3 Updated DC-DC converter for power optimizer use

A power optimizer (P.O) is a dc-dc converter connected to a PV panel on one end and a dc-ac inverter on the other to transfer power from the PV panel and deliver it to the dc-ac inverter, which can be connected to the grid as shown in Figure 5-9. LM5170EVM is a Texas Instrument (TI) based dc-dc converter used as a boost converter in this project, as shown in Figure 5-10. The TI-based DC-DC converter was used for battery charging applications. Certain modifications are needed to operate the converter as a P.O. Table 5-3 shows the changes required necessary to run the converter as a P.O. The TI-based converter is capable of operating in discontinuous current mode (DCM) under low power and continuous current mode (CCM) with sufficient inductor current and thus the inductance used in the converter is relatively low. For the P.O application, the converter inductor current must always be positive and CCM operation; hence the inductance and switching frequency are increased. With a change in inductance, the converter bandwidth and stability change; thus, the converter's RC network was modified to obtain system stability. The

inductor current sensor resistor used by TI can measure current till 50 A but has a low resolution for low current (< 2 A), so the resistor was increased for better resolution at low current.

5.3.1 Small Signal Injection into PV Panel using P.O.

Figure 5-10 LM5170EVM DC/ DC converter with MCU launchpad – 28379D

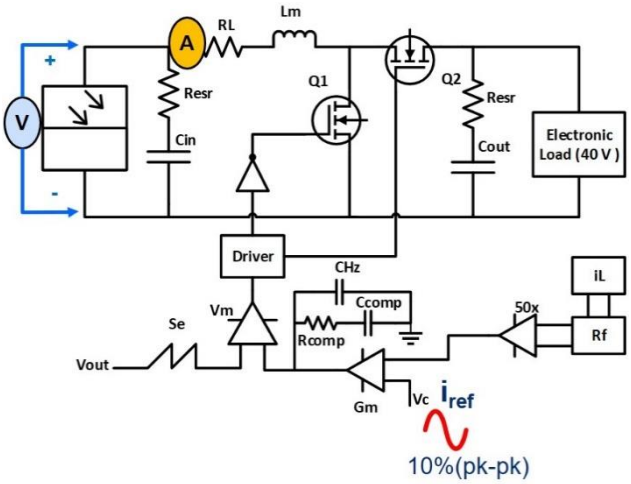

Figure 5-11 Small signal injection into PV panel using boost converter and SFRA via MCU

The updated DC-DC converter, as shown above, can be used as a P.O. to extract power from the PV panel under CCM operation. The control signal to the evaluation board (EVM) and sensor data from EVM are transferred to the launchpad – 28379D microcontroller unit (MCU) via the interface board. Figure 5-10, the input and output end source and load can be connected. LM5170EVM can be configured for the application via a configuration header pin, where an interface board can be connected to LM5170EVM, and then an MCU can be connected on the top. A few extra header pins are kept for monitoring EVM data on the oscilloscope. Figure 5-11 is a boost converter with input voltage from the PV panel up to 40 V at open circuit condition and output connected to electronic load under a constant voltage of 40 V.

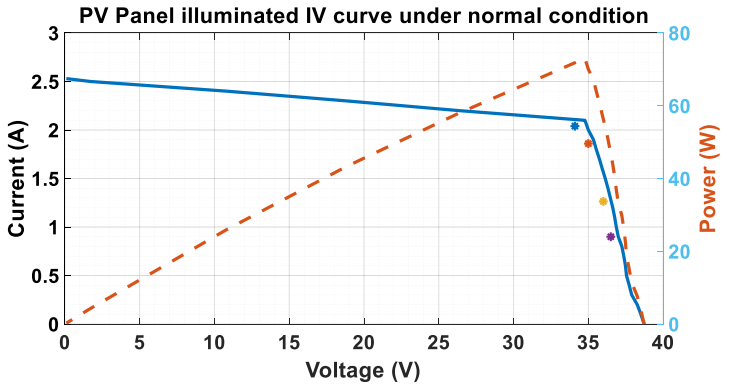

Figure 5-12 PV panel I-V and P-V characteristics under normal conditions

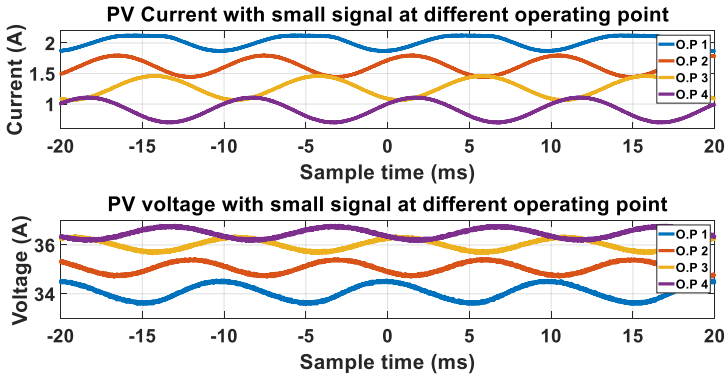

Figure 5-13 PV panel voltage and current waveform at the different operating points with small signal

Figure 5-12 shows the I-V and P-V characteristics of a monocrystalline PV panel with 60 PV cells and 300 W/m^2 of irradiance on the PV panel using a PV panel rack setup. The PV panel was connected to the input of P.O., and the output end of P.O. was connected to an electronic load. MCU provides the reference current to set the operating point on the PV panel. Using the current injector, an SFRA-based single-tone small signal was injected at four different operating points, as seen in the above figure. Figure 5-13 shows the perturbation on four different operating points with a current and voltage waveform via an oscilloscope. The operating point marked with orange, yellow, and purple fall on the right of MPP; thus, the sinusoidal nature of small signal perturbation

can be seen. The operating point marked in blue is located to the left of MPP; hence, a plateau-type nature is visible in the current waveform for the above-mentioned figure. Thus, the operating points selected to measure the impedance of the PV panel will be at the low-impedance region on either right side of the MPP.

5.3.2 Input Impedance Measurement using P.O.

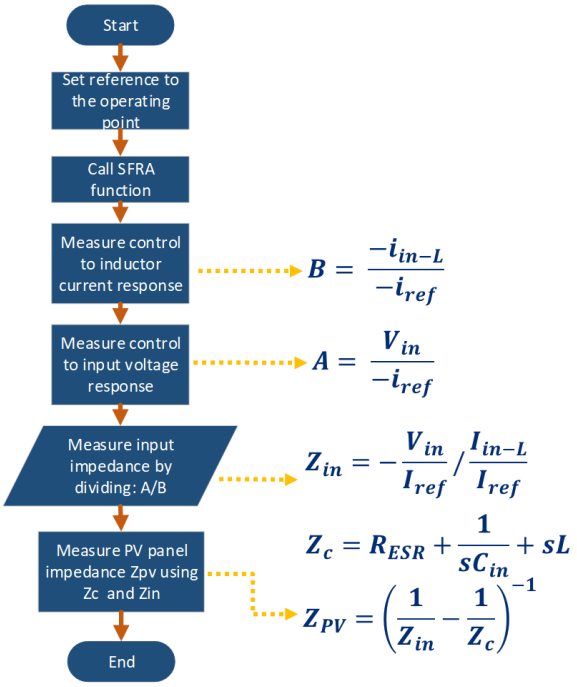

Figure 5-14 Flowchart to compute PV panel impedance using SFRA

Parameters	SFRA
Computation time	1.5 minutes
Data points	100
Frequency band	10 Hz – 1 kHz
Signal amplitude	10 %

Table 5-4 SFRA parameters

Online PV panel impedance was calculated with the help of a flow chart, as shown in Figure 5-14. Initially, the PV panel was set at an operating point using P.O. A reference signal was given to P.O. using MCU, with an operating point as set SFRA function was called. The SFRA needs a few parameters to be set before perturbation, as shown in Table 5-4. The small signal amplitude was set at 10% of the reference signal, the number of data points selected was 100, and

the frequency band for a response via SFRA was from 10 Hz to 22 kHz. MCU generates the reference signal with small signal perturbation, as shown in Figure 5-11, to measure control to inductor response ($V_{c\text{-}iL}$). Once the response for $V_{c\text{-}iL}$ was recorded, the data was stored in excel, and later SFRA measured, control to input voltage response ($V_{c\text{-}vin}$). The response for $V_{c\text{-}vin}$ was recorded and stored in excel. The input impedance for the system was measured using MATLAB, $V_{c\text{-}vin,}$ and $V_{c\text{-}iL}$. By dividing the two responses, the input impedance can be computed.

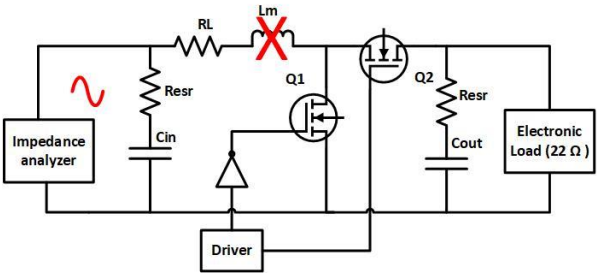

Figure 5-15 Offline input capacitance impedance measurement

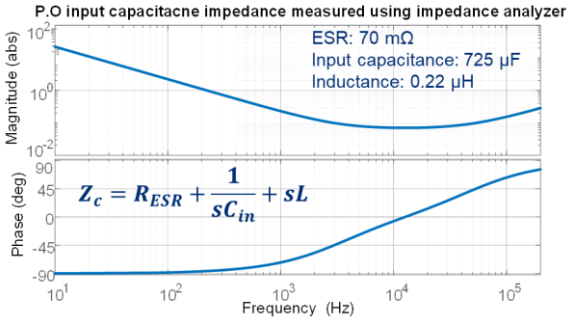

Figure 5-16 Input capacitance AC impedance measured using a network analyzer

To compute PV panel impedance using an online impedance measurement algorithm, the impedance of input capacitance was measured as shown in Figure 5-15. The offline impedance measurement was performed with an impedance analyzer, and the inductor of P.O. was opened; thus, the impedance measured will only be for input capacitance, ESR of capacitance with parasitic. Input capacitance was computed with MATLAB, and curve fitting was used to calculate input capacitance impedance in the s-domain. The frequency response of the input capacitance is shown in Figure 5-16. PV panel impedance was measured with input capacitance response, and the input impedance was measured using SFRA. Thus, with the help of the flowchart, the PV panel impedance can be measured online using dc-dc converter and SFRA.

5.3.3 Temperature Effect on PV Rack Setup

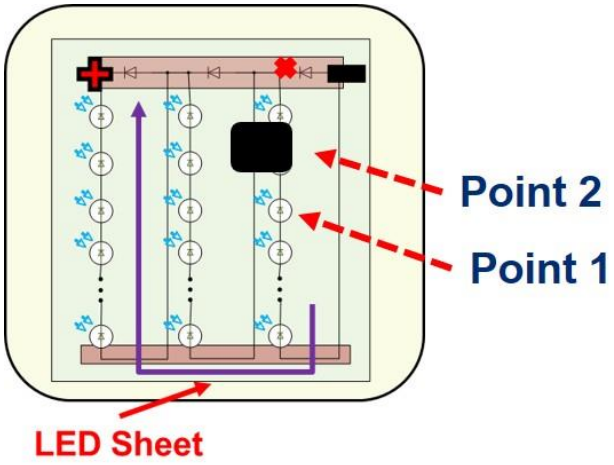

Figure 5-17 Illuminated PV panel with one PV cell shaded

The PV panel rack setup was illuminated using LED sheets, and the irradiance measured was 300 W/m^2. Due to space restrictions, the LED sheets tend to increase the temperature on the PV panel. A temperature variation test was performed to understand the temperature variation of PV panels under 300 W/m^2 illumination. Figure 5-17 shows the PV panel with one cell shaded completely; the temperature was monitored at two different locations, as shown in the figure mentioned above. Initially, both the points in the figure mentioned above are unshaded and kept at normal conditions; the Fluke temperature probe measures the temperature. Later, point No. 2 of the figure mentioned above was shaded, and the temperature of both points was measured.

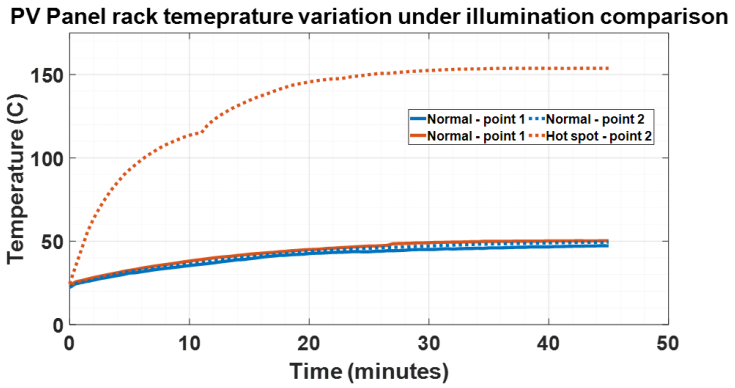

Figure 5-18 Temperature variation of PV cells under normal and hot spot conditions

The experiment was conducted for 45 minutes, and the PV panel was sourcing power to the electronic load at MPP. The temperature settles at 50 °C for normal conditions and at 175 °C for the PV cell shaded. Thus, to perform online impedance measurement, the PV panel temperature needs to be also monitored. The temperature should be stable to avoid a change in the operating point. Figure 5-18 shows the temperature variation for the experiments with two different locations.

5.4 Indoor Online Impedance Measurement of PV Panel

5.4.1 PV Panel Impedance Measurement under Normal Condition

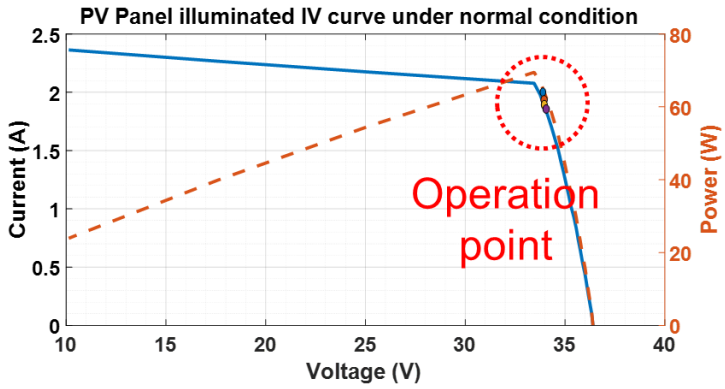

Figure 5-19 PV panel I-V and P-V characteristics under the normal condition with small signal injection operating point

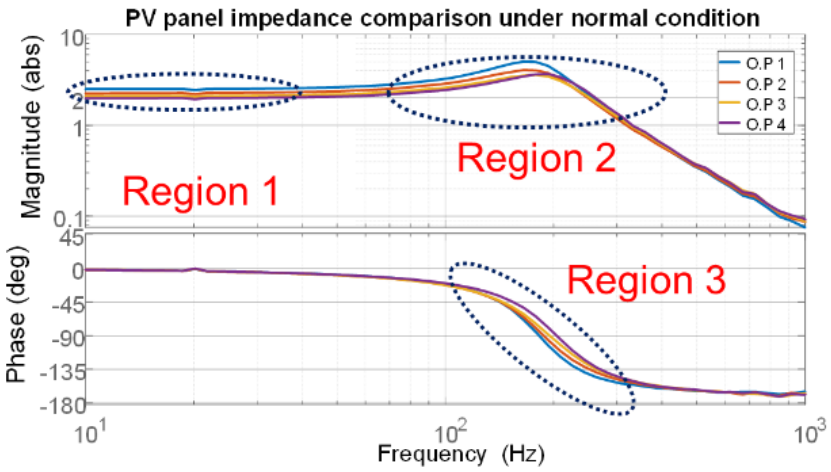

Figure 5-20 PV panel impedance at the different operating points under normal conditions

The PV panel impedance under the normal condition at 300 W/m^2 illuminations was measured using an online impedance measurement algorithm. The operating points for impedance measurement are marked in the PV panel I-V and P-V characteristics, as shown in Figure 5-19. The operating points are on the right side of MPP either under the low impedance region; the impedance measured and computed is shown in Figure 5-20. The impedance magnitude marked in region 1 decreases as the operating point shifts further right to the MPP; also, the impedance phase marked under region 3 shows the increase of phase; thus, the parallel capacitance decreases as the operating point shifts to the right of MPP. The impedance magnitude marked under region 2 shows the effect of bandwidth for the voltage and current sensor filter. The online impedance measured under normal conditions will be the benchmark for comparing the impedance under fault conditions.

5.4.2 PV Panel Impedance Measurement under Fault Conditions

5.4.2.1 PV Panel under Hot Spot Vs. Short Circuit Condition

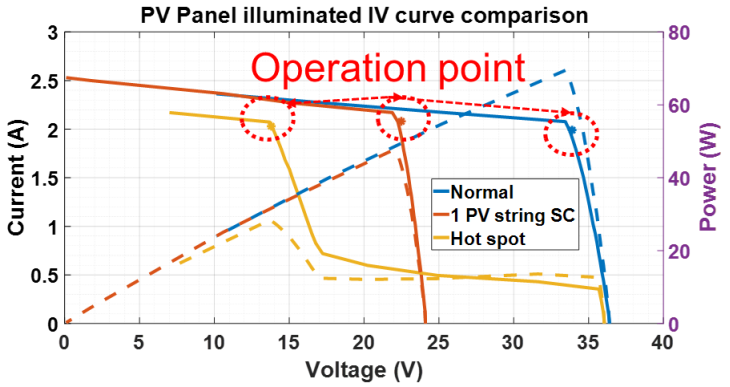

Figure 5-21 PV panel I-V and P-V characteristics comparison under normal and fault conditions

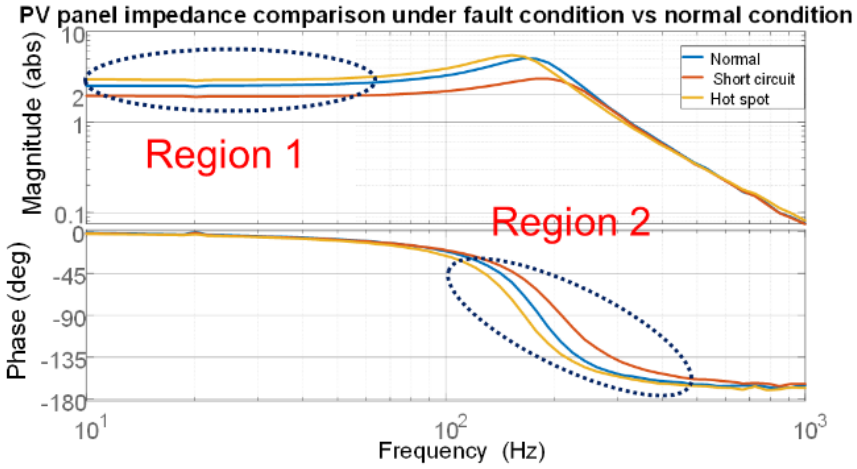

Figure 5-22 PV panel impedance comparison under normal and fault conditions

The PV panel impedance under a fault condition was measured and compared using online impedance measurement. The PV panel impedance was measured for short circuit fault with 1 PV string short circuit from 3 PV strings. Later the PV panel impedance was measured for the Hot spot fault where one of the PV cells was shaded, and the bypass diode of the shaded PV cell string was removed. Figure 5-21 shows the different operating points for different fault conditions in the

PV panel. PV panel impedance under fault conditions can be compared with a normal condition, as shown in Figure 5-22. Under region 1 of the image, as mentioned above, for hot spot fault, the fault indicator shows the increase in the impedance magnitude under the low-frequency region as the parallel resistance increases due to the reverse characteristics of the PV cell. Under region 2, for the hot spot fault, the impedance phase decreases in mid frequency region as the parallel capacitance increases for the shaded PV cell. Comparing PV panel impedance for short circuit fault with a normal condition, the impedance magnitude in region 1 shows a decrease in the impedance magnitude due to a decrease in the total number of PV cells; thus, the cumulative series and parallel resistance of PV panel decreases under short circuit conditions. Under region 2, the PV panel impedance phase increases due to a decrease in the capacitance of the PV panel under short circuit conditions. Thus, online impedance measurement can identify the PV panel hot spot and short circuit fault using online impedance measurement.

5.4.2.2 PV Panel under Junction Box Fault

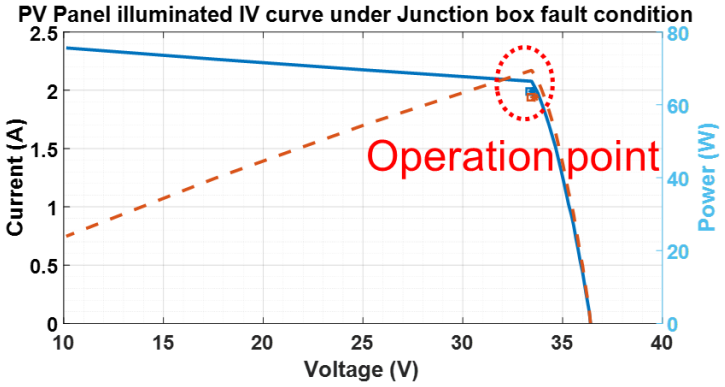

Figure 5-23 PV panel I-V and P-V characteristics under junction box fault

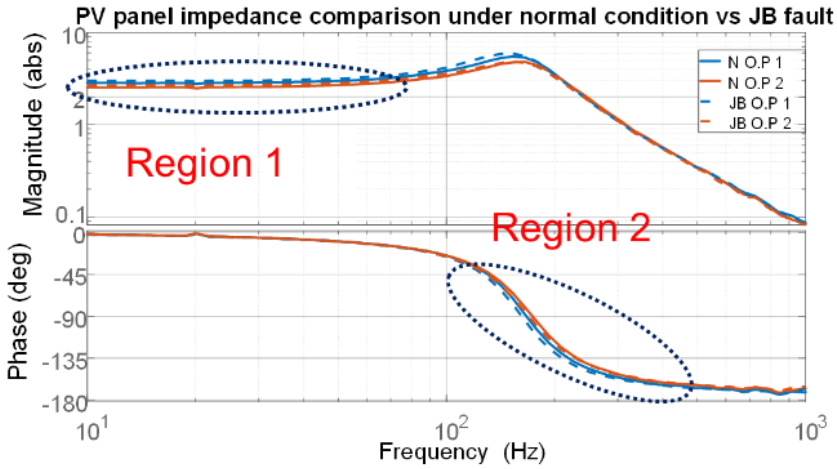

Figure 5-24 PV panel impedance comparison under normal and junction box fault condition

For implementing junction box fault detection in the PV panel, a series resistance of 0.1 Ω was added to the junction box. Online impedance measurement was performed at the operating points shown in Figure 5-23. The PV panel impedance was measured and computed, as shown in Figure 5-24. As mentioned above, the impedance for the image shows an increase in the impedance magnitude for the operating points by 0.14 Ω under region 1. Also, the impedance phase under region 2 shows an increase in phase. Thus, online impedance can detect a PV panel's junction box faults.

5.4.3 Capacitance Fault Detection using Online Impedance Measurement:

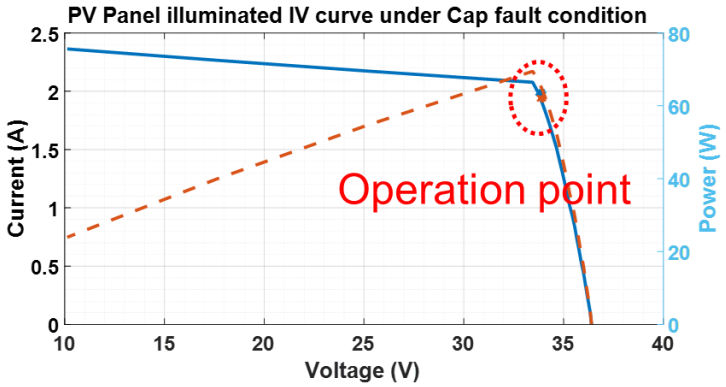

Figure 5-25 PV panel I-V and P-V characteristics under capacitance fault

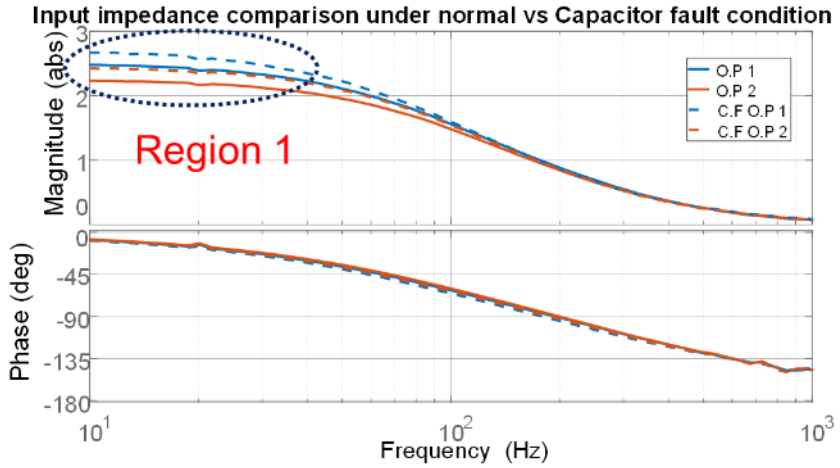

Figure 5-26 Input impedance comparison under normal and capacitance fault conditions

Over time, the DC-DC converter used as a power optimizer can degrade in performance. The input capacitance over the life degrades, causing the capacitance to decrease and the electrostatic resistance (ESR) to increase. A capacitor reaches its end of life (EOF) with a 20% decrease in capacitance and twice an increase in ESR. Online impedance measurement can be used to measure the input impedance of the PV panel. It can identify the impedance change at the same operating point over the period to detect the capacitor fault in the power optimizer. To conduct a capacitor fault detection test, one capacitor from 4 capacitors of a dc-dc converter at input was removed; thus, the capacitance decreased by 25%, and an online impedance measurement was performed. Figure 5-25 shows the operating point for injecting a small signal to the input end of the dc-dc converter. The input impedance of the dc-dc converter was measured and computed as shown in Figure 5-26. The input impedance marked in region 1 shows an increase in the impedance magnitude compared to the normal condition; as the input capacitance decreases, the impedance increases. Also, a consistent increase in the impedance magnitude can be seen with impedance for

both operating points marked in blue and orange. Thus, with a decrease in input capacitance, the online impedance can identify a consistent change in the impedance magnitude at the same operating point and indicate the capacitor fault of the power optimizer.

5.4.4 Relative Standard Deviation Test for Online Impedance Measurement:

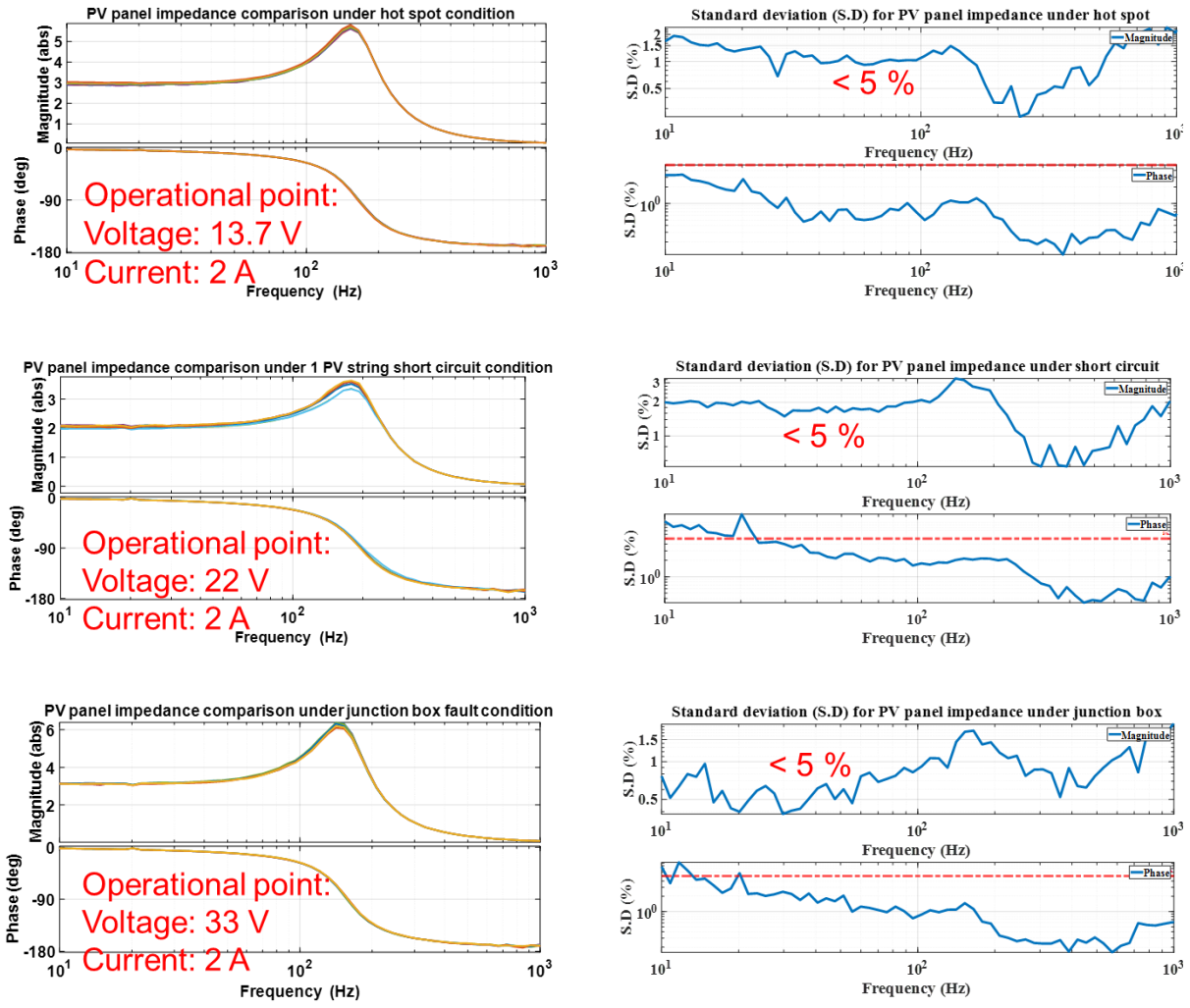

Figure 5-27 R.S.D for computing effectiveness of online impedance measurement

The online impedance measurement was tested for relative standard deviation to understand the variation under PV panel faults at measured frequency points. Each PV fault

impedance was measured 10 times at 100 different frequency points. The equation below calculated the relative standard deviation (R.S.D) of PV panel impedance under faulty conditions. Where x_i is the mean of the sample data, x is the sample data, and N is the number of data points. The PV panel impedance test for standard deviation under fault conditions like hot spot fault, short circuit fault, and junction box fault is shown in Figure 5-27. The relative standard deviation was calculated with the below-mentioned equation and is shown in the figure above. For each PV panel fault, at all the measured frequency points, the R.S.D is less than 5 %.

$$R.S.D = \frac{\sqrt{\sum((x_i - x)^2)/N}}{x} \quad (5\text{-}1)$$

5.5 Outdoor Online Impedance Measurement of PV Panel:

5.5.1 PV Panel Online Impedance Measurement under Normal Condition

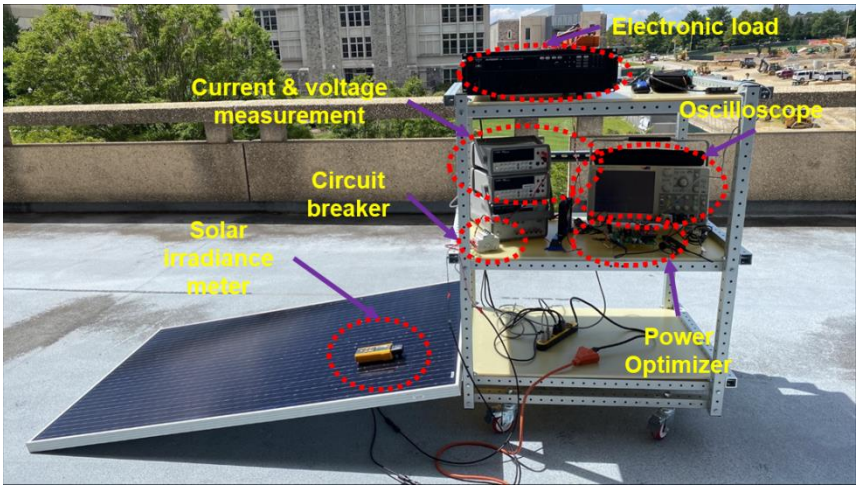

Figure 5-28 Hardware setup for outdoor AC impedance measurement of PV panel

The PV panel was tested outdoor on the third-floor balcony of Whittemore hall under Sun's illumination, as shown in Figure 5-28. The PV panel was rated for 300 W under 1000 W/m^2

illumination and 50 ˚C temperature. The PV panel sources DC power to the power optimizer; as discussed above, the power optimizer was used as a boost converter to sink the power from the PV panel and source it to electronic load BK precision 8610. The voltage and current were measured using an Agilent 34405A multimeter, the voltage waveforms were measured using a Tektronix TDP1500 differential probe, and the current waveform measured using Tektronix TCP0020 current probe was seen on a mixed signal oscilloscope Tektronix MSO5104. The Sun's irradiance and PV panel surface temperature was measured using Fluke IRR1-SOL solar irradiance meter. Eaton DC circuit breaker was used to obstruct current from the PV panel to the power optimizer under the shutdown condition.

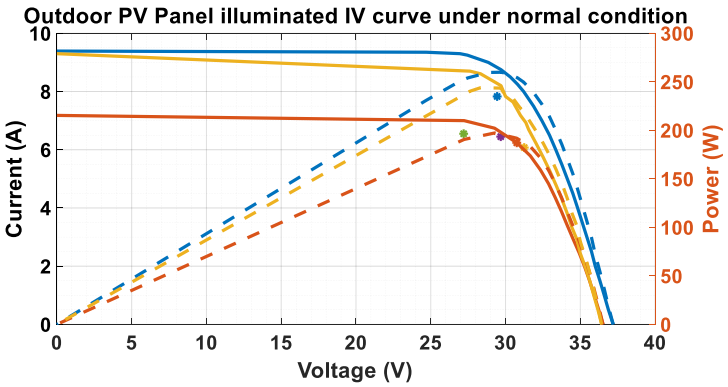

Figure 5-29 I-V and P-V characteristics under varying illumination on PV panel using hardware setup as shown in Figure 5-28

The PV panel I-V and P-V characteristics under varying sun illumination were measured and shown in Figure 5-29. The blue curve shows the I-V and P-V characteristics of the PV panel under 900 W/m^2 irradiances; with a decrease in illumination, the PV panel current drops, as discussed above, and can be noticed in the figure mentioned above.

5.5.2 PV Panel Online Impedance Measurement under Fault Condition

5.5.2.1 Under Short Circuit Fault:

The outdoor PV panel impedance was measured under 1 PV string short circuit fault using the online impedance measurement technique. The experiment was conducted outdoor, and the illumination on the PV panel measured for all conditions was 920 W/m^2. A circuit breaker was used to short-circuit one PV string in the junction box of a PV panel. The I-V and P-V characteristics of the normal condition (without short-circuiting PV string) were compared with the short circuit, as shown in Figure 5-30.Three operating points from each condition are injected with the small signal current to measure the impedance.

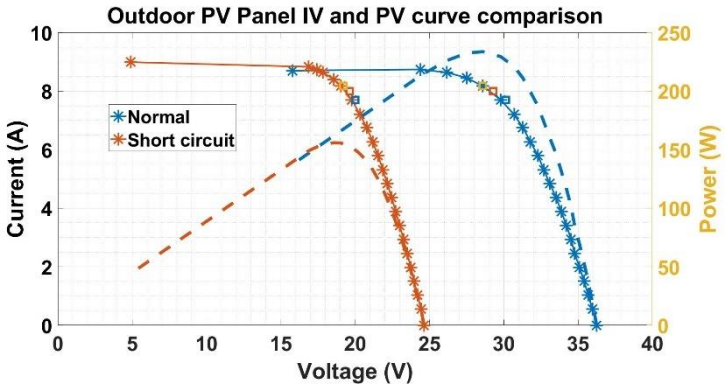

Figure 5-30 I-V curves of the PV panel under normal and short circuit conditions when the illumination is 920 W/m2

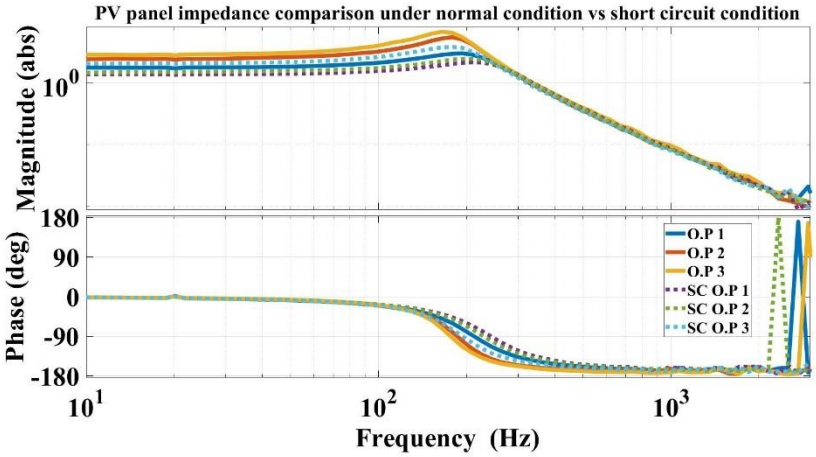

Figure 5-31 Measured small-signal impedance of the PV panel with short circuit condition using the outdoor test setup shown in Figure 5-28

The PV panel impedance was compared for the normal and short circuit conditions, as shown in Figure 5-31. Under short circuit conditions, the PV panel voltage decreases; as 20 PV cells are short-circuited, the 1/3rd voltage decreases can be seen in the I-V plot and Table 5-5. The fault indicators seen in modeling, offline and indoor online impedance measurement are similar in

the outdoor online impedance measurement test for PV panel short circuit fault condition. The fault indicators are a decrease in voltage, similar current, decreases in impedance magnitude under low frequency, and increases in phase under mid frequency.

Table 5-5 Summary of differences between impedances of normal and short circuit conditions

Operating Point	Condition	Voltage (V)	Current (A)	Impedance magnitude – 10 Hz (abs)	Phase -200 Hz(degree)
1.	Normal	30.15	7.7	1.76	-79.2
1.	Short circuit	20	7.7	**1.37**	**-59.9**
2.	Normal	29.3	8	2.4	-109
2.	Short circuit	19.65	8	**1.46**	**-66.2**
3.	Normal	28.6	8.17	2.86	-121
3.	Short circuit	19.2	8.17	**2.03**	**-96.3**

5.5.2.2 Under Hot Spot Fault:

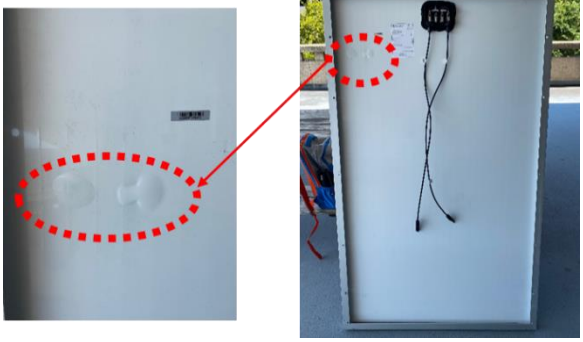

Figure 5-32 PV panel under hot spot fault with swell on the back plate of the PV panel

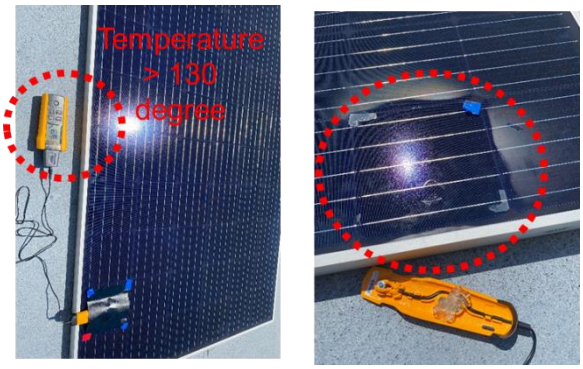

Figure 5-33 The rise in temperature on the shaded PV cell of the PV panel under a hot spot fault

The experiment was conducted outdoors, and the PV panel illumination measured for hot spot conditions was 650 W/m2. The outdoor PV panel impedance was measured under 1 PV cell shaded hot spot fault using an online impedance measurement technique. The experiment was

conducted for 15 minutes under hot spot conditions where 1 PV cell was shaded and sinking power rather than sourcing it; due to sinking power, the temperature of the shaded PV cell increased. The high temperature at the hot spot location caused a swell on the back plate of the PV panel, as seen in Figure 5-32. The temperature recorded by the Fluke irradiance meter was more than 130˚C, as seen in Figure 5-33, as the maximum temperature the irradiance meter can record was up to 100˚C.

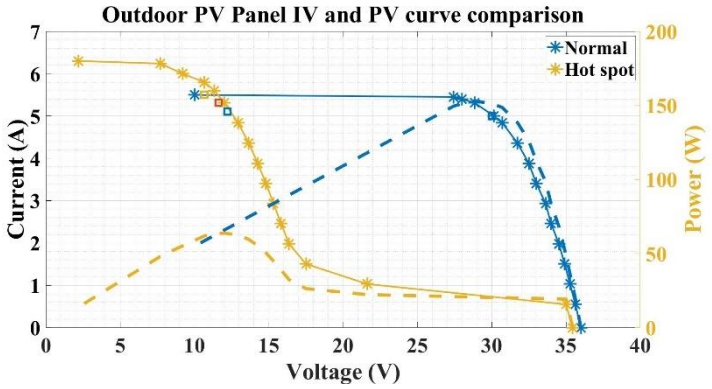

Figure 5-34 I-V curves of the PV panel under normal and hot spot conditions when the illumination is 650 W/m2

Table 5-6 Summary of differences between impedances of normal and hot spot conditions

Operating Point	Condition	Voltage (V)	Current (A)	Impedance magnitude – 10 Hz (abs)	Phase -200 Hz(degree)
1.	Normal	30	5	**3.81**	**-152**
1.	Hot spot	12.21	5.11	2.08	-97.4
2.	Hot spot	11.62	5.31	2.96	-134
3.	Hot spot	10.65	5.5	**5.29**	**-164**

The I-V and P-V characteristics of the normal condition (without shading the PV cell) are compared with the hot spot fault, as shown in Figure 5-34. Due to a decrease in illumination for the normal condition, the PV panel current is decreased compared to the hot spot condition. Three

O.Ps. from hot spot fault condition and one O.P. from normal are injected with a small signal current to measure the impedance. The PV panel impedance is compared for the normal and hot spot fault conditions, as shown in Figure 5-35. Under a hot spot fault condition, the PV panel voltage decreases, as 1 PV cell shaded was reverse biased, and due to the bypass diode of the same PV string open circuit, the reverse voltage will reduce the overall voltage of the PV panel, which can be a witness in the I-V plot as well as the table below. The O.P. of the hot spot fault near the MPP is compared with the normal condition. Due to different illumination, the measured impedance gives a different conclusion compared to the indoor online and offline measurement results. But as the illumination is low for the normal condition, the impedance magnitude measured is high. Referring to the modeling of the PV cell, with increased illumination, the PV panel impedance magnitude decreases; thus, the normal condition PV panel impedance would have been lower than the impedance magnitude measured. Table 5-6 compares the low-frequency impedance magnitude and mid-frequency impedance phase of O.Ps. Under normal and hot spot fault condition. The results show that implementing impedance-based indicators may cause confusion and wrong conclusion if the influence of the illumination was not considered. A possible solution is to record the impedance measurement and combine it with the time factor to have a better impedance comparison and fault detection.

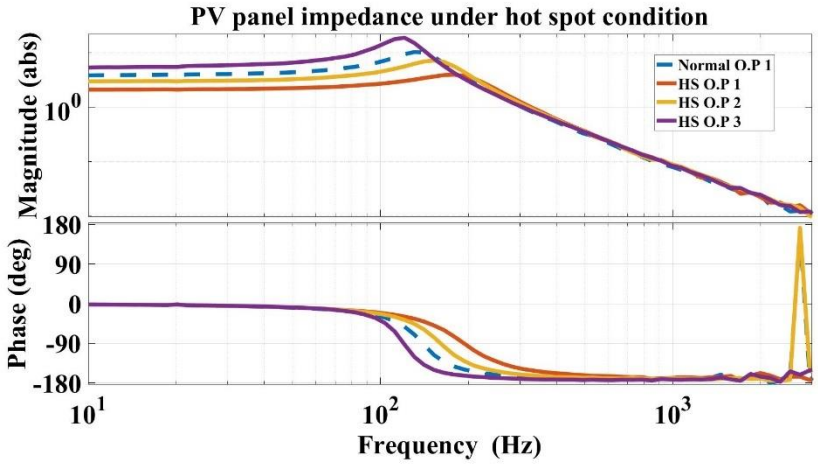

Figure 5-35 Measured small-signal impedance of the PV panel with hot spot condition using the outdoor test setup

5.6 Error Compensation Analysis

The online impedance measurement technique, as discussed above, measures the input impedance of the DC/ DC converter using a small signal injection. The small signal perturbation in input voltage and input current was computed to measure input impedance. The input impedance consists of the input capacitance of the DC/ DC converter, voltage and current sensor low pass filter, parasitic of DC/ DC converter and interface board PCB, dynamics of ADC in MCU, voltage and current sensor signal averaging, PV panel impedance and some unknown errors. A calibration test was performed, as shown in Figure 5-36, to measure the error in the computed impedance of the online impedance measurement technique.

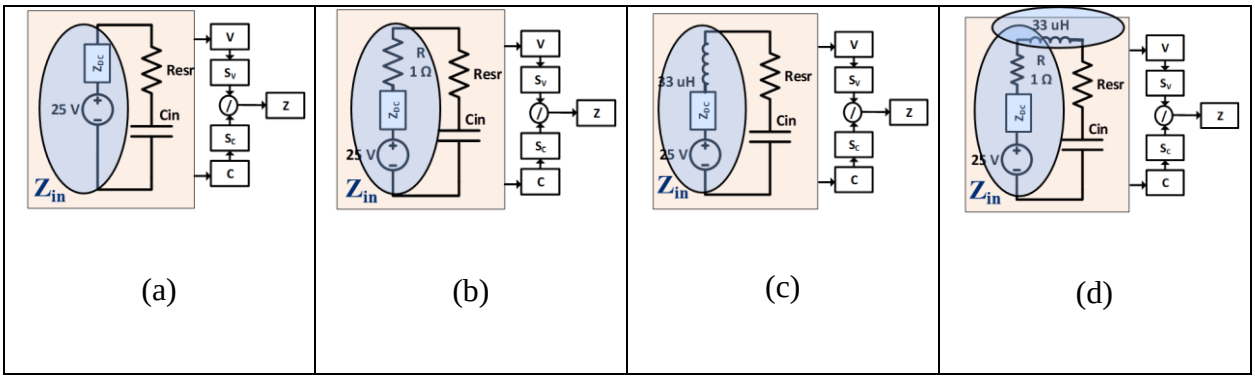

Figure 5-36 Input impedance measurement using online impedance measurement technique (a) power supply (b) power supply with 1 Ω resistance in series (c) power supply with 33 µH inductors in series (d) power supply with 1 Ω resistor and 33 µH inductor in series

Initially, the power supply was connected to the input of the DC/ DC converter and electronic load at the output. The converter was operated in boost mode with an inner current close loop and control signal generated in MCU with the operating point of 25 V input voltage, 0.7 A input current, and 40 V output voltage. SFRA injected small signal perturbation into the input of the DC/ DC converter; later, a 1 Ω was connected in series to the power supply, as shown in Figure 5-36 (b). Further, the 1 Ω resistor is replaced with 33 µH as shown in Figure 5-36 (c), and lastly, 1 Ω is added in series with a 33µH inductor. All four tests are performed, and the input impedance is measured and shown in Figure 5-37.

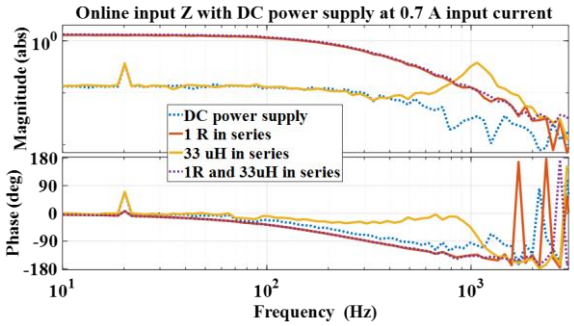

Figure 5-37 Input impedance plot for the test shown in Figure 5-36

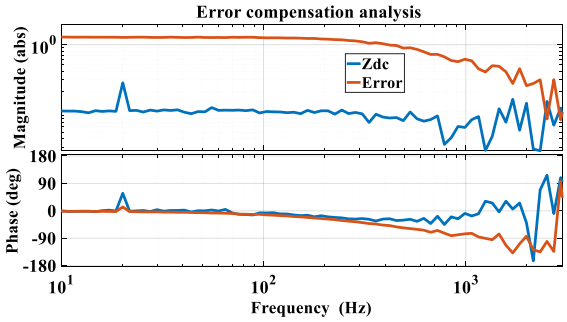

Figure 5-38 Estimating power supply impedance and error impedance for error compensation analysis

Equation (5-2) is considered for the measured input impedance; the equation shows the effects of voltage and current sensor low pass filter, input capacitance impedance of DC/ DC converter, and input impedance of converter apart excluding capacitor and some system error.

$$considering\ Z = \left(\frac{S_v}{S_c}\right) * (Z_{in} \,||\, C_{in}) * system_{error} \qquad (5\text{-}2)$$

The total error considered is shown in equation (5-3)

$$error\ \in\ = \left(\frac{S_v}{S_c}\right) * system_{error} \qquad (5\text{-}3)$$

Utilizing equation (5-3), the input impedance can be re-written as equation (5-4)

$$Z = (Z_{in} \,||\, C_{in}) * \in \qquad (5\text{-}4)$$

For the test, as shown in Figure 5-36 (a), the input impedance will be the effect of input capacitance, power supply impedance, and error, as shown in equation (5-5)

$$Z = (Z_{dc} \,||\, C_{in}) * \in \quad (5\text{-}5)$$

For the test, as shown in Figure 5-36 (b), the input impedance will be the effect of input capacitance, power supply impedance, 1 Ω series resistor, and error, as shown in equation (5-6)

$$Z_R = ((Z_{dc} + 1) \,||\, C_{in}) * \in \quad (5\text{-}6)$$

Computing power supply impedance from equations (5-5) and (5-6), we get a quadratic equation for power supply impedance as shown in equations (5-7)

$$Z_{dc}^2 + Z_{dc}(1 + C_{in}) + \frac{KC_{in}}{K-1} = 0 \quad (5\text{-}7)$$

Considering power supply impedance is positive, the impedance computed is shown in equation (5-8)

$$Z_{dc} = \frac{\sqrt{(1 + C_{in})^2 - \frac{4KC_{in}}{K-1}} - (1 + C_{in})}{2}, K = \frac{Z}{Z_R} \quad (5\text{-}8)$$

Utilizing equation (5-8), the error can be measured as shown in equation (5-9)

$$\in \; = \; \frac{Z_R}{(Z_{dc} || \, C_{in})} \quad (5\text{-}9)$$

The plot of power supply impedance and error is shown in Figure 5-38.

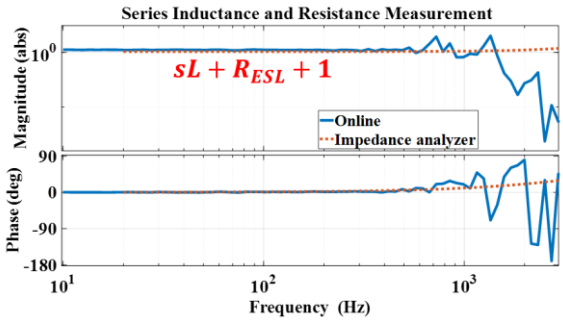

Figure 5-39 Measuring 1 Ω and 33 µH in series impedance using online impedance measurement technique and comparing with impedance measured using an impedance analyzer

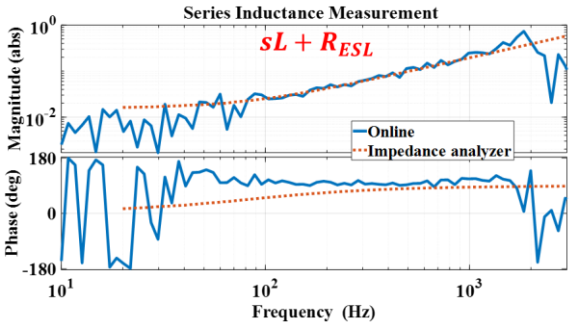

Figure 5-40 Measuring 33 µH impedance using online impedance measurement technique and comparing with impedance measured using an impedance analyzer

Using power supply impedance from equation (5-8) and error calibrated from equation (5-9), 33 µH inductance was measured from Figure 5-36 (c) and compared with impedance measured using an impedance analyzer and shown in Figure 5-40. The impedance magnitude is small under low frequency and difficult to measure, as can be seen in the impedance plot. Under the mid-frequency region, the impedance magnitude of measured inductance via online impedance with error compensation matches well with impedance measured using an impedance analyzer. Similarly, a 1 Ω resistor with 33 µH inductance in series, as shown in Figure 5-36 (d), was calibrated to exclude the effects of power supply impedance from equations (5-8) and error from equation (5-9). Figure 5-39 shows the compensated result of online impedance compared with impedance measured using an impedance analyzer. The impedance magnitude is small under low frequency and matches well with impedance measured using an impedance analyzer and can be

seen in the impedance plot. Frequency beyond 700 Hz, the impedance magnitude and phase don't match well with impedance measured using an impedance analyzer.

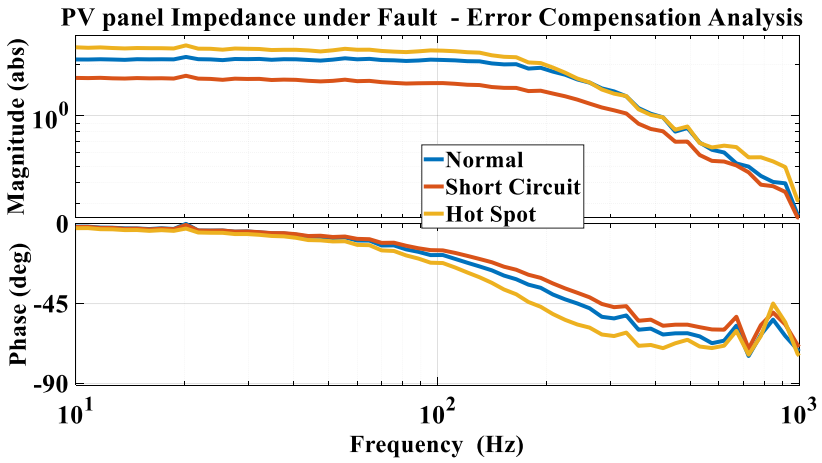

Figure 5-41 PV panel impedance measured using online impedance technique with error compensation comparison between normal Vs. fault condition

Figure 5-41 shows the PV panel impedance measured online under normal conditions compared with hot spot and short circuit conditions from section 5.4.2.1 and compensation with error as computed from equation (5-9). Comparing Figure 5-22 and Figure 5-41, the complex pole nature observed before error compensation cannot be noticed after the calibration test in the online impedance test. Also, the impedance phase notice prior to compensation decreased to -180 ˚ has now increased to -90 ˚ under the mid-frequency region.

5.7 Conclusion

Small signal injection generated using the single-tone technique was compared with the multitone technique; further, for the project, the single-tone was implemented using the SFRA technique. Boost converter inductor current was regulated using a control signal from MCU; DAC

in MCU generates an analog signal which was given to the boost converter as a control signal. For small signal injection into the inductor current, the analog signal was further added with a small signal generated by SFRA. Small signal perturbation in inductor current using SFRA was compared with small signal injection in input voltage with closed loop input voltage. Due to the additional voltage control loop, the bandwidth for small signal injection decreases; thus, the current injection was further utilized for the online impedance measurement technique. The online impedance measurement technique utilizes a small signal generated by SFRA to inject perturbation into the inductor current, and with a small signal component in voltage and current, the input impedance of the converter was measured. Updated P.O. was connected to the PV panel, and small signals for frequency 10 Hz to 22 kHz and amplitude 10 % of input PV panel current were injected into the current using SFRA.

The PV panel impedance was computed using input impedance measured through an online impedance measurement technique and input capacitance measured using an impedance analyzer. The temperature effect of the solar simulator was studied, and a rise in temperature under hot spot fault was noticed. PV panel impedance tested indoors under normal conditions was measured and compared with the change in operating point near the MPP. With O.P. changing from the left of MPP to the right of MPP, the impedance magnitude decreases, and also phase increases. The PV panel impedance was tested indoors under a hot spot, and the short circuit fault was measured and compared to the normal condition. The AC impedance under hot spot fault shows higher impedance magnitude and lower impedance phase compared to the normal condition; similar effects were noticed in the offline impedance measurement technique. Under short circuit conditions, the impedance magnitude is lower, and the phase is higher than in normal

conditions; similar effects are noticed in results based on the Simulink model. PV panel impedance under junction box fault measured and compared with the normal condition; under low frequency, the impedance magnitude is higher due to the addition of external series resistance. Capacitance fault was detected using an online impedance measurement technique. The relative standard deviation of online impedance measurement was tested, and less than 5% error was reported in faults like hot spot faults, short circuit faults, and junction box faults. PV panel impedance was measured using an online impedance technique under outdoor sunlight. Short circuit fault detection was tested using an online impedance measurement technique. Hot spot fault detection was tested using an online impedance measurement technique. The results show similarity with offline and modeling-based results. Error compensation analysis was studied for online impedance measurement, and PV panel impedance was calibration to remove the effects of voltage and current sensor low pass filter, parasitic of DC/ DC converter and interface board PCB, dynamics of ADC in MCU, voltage and current sensor signal averaging, and some unknown errors.

Chapter 6 Summary and Future Work

The boost converter with a PV panel model can detect hot spot faults, line-to-line faults, open circuit faults, junction box faults, and EOF of a capacitor using effective change in the operating points and with change in AC impedance magnitude and phase under at the MPP. The PV panel's illumination during the day changes due to a change in the sun's irradiance falling on the PV panel. The difference in illumination also changes the MPP, and with the shift in O.P., the AC impedance also changes. Table 2-5 shows the effects of change in illumination on PV panels with a decrease in illumination. To identify a PV panel fault, the fault detection nature should be distinctive for all the faults and different from the change in illumination under normal conditions. The fault indicators, as mentioned above, can be helpful to identify faults using AC impedance small signal PV cell model with O.P. at MPP of PV panel.

Under the continuous operation of the PV panel for a long time, it might go into multiple fault conditions where it can witness one or more than one faults. Figure 3-37 compares I-V and P-V characteristics of multiple fault scenarios with illuminated PV panels. The fault scenarios considered are hot spot fault, where one PV cell was shaded, the bypass diode was open-circuited; junction box fault, where a series resistance was added to the PV panel; and short circuit fault, where 1 PV string was short-circuited. The PV rack setup was used to measure the impedance of the PV panel under single and multiple fault conditions. Figure 3-38 compares impedance plots for multiple fault conditions. Comparing plot 2 with plot 1, the effect of short circuit fault is dominant as the operating point is not entirely MPP; thus, impedance magnitude is lower than normal conditions. Also, the phase is increased due to a short circuit fault. Comparing plot 3 with

plot 1, the hot spot fault indicators dominate under low-frequency and mid-frequency regions; under the mid-frequency region, the phase is decreased because of parallel capacitance. Also, due to additional series resistance, the impedance magnitude is higher than the normal condition at the resonating point. Thus, individual effects of hot spots and junction boxes can be noticed. Plot 4 is when the short circuit and junction box fault are noticed in the PV panel, the impedance plot resembles the short circuit fault, and at the mid-frequency region, because of the junction box fault, the magnitude of the impedance is higher than the plot 1. Under all three-fault conditions, the impedance plot is like hot spot and short circuit fault conditions, adding on the impedance magnitude at the resonating point due to junction box fault.

TI-based DC/ DC boost converter LM5170EVM was configured using header pins, and inductor current was regulated to control the converter in boost operation. TI launchpad F28379-D was interfaced with a boost converter to operate the evaluation board under normal operation and generate a control signal for regulating the inductor current. DC/ DC converter was tested under light load using evaluation boards' analog outer voltage loop prior to update. Under light load operation, diode emulation mode was noticed, and DC/ DC converter CCM was further studied. DC/ DC boost converter inductance was updated from 4.7 µH to 33 µH, and MOSFET switching frequency was increased from 100 kHz to 160 kHz to operate the boost converter from 24 W to 300 W. With updating inductance and switching frequency, MOSFET losses, and inductance losses were studied for boost converter application. The current sensor was updated for better resolution under the low current application. The average current control mode was simulated, and the inner current compensation circuit was updated for inner current close loop operation. The converter was tested under 24 W and 75 W with inner current close loop operation.

The DC/ DC converter evaluation board was further used as a power optimizer to measure PV panel impedance.

Small signal injection generated using the single-tone technique was compared with the multitone technique; further, for the project, the single-tone was implemented using the SFRA technique. Boost converter inductor current was regulated using a control signal from MCU; DAC in MCU generates an analog signal which was given to the boost converter as a control signal. The online impedance measurement technique utilizes a small signal generated by SFRA to inject perturbation into the inductor current, and with a small signal component in voltage and current, the input impedance of the converter was measured. Updated P.O. was connected to the PV panel, and small signals for frequency 10 Hz to 22 kHz and amplitude 10 % of input PV panel current were injected into the current using SFRA.

The PV panel impedance was computed using input impedance measured through an online impedance measurement technique and input capacitance measured using an impedance analyzer. With O.P. changing from the left of MPP to the right of MPP, the impedance magnitude decreases, and also phase increases. The PV panel impedance was tested indoors under a hot spot, and the short circuit fault was measured and compared to the normal condition. The AC impedance under hot spot fault shows higher impedance magnitude and lower impedance phase compared to the normal condition; similar effects were noticed in the offline impedance measurement technique. Under short circuit conditions, the impedance magnitude is lower, and the phase is higher than in normal conditions; similar effects are noticed in results based on the Simulink model. PV panel impedance under junction box fault measured and compared with the normal condition; under low frequency, the impedance magnitude is higher due to the addition of external

series resistance. Capacitance fault was detected using an online impedance measurement technique. The relative standard deviation of online impedance measurement was tested, and less than 5% error was reported in faults like hot spot faults, short circuit faults, and junction box faults. PV panel impedance was measured using an online impedance technique under outdoor sunlight. Short circuit fault detection was tested using an online impedance measurement technique. Hot spot fault detection was tested using an online impedance measurement technique. The results show similarity with offline and modeling-based results. Error compensation analysis was studied for online impedance measurement, and PV panel impedance was calibration to remove the effects of voltage and current sensor low pass filter, parasitic of DC/ DC converter and interface board PCB, dynamics of ADC in MCU, voltage and current sensor signal averaging, and some unknown errors.

Power converter bandwidth is low, either less than 3 kHz; thus, the small signal response is limited to 2 kHz. A possible solution would be to increase the inner current control loop bandwidth to 1/5th of the switching frequency. The SFRA-based small signal injection takes 1 – 1.5 minutes for injection and computation; thus, the operation point can get shifted due to changes in irradiance, multi-tone small signal can be used for a fast response in the future. Signal conditioning is required for voltage, and current sensed after ADC due to the low pass filter present at ADC input, high bandwidth filter can be used for noise attenuation. A small signal amplitude greater than 20% can lead to a system undergoing instability, and a small signal amplitude lesser than 10% will lead to a response with noise at a high frequency; software-based signal conditioning can be used for a better response for future work.

References

1. Wesley Cole, Daniel Greer, Jonathan Ho, Robert Margolis, “Considerations for maintaining resource adequacy of electricity systems with high penetrations of PV and storage”,Applied Energy,Volume 279,2020,115795,ISSN 0306-2619.
2. Curtis, Taylor L., Heather Buchanan, Garvin Heath, Ligia Smith, and Stephanie Shaw. 2021. Solar Photovoltaic Module Recycling: A Survey of U.S. Policies and Initiatives. Golden, CO: National Renewable Energy Laboratory. NREL/TP-6A20-74124
3. Feldman, David, Vignesh Ramasamy, Ran Fu, Ashwin Ramdas, Jal Desai, and Robert Margolis. 2021. U.S. Solar Photovoltaic System Cost Benchmark: Q1 2020. Golden, CO: National Renewable Energy Laboratory. NREL/TP-6A20-77324.
4. K. A. Kim, C. Xu, L. Jin, and P. T. Krein, “A Dynamic Photovoltaic Model Incorporating Capacitive and Reverse-Bias Characteristics,” *IEEE J. Photovoltaics*, vol. 3, no. 4, pp. 1334–1341, Oct. 2013, doi: 10.1109/JPHOTOV.2013.2276483.
5. N. Akpolat, Y. Yang, F. Blaabjerg, E. Dursun, and A. E. Kuzucuoglu, “Modeling Photovoltaic String in PLECS Under Partial Shading,” in *2019 International Conference on Power Generation Systems and Renewable Energy Technologies (PGSRET)*, Istanbul, Turkey, Aug. 2019, pp. 1–6. doi: 10.1109/PGSRET.2019.8882698.
6. C. Chamberlin, M. A. Rocheleau, M. W. Marshall, A. M. Reis, N. T. Coleman, and P. A. Lehman, “Comparison of PV module performance before and after 11 and 20 years of field exposure,” in Proc. IEEE Photovoltaic Specialists Conf., June 2011, pp. 101–105

7. A. Mellit, G. M. Tina, and S. A. Kalogirou, “Fault detection and diagnosis methods for photovoltaic systems: A review,” *Renewable and Sustainable Energy Reviews*, vol. 91, pp. 1–17, Aug. 2018, doi: 10.1016/j.rser.2018.03.062.
8. K. A. Kim, G.-S. Seo, B.-H. Cho, and P. T. Krein, “Photovoltaic Hot-Spot Detection for Solar Panel Substrings Using AC Parameter Characterization,” *IEEE Trans. Power Electron.*, vol. 31, no. 2, pp. 1121–1130, Feb. 2016, doi: 10.1109/TPEL.2015.2417548.
9. K.-M. Jakobi, W. Nasse, D. M. Parterna, D. F. Ansorge, C. Baar, and K. Ring, “FAULTS OF CONTACTS IN PV MODULE JUNCTION BOXES DUE TO FRETTING CORROSION,” p. 6.
10. Z. Zhao, P. Davari, W. Lu, H. Wang, and F. Blaabjerg, “An Overview of Condition Monitoring Techniques for Capacitors in DC-Link Applications,” IEEE Trans. Power Electron., vol. 36, no. 4, pp. 3692–3716, Apr. 2021, doi: 10.1109/TPEL.2020.3023469
11. O. I. Olayiwola and P. S. Barendse, “Photovoltaic Cell/Module Equivalent Electric Circuit Modeling Using Impedance Spectroscopy,” *IEEE Trans. on Ind. Applicat.*, vol. 56, no. 2, pp. 1690–1701, Mar. 2020, doi: 10.1109/TIA.2019.2958906.
12. S. Osawa, T. Nakano, S. Matsumoto, N. Katayama, Y. Saka, and H. Sato, “Fault diagnosis of photovoltaic modules using AC impedance spectroscopy,” in *2016 IEEE International Conference on Renewable Energy Research and Applications (ICRERA)*, Birmingham, United Kingdom, Nov. 2016, pp. 210–215. doi: 10.1109/ICRERA.2016.7884539.
13. T. Yokoi, K. Takechi, and H. Kakigano, “Impedance Measurement Method for Solar Cell Evaluation using a Power Converter,” in *2019 IEEE Third International Conference on*

DC Microgrids (ICDCM), Matsue, Japan, May 2019, pp. 1–6. doi: 10.1109/ICDCM45535.2019.9232790.

14. S.-Y. Chiu, K. A. Kim, and Y.-C. Liu, "Analysis of Nanosatellite Impedance Interaction and Stability Based on System Operation Mode," in *2021 IEEE International Future Energy Electronics Conference (IFEEC)*, Taipei, Taiwan, Nov. 2021, pp. 1–6. doi: 10.1109/IFEEC53238.2021.9662020.
15. B. Miao, R. Zane, and D. Maksimovic, "System Identification of Power Converters With Digital Control Through Cross-Correlation Methods," *IEEE Trans. Power Electron.*, vol. 20, no. 5, pp. 1093–1099, Sep. 2005, doi: 10.1109/TPEL.2005.854035.
16. A. Riccobono *et al.*, "Stability of Shipboard DC Power Distribution: Online Impedance-Based Systems Methods," *IEEE Electrific. Mag.*, vol. 5, no. 3, pp. 55–67, Sep. 2017, doi: 10.1109/MELE.2017.2718858.
17. A. Barkley and E. Santi, "Online Monitoring of Network Impedances Using Digital Network Analyzer Techniques," in *2009 Twenty-Fourth Annual IEEE Applied Power Electronics Conference and Exposition*, Washington, DC, USA, Feb. 2009, pp. 440–446. doi: 10.1109/APEC.2009.4802695.
18. H. Walker *et al.*, "Model of Operation-and-Maintenance Costs for Photovoltaic Systems," NREL/TP-5C00-74840, 1659995, MainId:6662, Jun. 2020. doi: 10.2172/1659995.
19. J. Panchal, B. Wen, and R. Burgos, "Power Electronics Based Self-Monitoring and Diagnosing for Photovoltaics Systems," in *2021 IEEE 22nd Workshop on Control and Modelling of Power Electronics (COMPEL)*, Cartagena, Colombia, Nov. 2021, pp. 1–8. doi: 10.1109/COMPEL52922.2021.9646060.